Dissertation

submitted to the
Combined Faculties for the Natural Sciences and for Mathematics
of the Ruperto-Carola University of Heidelberg, Germany
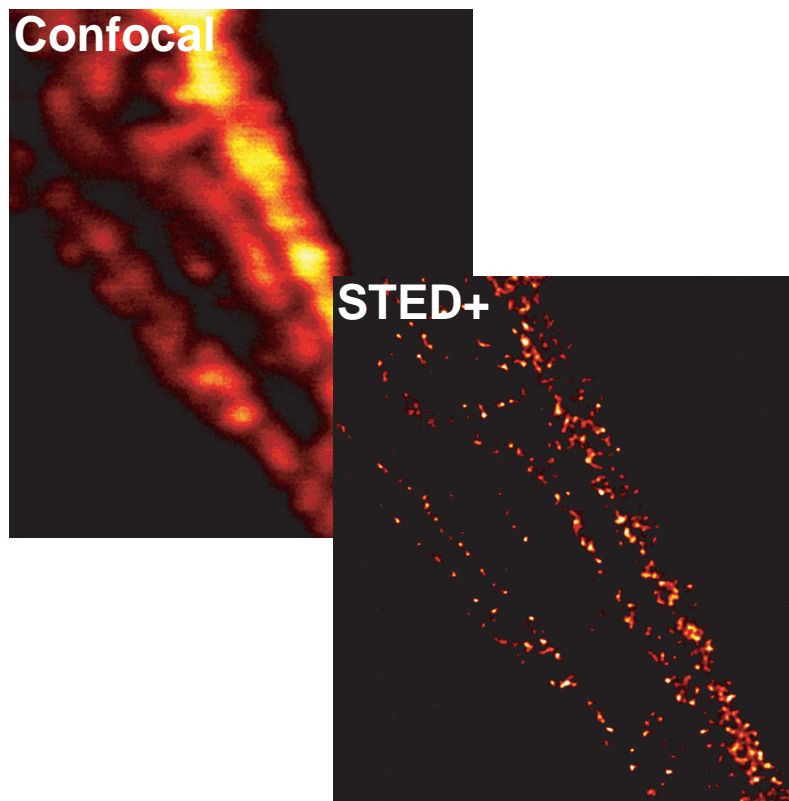for the degree of
Doctor of Natural Sciences

presented by
Diplom-Physiker Gerald Donnert
born in Nürnberg

Oral examination: April 18th, 2007

Dual-colour STED-microscopy

on the Nanoscale

Referees: Prof. Dr. Stefan W. Hell
Prof. Dr. Josef Bille

Zusammenfassung:

Gesättigte Entvölkerung durch stimulierte Emission (engl.: STED) ist das erste Konzept, welches die Abbesche Beugungsgrenze in der optischen Fernfeld-Mikroskopie überwindet und erfolgreich in der Zellbiologie angewandt wurde. Jedoch war die theoretisch unbegrenzte Auflösung durch Ausbleichen der Farbstoffmoleküle limitiert. In dieser Arbeit wird in einer umfassenden Studie zur ein- und zwei- Photonen Anregung die Dunkelzustands-Relaxation (engl.: D-Rex) als ein effektives Mittel der Bleichreduzierung nachgewiesen, welche gleichzeitig eine enorme Fluoreszenzsignalzunahme pro Anregungspuls hervorruft. Dies bereitet den Weg für eine erfolgreiche Kombination dieser Anregungsstrategie mit der STED-Mikroskopie und ermöglicht die Anwendung einer 10-fach höheren STED-Energie aufgrund reduzierten Farbstoffbleichens. Damit wird die laterale Auflösung in der STED-Mikroskopie auf $\approx$ 20 nm erhöht, was einer 12-fachen Auflösungserhöhung über der Abbeschen Beugungsgrenze entspricht. Dieses makromolekulare Trennungsvermögen wird auf eine Vielzahl biologischer Fragestellungen angewendet, einschließlich der Untersuchung von Zellkontaktproteinen und fokalen Zellkontaktstellen sowie der hochaufgelösten Erforschung der Neurofilamenten menschlicher Neuronenzellen. Schließlich wird erstmals die Erweiterung auf ein Zwei-Farben STED-Mikroskop realisiert, das eine Nanoskalen präzise Kolokalisation individueller Proteinkluster ermöglicht und damit die Anwendungsmöglichkeiten der STED-Mikroskopie nachhaltig erweitert. Diese Methode kann bislang unentdeckte Nanostrukturen von Vesikelproteinen auf Endosomen darstellen sowie verschiedene Proteine in Säugetier-Mitochondien hochaufgelöst kolokalisieren.

Abstract:

Stimulated emission depletion (STED) microscopy was the first concept for breaking Abbe's diffraction barrier in optical far-field microscopy verified in biological applications. However, the theoretically infinite resolution was limited due to photobleaching of the fluorescent species. In this thesis, dark-state relaxation (D-Rex) has been traced in a comprehensive study on one- and two-photon excitation to crucially reduce photobleaching in general thus leading to a major signal increase per excitation pulse. This facilitated a successful combination of this illumination strategy with STED-microscopy making a 10-fold increase of STED-power feasible. The expansion of STED-microscopy to D-Rex conditions at 250 kHz leads to a yet unattained focal plane resolution $\approx$ 20 nm, equivalent to an approximate 12-fold multilateral increase of resolution below the diffraction limit. This macromolecular resolution was exemplified in a variety of biological samples, including proteins of cell-junction and focal adhesion, or a neurofilamental protein from the human brain. Finally, the extension to a Dual-colour STED-microscope was achieved to provide nanoscale precise colocalization ability of individual protein clusters in cell biology, thereby sustainably widening the application range of STED-microscopy. The method proved to resolve hitherto uncovered nanopatterns of vesicle proteins on endosomes, as well as localized different proteins in mammalian mitochondria.

Abbreviations

+	Iterative Deconvolution algorithm (Richardson-Lucy)
1D	One-dimensional
2D	Two-dimensional
3D	Three-dimensional
4Pi-microscopy	Microscopy using two opposing lenses in a coherent way
AFM	Atomic force microscope
ANT	Adenosin nucleotide transporter
APD	Avalanche photodetector
ATP	Adenosintriphosphat
CNGA2	Cyclic nucleotide-gated channel subunit A2
CW	Continuous wave
DM	Dichroic mirror
D-Rex	Dark-state relaxation
EM	Electron microscope
Exc	Excitation
FCS	Fluorescence correlation spectroscopy
FRAP	Fluorescence recovery after photobleaching
FREF	Förster resonance energy transfer
FWHM	Full width at half maximum
GFP	Green fluorescent protein
GSD	Ground state depletion
IR	Infrared
ISC	Intersysem crossing from singlet to triplet system
LD	Linear deconvolution
LSM	Laser scanning microscope
MOE	Main olfactory epithelium
NA	Numerical aperture of a lens (NA= $n \sin \alpha$)
OL	Objective lens
ONE-photon	One-photon excitation condition

OPA	Optical parametric amplifier
OPO	Optical parametric oscillator
OSN	Olfactory sensory neuron
PALM	Photoactivation light microscopy
(PAL-)SLM	(parallel-aligned nematic liquid crystal) spatial light modulator
PSF	Point spread function
RESOLFT	Reversible saturable optical (fluorescence) transitions
RL	Richardson-Lucy algorithm for deconvolution
RNA	Ribonucleic acid
s.d.	Standard deviation
SMF	Single-mode fibre
SMHCF	Single-mode hollow-core fibre
SNAP25	Synaptosome associated protein of 25kDa
SNOM	Scanning near-field optical microscopy
STD	Standard deviation
STORM	Stochastic optical reconstruction microscopy
STED	Stimulated emission depletion
TIRF	Total internal reflection fluorescence
TL	Tubus lens
Tom20	Protein of the TOM-complex in the mitochondria outermembrane
TPM	Two photon microscopy
T-Rex	Triplet-state relaxation
TRPM5	Protein M5 of the transient receptor potential channel
TWO-Photon	Two-photon excitation condition
VE-cadherin	Vascular endothelial cadherin complex protein
VIS	Visible

Contents

1 Introduction

,,Wär in der Natur überhaupt ein Zufall - auch nur einer -, so würdest du ihn in allgemeiner Regellosigkeit erblicken. Weil aber alles, was in ihr geschieht, mit blinder Notwendigkeit geschieht, so ist alles, was in ihr geschieht oder entsteht, Ausdruck eines ewigen Gesetzes und einer unverletzbaren Form."

FRIEDRICH WILHELM SCHELLING

1.1 Importance of modern light microscopy in cell biology

Science begins with careful observation. The more accurate and precise the observation, the sounder the hypothesis, the more discerning the experiment, the more telling and reliable the result. Techniques that allowed us to observe organelles and molecules made a revolution in science possible, resulting in the fields of cellular and molecular biology; these disciplines have laid the foundations for an important number of advances in many areas of biology, including the medical arena.

Since light has proven to be one of the most decisive factors for the evolution of life on this planet, clever pioneers started exploiting the phenomena of visible light for investigating the origin and mechanisms of life itself. One of the foundations of far-field light microscopy were laid in the 19th century, when Carl Zeiss and Ernst Abbe combined their engineering and theoretical outstanding abilities. In 1873 Ernst Abbe derived the wave theory of optical imaging ([1]), setting a milestone in the theory of microscopy since today. He was the first to recognize, that the resolution of a far-field microscope, likely to be the most essential characteristic of an optical tool, is limited by diffraction, a fundamental physical law. The diffraction barrier states that far-field optics cannot focus light to an infinitely small spot, rather its size is limited e.g. in lateral dimension to $\Delta x \approx 0.5\lambda/NA$, with λ denoting the wavelength of the focused light, and $NA=n\sin\alpha$ describing the light collecting ability of the focusing lens. The refractive index n and the maximum cone angle α of accepted light by the lens are technically limited. The intensity distribution of the

focused light in the specimen is called the point spread function (PSF), or expressing it in words: a point light source (e.g. a single fluorescent molecule) is imaged by a single lens not back to a single point, but is spread out due to diffraction. In terms of resolution, the size of the PSF is essential since its spatial extent determines the smallest dimension that can be resolved in the image ([2]). The lateral spot size is often referred to as Airy disk which is defined as the lateral distance between the primarily intensity minima. The diameter of the Airy disk is given, as previously described, by the Abbe formula,

$$\Delta x, \Delta y \approx 1.22 \frac{\lambda}{NA} \tag{1.1}$$

and respectively, for the axial dimension, the distance between the primarily minima leads to ([3]):

$$\Delta z \approx 4.00 \frac{n\lambda}{(NA)^2} \tag{1.2}$$

Till today the Abbe law is valid for describing the focusing process of light thus determining the resolution of a conventional far-field light microscope applying visible light which is about 200 nm in the lateral and 500 nm in the axial directions.

The wide range of available fluorescent markers adds to the importance of light microscopy in cell biology. Apart from fluorescence detection containing multidimensional information regarding light colour, lifetime, intensity or polarization, selective labeling strategies of proteins or lipids in cells enable the study of the tagged species in terms of localization or dynamic behavior. The immunolabeling technique being one of the first specific labeling approaches in the 1940s uses antibodies for recognizing specifically the protein of interest. Since the antibodies are decorated with fluorescent labels, their binding distribution in the cell is accessible by light microscopy.

Traditional imaging technologies, including light and electron microscopy (EM) opened a window on the inner working of cells and organisms. The latter technique addresses the problem of resolution limitation by choosing the operating wavelength of accelerated electrons being orders of magnitude smaller than the wavelength of visible light. With the de Broglie wavelength of electrons being below 1nm, this approach delivers a resolution ability down to the molecular level ([4]). However, highly energetic electrons are inherently destructive to biological material rendering live cell imaging impossible. Furthermore, EM-sample preparation involves sample cutting into thin slices, thereby interrupting 3D relationships and requires contrast enhancing materials such as gold nanoparticles. To conserve slow cellular processes evolving at least on the millisecond time scale, one can shock-freeze the sample at different timescales with afterwards imaging different stages of the interesting process.

It is the limitation of real 3D resolution capability that EM-microscopy is facing. This was overcome by confocal microscopy proposed 1955 by Minsky ([5]), after a century of stagnation in the field of optical microscopy have passed. The principle of confocal microscopy is to illuminate the specimen with laser light focused at one position in the specimen using only a single point of illumination. In combination with pinhole detection, this method ensures, that the light spot generated at the far-field is the smallest spot available due to diffraction and is exploited to the maximum extent.

The detected signal (e.g. fluorescence light from labeled cellular structures) is imaged by the same objective again onto a point detector, e.g. with a spatial filter smaller in size than the Airy disk of the imaged detection light. This leads to "out of focus light rejection", i.e. the illumination intensity immediately above and below the focal plane is reduced due to beam convergence and divergence. Light scattered from parts other than the specimen illumination point is rejected from the optical system to an extent never realized before, thus establishing light microscopy for the first time with a real 3D resolution.

The overall detection probability of a fluorescence photon is governed by two contributions: the excitation light distribution giving the probability of exciting a fluorescent species at the specimen and the probability of detecting a thereby generated fluorescence photon by the point detector, denoted the detection PSF h_{det}. Therefore the confocal PSF is given by

$$h_{conf}(\vec{r}) = h_{exc}(\vec{r})h_{det}(\vec{r}) \cong h_{exc}(\vec{r})^2 \tag{1.3}$$

Here the product of both PSF's reveals a quadratic suppression of out of focus light, thus ensuring axial resolution performance of $\cong \lambda$ determined by the confocal spot size (the identity in (1.3) is valid, if excitation and detection wavelengths are the same). For obvious reasons, a combination of the confocal pinhole with the laser scanning microscope (LSM) presents the standard device for biological imaging and spectroscopic applications, having demonstrated single molecule sensitivity. In the latter method, the image build-up is arranged by scanning the single focal spot through the specimen, in contrast to wide-field techniques, where the complete image is obtained at the same time by homogeneously illuminating the area of interest. For this reason, the confocal performance is taken as reference for the developments in this thesis, especially since the STED technique in the implementation presented here is based on the confocal setup.

Another development successfully improved the performance of confocal LSM with regard to tissue penetration ability. The widespread availability of ultrashort laser sources providing high electromagnetic fields ([6]) made two-photon excitation, which is a non-linear absorption process that needs to absorb two photons at the same time for exciting a fluorescent molecule ([7]), accessible for microscopy. The two-photon absorption is proportional to the square of the light intensity at the specimen thus limiting the excitation

spatially to the center of the focus. This fact makes the presence of a detection pinhole unnecessary, while still providing full 3D sectioning ability. In combination with the fact that infrared light photons with energy hν (ν denoting the light frequency), now providing the excitation energy of 2hν, are much less absorbed in biological material, two-photon microscopy (TPM) provides deeper penetration depths in highly scattering samples like brain slices or tissue ([8]). Still, in terms of resolution, the TPM cannot surpass the conventional one-photon excitation, since the doubled wavelength of excitation in TPM cancels out the effect of smaller effective focal volumes due to the quadratic excitation probability ([9]). Increased photobleaching in the center of the focus due to orders of magnitude higher peak powers as compared to single photon excitation limits however its applications and is also center of interest in chapter (2.2) of this thesis.

Addressing the minor axial resolution of a confocal microscope of around 500 nm, the concept of 4Pi-microscopy ([10],[11]) brought a major breakthrough in axial sectioning. Since the focusing angle of one objective is limited to values $\alpha \approx 70°$ (see equation 1.2), the idea to mimic focusing light from the full 4π angle lead to the realization of fusing two objectives opposing each other. Constructive interference in the focal point results in a pronounced intensity maximum that is about four times narrower than that compared to a single objective. Since the PSF also features axial side maxima, the images need to be deconvolved for uncovering the pure object. The applicability of 4Pi-microscopy to living cells with an axial resolution of ≈ 80 nm was already shown in ([12]).

Similarly motivated by the lack of resolution, optical near-field surface methods were established. Total internal reflection microscopy (TIRF) makes use of generating an evanescing light field when the sample is illuminated at high angles featuring total internal reflection ([13]). The axial resolution is governed by the penetration depth of around 100 nm and can only be exploited for structures within this proximity of the glass surface. Another method which does not rely on focused light and thus not being governed by the Abbe law is the scanning nearfield optical microscope (SNOM) ([14],[15]). The trick here is to use a nanoscaled tip with a light emitting aperture much smaller than λ. When avoiding the divergently propagating radiation out of the aperture by placing the sample right next to the tip in the near-field, the area of illumination is directly given by the dimension of the tip. Having shown illumination areas of 50-100 nm ([14]), this approach is however confined to image surfaces only. Moreover, an elaborate tight control of the aperture tip is necessary.

Important progress and development in the field of studying molecular processes on the nanoscale range was achieved by spectroscopic approaches, addressing questions of distances and interaction dimensions below the diffraction limit. For example the Förster Resonance Energy Transfer (FRET) makes use of the nonradiative energy transfer from a previously excited donor molecule to an acceptor molecule via dipole-dipole coupling

([16],[17]). The red shifted fluorescence intensity decodes the efficiency of the FRET-process. Since this process is sensitive to the distance of both molecules the energy transfer rate is an efficient nanometer ruler. In fact, the transfer efficiency varies with the 6th power of the donor-acceptor separation over the range of 1-10 nm. The technique is applicable to questions on chemical bonding, molecular conformation or colocalization problems. Obviously, the spatial distribution of the FRET-process in for example cellular environment can only be read out diffraction limited. Another powerful spectroscopic approach is fluorescence correlation spectroscopy (FCS). It allows one to investigate diffusion, molecular dynamics and chemical reactions, e.g. clustering behaviour of individual molecules, in solution and also in live cells ([18]).

However, all of these methods have brought application-driven improvements but none of them has questioned the basic limiting factor, namely the diffraction limitation itself. Ever since the invention of the light microscope and our first vistas of cells, technological and conceptual developments have gone hand in hand. The ultimate tool for any cell biologist would be the combination of life-cell compatibility, 3D accessibility and nanoscale resolution. In other words, a focusing far-field light microscope with nanoscale resolution, which was believed to be impossible only a couple of years ago. The following describes the very latest approaches to overcome the diffraction barrier which has the potential to open a new realm of microscopy.

1.2 Subdiffraction resolution techniques are breaking ground for a new realm in microscopy

The very first concept of breaking the diffraction barrier, namely STimulated Emission Depletion (STED), was proposed by Hell and Wichmann in 1994 ([19]). So far STED is the most sophisticated implementation of a more generalized concept, which is denoted reversible saturable optical fluorescence transition (RESOLFT) ([20]). Before discussing the basic STED implementation detailed in the next section, the RESOLFT concept behind it will be illustrated here, since any RESOLFT-type subdiffraction technique so far can be related to this idea.

Starting with two arbitrary states of a fluorophore, A and B, one of these states must be fluorescent (let us assume state A), the other one needs to be dark (at least in the detection window). One of these transitions, e.g. the reverse transition into the nonfluorescent state (A$\longrightarrow$B) must be optical saturable by increasing the light intensity of the fluorescence inhibiting light (deexcitation power I) (Fig.1.1 (a)). The molecules can be effectively pushed into the state B by arbitrarily increasing the deexcitation power. The deexcitation beam intensity I is organized in such a way that it features intensity zeros in space (Fig.1.1
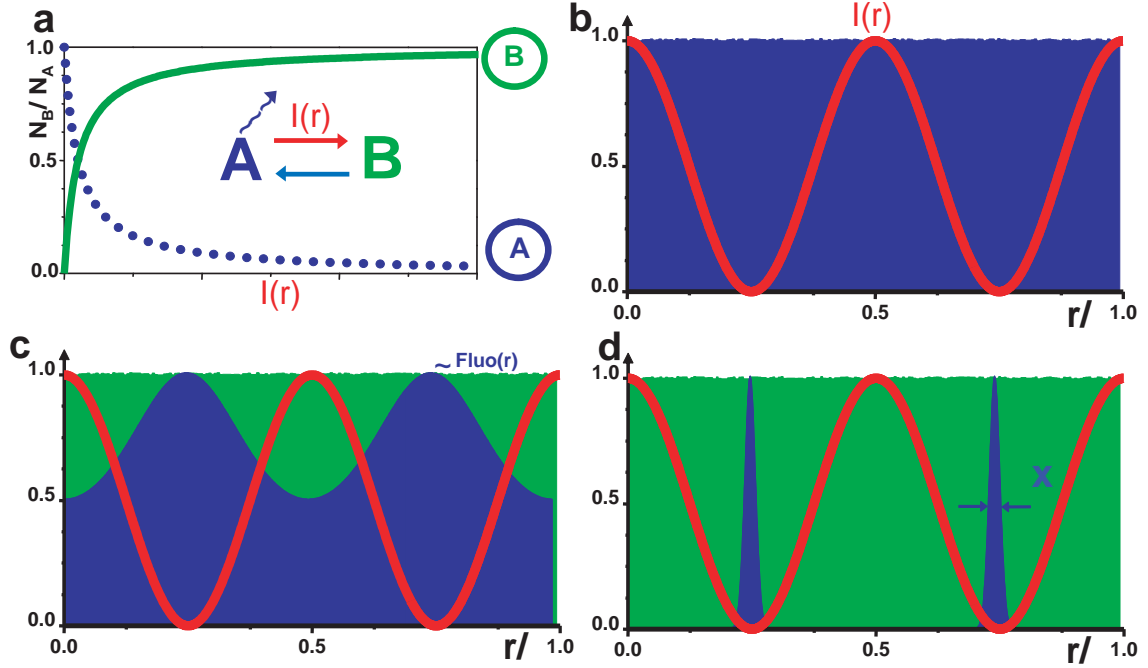
Figure 1.1: RESOLFT concept of breaking the diffraction barrier. (a) Saturation behaviour of the fluorescence inhibition driven by the deexcitation light intensity I(r) from the fluorescent state A to the dark state B. Both transitions are light induced. (b) Wide-field excitation of the molecules into state A (blue); note that the deexcitation light I(r) is featuring intensity zeros, e.g. by destructive interference. The remaining molecules in state B (blue) indicate the fluorescence intensity Fluo(r). (c) Applying the saturation power level of the deexcitation beam can only deplete molecules outside the intensity zeros. (d) Ramping up the deexcitation power to arbitrary values leads to subdiffraction areas of remaining excitation with $\Delta x \approx \frac{\lambda}{\sqrt{\frac{I}{I_{sat}}}}$. Saturation factors I/I_{sat} for simulation in panel (b,c,d): 0, 1, 16^2.

(b)), which is always possible even in wide-field illumination through the interference phenomena. Only those molecules in the intensity zero can resist being deexcited (Fig.1.1 (c)). Since the transition is saturable, the molecules being infinitely delocalized outside the intensity zero can still be forced into state B by arbitrarily increasing the deexcitation power I, the resolution thus being theoretically unlimited (Fig.1.1 (d)). In STED state A represents the excited fluorescent level and state B is the ground state of the fluorophore. A second implementation beside the STED concept is the utilization of photoswitchable proteins for showing subdiffraction resolution ([21]). Here a conformational change is responsible for the switching between a fluorescent and a nonfluorescent state of the fluorescent protein asFP545. It should be mentioned that the switching takes place on

time scales of miiliseconds or seconds. This spontaneous relaxation process into state B must be overpowered by the light induced deexcitation process to reach saturation levels. Therefore the saturation peak powers for the induced switching process feature moderate values of W/cm^2. Compared to the values of the STED-implementation, where the deexcitation process is stimulated emission, as described detailed in the next section, the spontaneous relaxation process of spontaneous fluorescence emission ($\approx$ ns) makes saturation powers that are orders of magnitude larger necessary (see chapter 3.1).

The photoswitchable proteins were the missing ingredient in another smart idea to break effectively the diffraction barrier, as proposed and verified in ([22],[23]). In photoactivation light microscopy (PALM), the "bottom up" approach is chosen with localizing single molecules in modest numbers to allow spatial localization which is far more precise than the resolution. To this end, photoswitchable proteins in their dark ground state are illuminated with a very weak "switching on" light intensity, and thereby only sparse photoactivation is generated. With the read-out light, fluorescence is detected only from those molecules which have been switched on in the previous step. This fluorescence is read out till the "on-state"-molecules are bleached and their individual position is localized afterwards with nanoscale precision. Under the uncertainty of having switched on probably more than one molecule within a confocal Airy disk, the resolution of PALM is governed by the localization accuracy of a single molecule given by the number of detected fluorescence photons, i.e., bright fluorophores are needed. The described process is iterated until all molecules have been read out once and bleached by this process. Finally the image is reconstructed taking all detected position of individual molecules into account. The process being comparably slow, the acquisition time is many hours. Moreover, PALM must rely on a mathematical restoration techniques to extract the spatial information of the image, whereas such techniques are only additional tools in the RESOLFT concept, e.g. one can exploit a-priori knowledge of the effective PSF by applying deconvolution algorithms. PALM was shown to be applicable to cellular imaging, however, the necessity of cutting back background signal made sample slicing inevitable, hence not being live-cell compatible in this stage of development. Nevertheless, the method showed another powerful approach of breaking the diffraction barrier by introducing a spectroscopic dimension in the working principle of the microscope, just like RESOLFT microscopy does. A very similar approach was independently chosen by introducing the STORM (stochastic optical reconstruction microscopy) concept ([24]). Here, not photoswitchable proteins but photoswitchable fluorophores, namely Cy5, are used for reversibly switching them on an off while again reading out only a small fraction of the whole molecule ensemble at the same time thus being able to determine their individual positions. The method was proven by labeling DNA-strands with Cy5 in defined distances and resolving those distances as being far below the diffraction barrier. To complete the very recent implementations

of subdiffraction imaging, the realization of nonlinear structured illumination should be mentioned ([25],[26]). Here the subdiffraction information is generated by illuminating the sample with a single, modulated wide-field intensity distribution, e.g. an interference pattern, and saturating the level of excitation. Depending on the accessible saturation level, more and more harmonics come into play thus transmitting higher spatial frequencys through the microscope. In the described way this method can extend the resolution which is only being limited by photobleaching. In this implementation bleaching mainly occurs due to the necessity of oversaturation of the excited state A. Additionally, the user is only provided with negative images, which makes deconvolution techniques inevitable. In fact, the method can also be judged as a wide-field implementation of the RESOLFT concept, which is not necessarily relying on focused light as illustrated in Fig.1.1. Recently this was consequently proven with the switchable protein FP595, implemented in a wide-field STED technique ([27]).

The diffraction barrier has thus been ultimately broken and the belief in this achievement seems to be established. Therefore fundamentally new ways of looking deeper into the structures and functionality of cells is open.

1.3 STED-microscopy

The depleting mechanism of the fluorescent state in STED-microscopy is illustrated in Fig.1.2. In a STED-microscope the deexcitation of fluorescence, a necessity originating
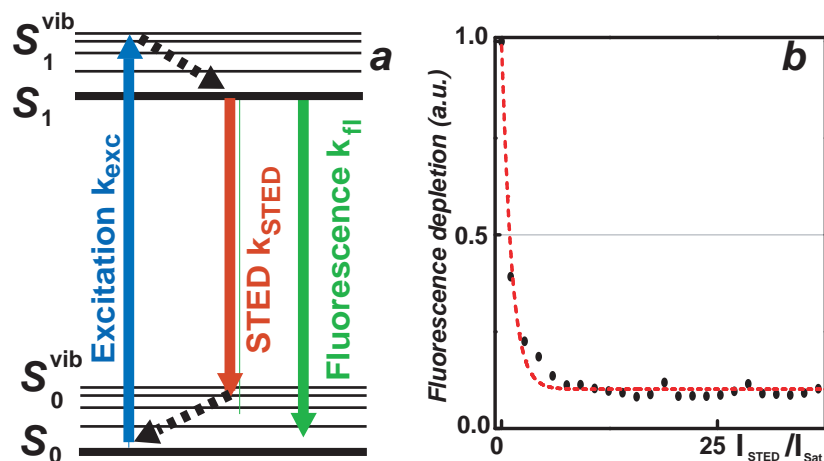
Figure 1.2: (a) **Basic energy states of a fluorescent molecule.** (b) **Typical measurement of the depleting efficiency of the STED beam depending on the applied STED intensity I_{STED}. For explanation see text.**

from the RESOLFT-concept, is achieved by stimulated emission. This effect was already predicted in 1917 by A. Einstein ([28]) and is the key mechanism in the laser working principle. Fig.1.2 (a) shows the basic energy states of a fluorescent molecule. After excitation of a fluorescent molecule in its ground state S_0 into higher vibronic levels of the first excited state (S_1^{vib}), the molecule undergoes a fast relaxation process ($\tau_{vib} \approx 0.1$-10 ps) into the vibronic ground state of S_1. Therefore a red shifted second laser beam (STED pulse) can efficiently couple into the populated state S1 and force the molecules into the ground state S_0^{vib} by stimulated emission, but cannot reexcite the molecules from the ground state S_0. The latter holds true, since the deexcited molecules also undergo fast relaxation ($S_0^{vib} \rightarrow S_0$), hence the depleting light intensity does not provide enough energy for reexcitation. Since the depleting efficiency must overpower the decay of spontaneous fluorescence emission ($k_{fl} \approx$ ns), the depleting rate k_{STED} has to fulfill the condition $k_{sted} >> k_{fl}$, with $k_{STED}=\sigma_{STED}I_{STED}$. Here σ_{STED} denotes the molecular cross-section at the depleting wavelength and I_{STED} the intensity of the depleting beam. This relationship determines the power level of effective STED depleting to be in the order of MW/cm^2 (also see chapter 3.2).

Mathematically, the four level system consisting of S_0, S_1, S_0^{vib} and S_1^{vib} can be modelled by a set of four differential equations. For a different purpose, a similar set of equations was solved in chapter (2.3). Therefore the result is directly presented here (for a detailed description and discussion see [29]). The population of the excited state niveau S_1 can be approximated immediately after the STED pulse duration to be

$$N_{S_1} \approx N_0 exp(-\sigma_{STED}I_{STED}) = N_0\eta(I_{STED}), \tag{1.4}$$

η is called the STED suppression coefficient, since it describes the amount of fluorescence inhibition (also compare with Fig.1.1 (a)). Such experimental depleting curves can be directly measured (Fig.1.2 (b)) and determine the performance of the fluorescent dye under STED conditions, hence the performance of the STED-microscope. Unfortunately, a theoretical prediction of the saturation level is difficult since intrinsic molecule specific entities like the cross sections σ are involved, why a screening of different fluorescence species becomes necessary. The most important aspect of (1.4) is the strongly nonlinear dependence of the remaining fluorescence on the STED intensity I_{STED}, hence creating the saturation behaviour (Fig.1.2 (b)). In fact, the clue to resolution enhancement stems from this nonlinearity since any light distribution in the focal plane can only feature diffraction limited features following the Abbe law.

To make this efficient fluorescence inhibition feasible for resolution enhancement, the last ingredient for STED-microscopy is the reengineering of the STED light distribution in such a way that it features an intensity zero, corresponding to the RESOLFT-concept. Several methods have been established to design the spatial light distribution of the STED-PSF, all of them utilizing phase manipulations of the depleting beam to generate destructive

interference in the center of the focus addressing lateral and axial resolution improvements. The latest method to deplete the outer areas of the excitation PSF laterally isotropic is to use circular polarized light in combination with a phase pattern of a helical phase ramp from 0 to 2π ([30]). To this end, a spatial light modulator (SLM) was introduced which is freely programmable in phase retardation on an array of 1024 x 768 pixels. The resulting light distribution is of doughnut shape featuring a singularity in the middle (Fig.1.3). This light distribution is coaxially aligned with the excitation beam and synchronized
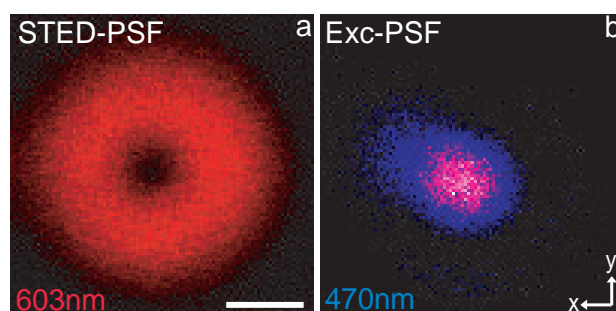
Figure 1.3: Light distributions in the focal plane of a STED microscope for lateral resolution enhancement. (a) STED-PSF generated by a helical phase ramp from 0 to 2π radians in combination with circular polarized light. (b) Conventional confocal excitation PSF. Scale bar = 200 nm.

in time to be shortly after the excitation pulse for most efficient depleting ([31]). With arbitrarily increasing the STED power above the saturation level, the resulting lateral spot size of non-depleted, excited molecules shrinks down to the molecular level (Fig.3.2). Limitations are observed in practice concerning the maximum power level tolerable for the molecules under photostable conditions and the imperfection of the intensity zero due to optical imperfections or scattering. A major part of this thesis deals with the questions of the maximum applicable STED peak powers and consequent optimization of the illumination pattern for reaching higher saturation factors, hence higher resolution, while simultaneously reducing photobleaching.

This thesis demonstrates major signal increase in fluorescence microscopy inherent with reduced bleaching in one- and two-photon microscopy in general by utilizing molecular dark state relaxation (D-Rex) between subsequent absorption events (chapter 2). This illumination technique in the low repetition rate regime (250 kHz) is combined with STED microscopy (T-Rex STED-microscopy), thus ramping up the resolution power in the focal plane below 20 nm. This unprecedented resolution ability was shown in various biological samples, including membrane patches, vesicle proteins on endosomes, and neurofilaments in the human brain (chapter 3). Moreover, the method was extended by designing the

first Dual-colour STED-microscope that reached superresolution in two independent channels, as shown in chapter 4. The concept of Dual-colour fluorescence nanoscopy opens up the possibility of studying different protein colocalizations with hitherto unprecedented detail. This new technique was verified by colocalizing two individual proteins on endosomes and in mammalian mitochondria, reaching nanoscale alignment preciseness of two subdiffraction resolution images.

# 2 Major signal increase in fluorescence microscopy through D-Rex

2.1 Illumination strategy of dark-state relaxation (D-Rex)

Two key properties of standard fluorescence microscopy, namely the spatial resolution and the limited signal yet call for major improvements ([32]). This chapter addressed the latter and uncovers an illumination scheme that increases the fluorescence yield substantially. Particularly this study is concerning different excitation modes for optimizing the illumination pattern in terms of fluorescence signal. To maximize fluorescence emission within a given time span, it is generally desirable to apply high excitation intensities. In most cases of imaging biological structures in cells it is simply not possible to enhance the signal by increasing the concentration of labeling, since the amount of the target proteins is usually part of the experiment itself. Therefore the signal of the individual molecule is to be addressed by increasing the excitation power level. Besides, high intensities are mandatory in multihoton microscopy ([6]). However, intense excitation results in both enhanced triplet buildup and photobleaching, and thus in losses in the fluorescence signal. Therefore, excitation times of less than a microsecond readily elicit a substantial triplet population, which suggests the use of fast scanning in conventional confocal microscopes ([33],[34],[35]).

In the following will be shown that the total number of photons emitted by a dye that is subject to intense illumination substantially increases when one ensures that fluorophores caught in an absorbing dark state, such as the triplet state, are not further excited ([36]). Consequently, judicious pulsed excitation allowing for dark od triplet relaxation (D-Rex or T-Rex), yields a lot more photons from the sample. This observation is relevant not only to microscopy but also to a range of bioanalytical techniques that, relying in fluorescence detection, are challenged by photobleaching. Pulsed excitation is preferred or even required for fluorescence lifetime imaging, STED microscopy, and for multi-photon excitation microscopy, as well as for the bioanalytical techniques relying on the same characteristics of fluorescence emission. In basically all of these fluorescence detection modes, pulse trains with a repetition rate f = 40-100 MHz are utilized. This rate is conveniently

provided in most pulsed lasers, such as the mode-locked Ti:Sapphire laser operating at f = 80 MHz. Moreover, the associated "illumination pause", $\Delta t = 1/f$ of 10-25 ns between two succeeding pulses is up to 10 times larger than the typical lifetime of the fluorescent state S_1 of most organic fluorophores. Shorter Δt increase the probability of illuminating molecules that are already excited, whereas longer Δt would leave the dye overly idle. Hence, not surprisingly, increasing Δt by decreasing f appeared unattractive.

Exceptions are rarely reported. For example, an amplified Ti:Sapphire system emitting at f = 0.2 MHz has been sporadically used in two-photon microscopy to benefit from the 400 times more intense pulses ([37]) allowing deeper penetration into live brain ([38]) or into tissue. In another experiment, widefield one-photon excitation with a pulsed laser diode at f = 6 kHz has been used to saturate the fluorescent S_1 state and for technical convenience ([26]). However, having relied on a single value of f and having targeted different purposes, these works have not recognized the general relationship between Δt and the signal magnitude. Here is shown that intermissions $\Delta t \approx$0.5-2 μs boost the number of photons emitted from a molecule before bleaching. Increasing Δt enables the spontaneous
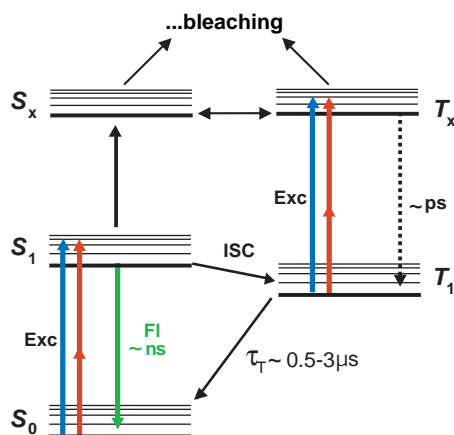

Figure 2.1: Energy diagram of a typical organic fluorophore, indicating the major molecular pathways for excitation (Exc), fluorescence (Fl), relaxation (dashed line), and photobleaching: singlet states: S_0, S_1, $S_{n>1}$, triplet states: T_1, $T_{n>1}$. Due to the chemical fragility of the triplet system, the excitation of T_1 is an effective bleaching pathway. While the lifetime of the fluorescent state S_1 is $\approx$ 1 ns, that of the vulnerable T_1 is by 3 orders of magnitude longer: $\approx$ 1 μs.

relaxation of this state, thereby avoiding its pile-up and its excitation to a further reactive state ([39],[40]). The primary candidate for this dark state is the molecular triplet state T_1, because, in most fluorophores the T_1 reportedly relaxes within $\approx$ 1 μs under ambient conditions ([41]). These states and the associated pathways of excitation and photobleaching are illustrated in Fig.2.1. This finding holds both for intense one- and

inherently intense two-photon molecular excitation.

2.2 Experimental fluorescence gain for ONE- and TWO-photon excitation

Here I present the study of the role of dark- or triplet state relaxation in pulsed mode illumination by gradually reducing the repetition rate f from 40 MHz down to 0.5 MHz, which is the same as expanding the inter-pulse distance Δt from 25 ns to 2 μs. Two
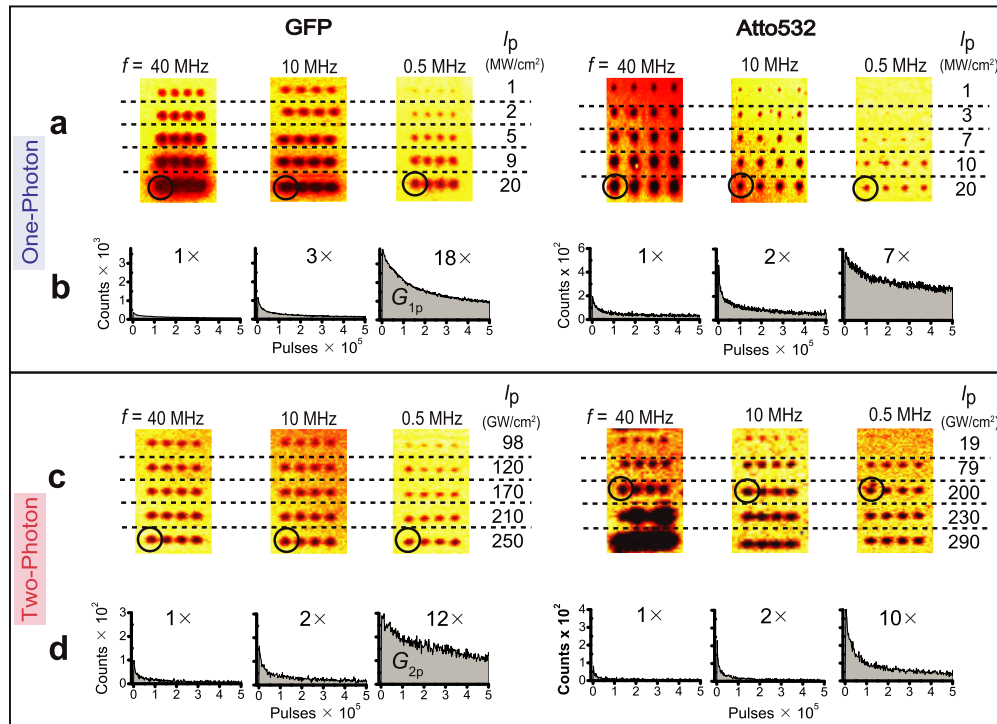
Figure 2.2: **Photobleaching of GFP and Atto532 decreases with interpulse break $\Delta t = 1/f$ for one- and two-photon excitation. (a,c) Fluorescence images of the fluorophore layers (7 x 10.5 μm) after illumination with varying repetition rates f and pulse peak intensities I_P. The horizontally aligned spots were subject to the same I_P. In each panel the number of excitation pulse was the same for all exposures. (b,d) show decrease in fluorescence observed at the spot marked in (a) and (c), respectively, its integral giving the total signal G_{1P} and G_{2P} for one- and two-photon excitation. Note the increase of the initial peak with increasing Δt. The magnification factors indicate the relative increase of G_{1P} and G_{2P}.**

fundamentally different fluorophores are chosen: Atto532 and GFP. The first is a Rho-

damine dye known for its photostability, low intersystem crossing to the triplet state (< 1 %), and high fluorescence yield. Atto532 emits in the 540-580 nm wavelength range and is used for labeling peptides and proteins, as well as for single molecule imaging. GFP is the archetype of the genetically encodable fluorescence markers. The fluorophores have been prepared as thin layers on a glass cover slip and covered with the mounting medium mowiol. This measure avoided molecular diffusion as a source of signal replenishment during photobleaching. To quantify photobleaching I irradiated the layers with a stationary beam focused to a ≈ 200 nm diameter spot (experimental setup see A.1). The panels in Fig.2.2 (a,c) show images taken from the layer after completion of the measurements. Dark areas signify the spots at which the signal was recorded, with the darkness being a measure of the bleaching occurred. Besides f, I also varied the pulse peak intensity I_P. There were actually five values of I_P both for one- and two-photon excitation applied. For each pair f and I_P, four runs were recorded, arrayed in the same line. Recording the fluorescence as a function of time indicated the photobleaching rate, whereas the integration of the fluorescence over time disclosed the total signal G_{1P} and G_{2P} gained by one- and two-photon excitation, respectively (b,d). Importantly, all runs to be compared were performed with the same total number of pulses, irrespective of the repetition rate, because I compensated the reduction of f by concomitantly extending the exposure time.

Fluorescence gain for ONE-photon excitation

The total illumination time for one-photon excitation (470 nm, pulse width $\tau_p =$100 ps) of Atto532 at f = 40 MHz, 10 MHz, and 0.5 MHz was 35 ms, 140 ms, and 2.8 s, respectively, implying that the spots were exposed to 1.4 x 10^6 pulses in all cases. For GFP the number of excitation pulses was 2.8 x 10^6. Photobleaching increased with increasing I_P (Fig 1a). Although this finding may arguably be expected ([42]), less expected is the fact that photobleaching is substantially weaker at the lower f.

The fluorescence as a function of the number of excitation pulses applied is plotted in (Fig.2.2 (b)). In fact, these curves quantify the initial fluorescence strength along with its decrease for the first 5 x 10^5 pulses. Each data point represents the signal accumulated from 2000 pulses (1000 pulses for one-photon excitation of Atto532). Being recorded at f = 40, 10, and 0.5 MHz, the curves reveal that increasing Δt elevates the signal dramatically. The elevation is observed both for the signal generated by the first pulses applied on the spot (note the initial peak in Fig.2.2 (b)) and for the integrated one-photon generated signal G_{1P}. For example, the curves in (b) indicate that the reduction of the repetition rate from f = 40 MHz to 0.5 MHz for one-photon excitation with $I_P \approx 20$ MW/cm^2 increases the G_{1P} from GFP by 18-fold and that from Atto532 by 7-fold. The actual improvement is larger because the curves in (b) just show the signal for the first 5 x 10^5 pulses. The signal G_{1P} gained from 1.4 x 10^6 pulses is shown in Fig.2.3 (a) as a function of Δt. The data shows that the signal improvement actually is by 20-fold for GFP and by

8-fold for Atto532. I plotted G_{1P} as a function if I_P ranging up to 50 MW/cm^2 (Fig.2.3 (b)); here $\Delta t = 1/f$ is used as a parameter. For all values of I_P the maximum G_{1P} is attained at the highest Δt. These results underscore that Δt plays a decisive role in keeping the dye fluorescent. Moreover, the most significant leap occurs between $\Delta t = 0.1$ and 1 μs. This observation indicates that the primary mechanism of photobleaching of Atto532 and GFP is the absorption of a dark state with a lifetime of $\approx 1\mu s$ (Fig.2.3 (a)).
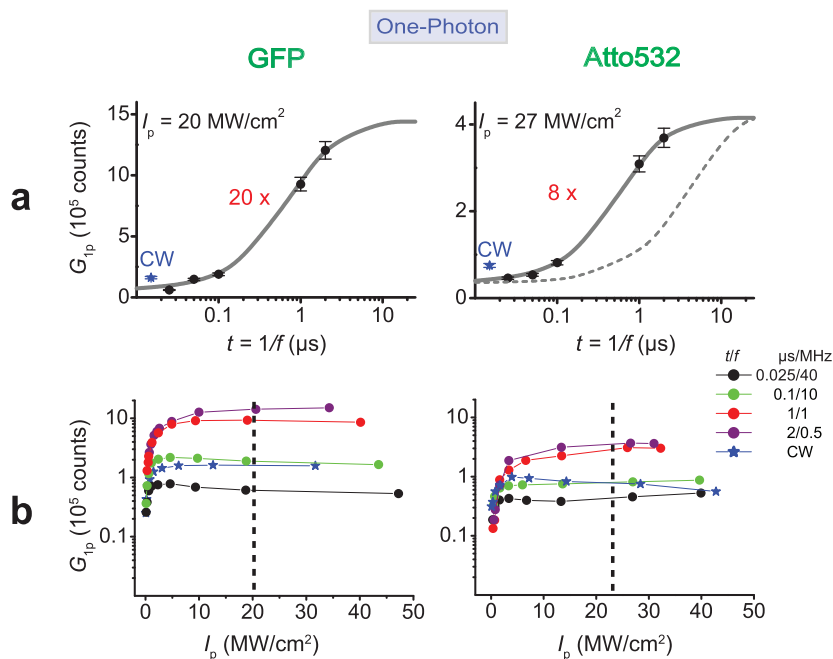
Figure 2.3: **Total fluorescence signal generated by one-photon excitation (G$_{1P}$) for GFP and Atto532 for a given number of excitation pulses (1.4 x 10^6). (a) G$_{1P}$ as a function of $\Delta t = 1/f$. The magnification factors indicate the relative increase in total fluorescence. The s.d. of 5-10 % were determined from five replicate measurements. The solid lines represent an exponential fit to the data, mimicking the extent of the decay of a nonfluorescent dark (triplet) state of 1 μs lifetime between two subsequent pulses. Note that an optimal gain in G$_{1P}$ is predicted for 100 kHz, close to the samllest applied rate of 500 kHz. In the case of a 5-μs lifetime (dashed line), the optimal frequency shifts to lower repetition rates. (b) G$_{1P}$ as a function of the pulse peak intensity I$_P$ with Δt as parameter. The number of excitation photons and illumination time of continuous wave (CW) illumination was the same as that of its 40 MHz pulsed counterpart. Strong excitation intensities and pulsed excitation with $\Delta t < 1\mu s$ lead to smaller total fluorescence yield per fluorescent molecule.**

It is now interesting to compare the G$_{1P}$ values found for the pulsed illumination with

those for continuous wave (CW) exposure (Fig.2.3). As there is no dedicated intermission in the CW case, the population of the dark state and its excitation just depend on the continuously applied intensity I_{CW}. The CW data is gained by illuminating for the same illumination time and with the same time-averaged intensity $I_{CW} = I_P(\tau_P f)$ as in the 40Mhz case. The latter condition is like spreading out the photons of a pulse across the 25 ns break. At the 488 nm wavelength used for continuous-wave illumination, the absorption cross-section is higher at the 470 nm wavelength used for pulsed illumination. Nevertheless, for all intensities, the fluorescence signal is by up to 5-fold (GFP) and by up to 8-fold (Atto532) smaller than in the 0.5 MHz case. Note that the maximum applied intensities of up to I_{CW} of $\approx 200 \text{kW/cm}^2$ were about an order of magnitude above those usually applied in fluorescence microscopy ([39]), but they were in the range of what is routinely used in single-molecule experiments in solution ([40]). Hence, an intense CW illumination cannot provide the same total signal that is provided by pulsed D-Rex illumination.

Fluorescence gain for TWO-photon excitation

I also measured the total fluorescence signal generated by two-photon excitation (800 nm, pulse width $\tau_p = 200$ fs) shown in Fig.2.4. Like in the one-photon mode, the total number of pulses was 1.4 x 10^6 in all cases. For pulse peak intensities $I_P \approx 300 \text{ GW/cm}^2$, enlarging Δt from 25 ns to 2 μs increased the total two-photon fluorescence yield G_{2P} by $\approx$ 25-fold for GFP and $\approx$ 20-fold for Atto532.

Fig.2.4 (b) displays G_{2P} as a function of I_P, with $\Delta t = 1/f$ as parameter. Again, G_{2P} becomes saturated with increasing I_P; the saturation level strongly depends on Δt. Yet again, larger Δt enable more emissions and once more, both GFP and Atto 532 exhibit the decisive leap when stepping up from $\Delta t = 0.1$ to 1 μs. This finding showed again that a ≈ 1 μs dark state played a key role in the fluorescence bleaching (and saturation) mechanism. Similarly to the one-photon case, a larger Δt leads to a stronger prompt signal (compare Fig.2.2(d)), because all non-bleached molecules are in the S_0 at the time of arrival of the following illumination pulse. This similarity suggests the comparison of the yield for both excitation modes, especially because two-photon excitation reportedly involves stronger photobleaching ([43],[44]). Therefore, I selected $I_P = 25 \text{ MW/cm}^2$ and 300 GW/cm^2, for the one- and the two-photon mode, respectively, and displayed the ratio G_{1P} / G_{2P} as a function of Δt (c). Interestingly this exhibits that, for $\Delta t \leq 0.1$ μs the G_{2P} was indeed up to 20-times lower than G_{1P}, but this adverse factor is below 10-fold at $\Delta t \geq 0.1$ μs, thus narrowing the gap. This finding indicates that in a multiphoton excitation modality, the intermission Δt are even more effective.
In addition, this observation provides further evidence for dark state absorption because in the multiphoton mode, the pulse intensity is larger than for its one-photon counterpart by orders of magnitude. Once a molecule has passed to an absorbing dark state, such as
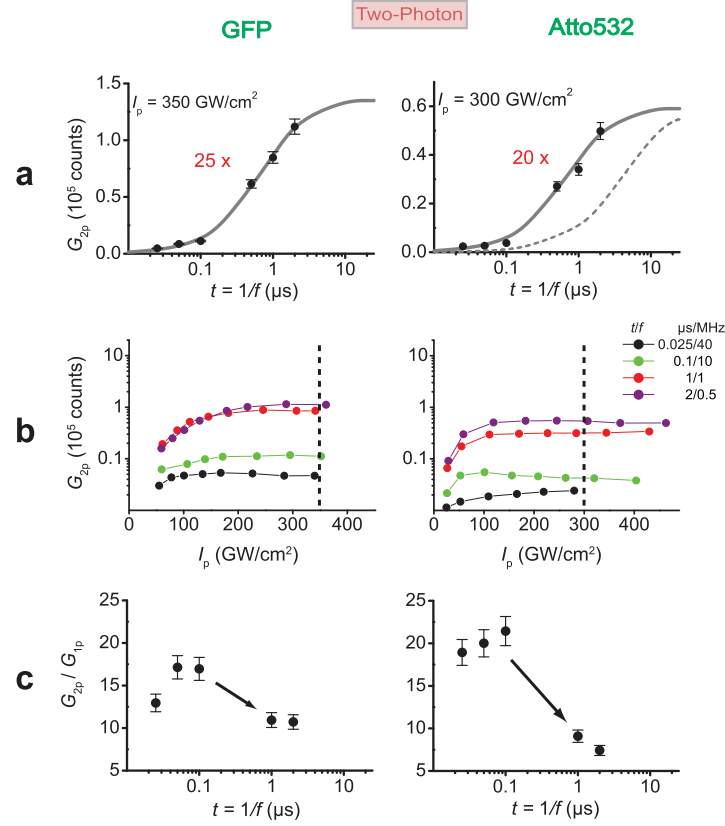
Figure 2.4: Total fluorescence signal generated by two-photon excitation (G_{2P}) for GFP and Atto532 for a given number of excitation pulses (1.4×10^6). (a) G_{2P} as a function of $\Delta t = 1/f$. (b) G_{2P} as a function of the pulse peak intensity I_P with Δt as parameter. The magnification factors indicate the relative increase. The s.d. of 5-10 % were determined from five replicate measurements. The gray lines reveal the extent of the decay of a nonfluorescent dark (triplet) state of 1 μs (solid line) and 5 μs (dashed line) lifetime in between subsequent pulses (c). Ratio of one- and two-photon generated fluorescence as a function of Δt, showing that the total fluorescence yield is lower for two-photon excitation than for its one-photon excitation counterpart, but the ratio decreases by two-fold for $\Delta t > 1$ μs.

the T_1, the molecule is confronted with a photon flux that readily leads to a single (and possibly also multi-photon) excitation to the $T_{n>1}$ (compare Fig.2.1). The occurrence of such processes is exacerbated by the fact that the molecular cross-section for a one-photon absorption of the T_1 state is $\sigma_T \approx 10^{-17}$ cm^2 ([45]). Given $I_P = 300$ GW/cm^2 and a photon energy of 2.5×10^{-19} J, the excitation rate of a T_1 molecule is ≈ 1 event per ($\tau_p \approx 200$ fs) pulse, i.e., the $T_1 \longrightarrow T_{n>1}$ process is nearly saturated. Therefore, once the molecule has crossed to the T_1, the molecule is prone to be excited to a more

fragile state. Furthermore, the $T_{n>1}$ molecule can absorb another photon from the same pulse, thus setting off a cascade of several consecutive one-photon excitations leading to increasingly fragile states. In fact, starting from T_1 ($\approx$ 1.9 eV) the combined energy of about 2-3 photons of $\approx$ 800 nm wavelength (i.e., $\approx$ 2-3x1.56 eV) reaches the typical ionization energy of $\approx$ 5-6 eV of, for example, Rhodamine dyes. This scenario explains why the D-Rex illumination modality is so effective.

Influence of the pulse length τ_p in TWO-photon excitation

In fact, there is further evidence to be found for the previously discussed scenario when scrutinizing the role of the pulse duration τ_p on G_{2P}. Accommodating $\tau_p = 0.2, 1,4$ both for 40 ps for f = 40 and 0.5 MHz pulse trains, in Fig.2.5 G_{2P} is plotted as a function of $I_P^2 \tau_P$, which is proportional to the probability of two-photon excitation within a single pulse. Increasing τ_P by a factor m while keeping this ability constant, entails an I_P that
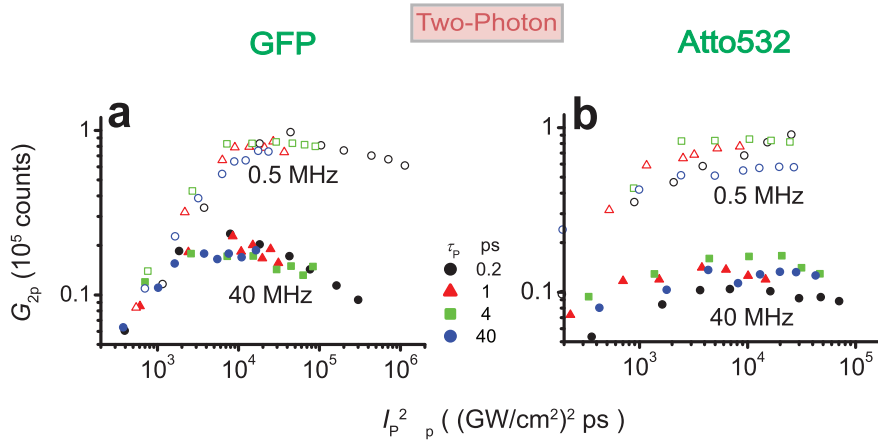

Figure 2.5: **Dependence of photobleaching on the pulse width (τ_p) for two-photon fluorescence excitation of GFP (a) and Atto532 (b). The curves show G_{2P} for 0.5 MHz (open circles) and 40 MHz (filled) with increasing value of $I_P^2 \tau_P$ giving the ability of a pulse to excite in the two-photon mode. The latter is maintained when varying the pulse widths from τ_p = 200 fs to 40 ps. Pulses that are longer by m feature a pulse energy that is larger by $\sqrt{m}$ and an I_P that is lower by the same factor.**

is lower by $\sqrt{m}$. By the same token, the pulse energy, given by $\approx I_P \tau_P \approx (I_P/\sqrt{m})$m, is larger by $\sqrt{m}$. τ_p was adjusted to the values 0.2, 1, 4, and 40 ps both for f = 40 and 0.5 MHz pulse trains. Spanning over two orders of magnitudes, the variation in τ_p exceeds by far the 100 fs - 2 ps span encountered in practical two-photon microscopy ([46]). Fig.2.5 reconfirms that stepping down f leads to a substantial increase in G_{2P}, but changing τ_p by m = 200 and hence the pulse energy by 14-fold does not display a considerable effect

on G_{2P}. There are two reasonable explanations for the fact that the reduction in the two-photon fluorescence yield G_{2P} (caused by dark state population and absorption) does not vary with $I_P^2 \tau_P$. The first one is that all the excitation pulses are so intense that they deplete the ground state S_0, thus neutralizing any intensity or pulse length dependence of the transition to the S_1 and hence to the dark state, such as the T_1. This scenario is unlikely. The second explanation is consistent with the one given above: following a two-photon excitation to the S_1, the molecule crosses to the dark state (e.g. the T_1) which is then subject to a further nearly saturated excitation (e.g. to $T_{n>1}$) elicited by one of the following pulses. The saturation is either provoked by large I_P for short ($\tau_p = 200$ fs) or by repetitive excitation to $T_{n>1}$ within the same long pulse ($\tau_p = 40$ ps) with the lifetime of $T_{n>1}$ being ≈ 200 fs. The saturation eliminates any dependence on intensity or pulse width.

Increased image brightness

D-Rex illumination conditions yield brighter two-photon images of Escheria coli cells expressing the Venus yellow fluorescent protein ([47]) (Fig.2.6). In each recording were 4×10^4 pulses of $I_P = 350$ GW/cm^2 per 62.5 nm quadratic pixel applied, but in (a) $\Delta t = 1$ μs, whereas in (b) $\Delta t = 0.025$ μs. The brightness histogram in (c) reveals that the 40-fold increase in Δt provided an approximately 3 times brighter image. In light of the fact that Venus is a further member of the GFP family, the data of Fig.2.6 underscores the relevance of D-Rex for other fluorophores.
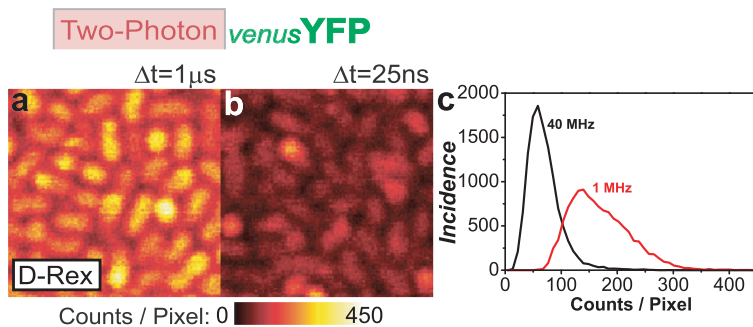
Figure 2.6: **Two-photon fluorescence images of Escherichia coli cells expressing the fluorescent protein Venus are brighter when recorded in the D-Rex mode. Pulse intermissions $\Delta t = 1$ μs and 0.025 μs in (a) and (b), respectively. The same number of excitation pulses was ensured for both images by adjusting the exposure time accordingly (40 ms in (a) and 1 ms in (b)). Scale bar = 1 μm. (c) Histogram of the counts per pixel of the images of (a) (red) and (b) (black).**

Conclusion

The fluorescence generated by intense one- and two-photon excitation from a molecule can be fundamentally increased by applying light pulses with a rate f $<$ 1 MHz. Photobleaching is reduced, because intermissions $\Delta t = 1/f > 1~\mu s$ between succeeding pulses enable the decay of an absorbing dark state of similar lifetime. The primary candidate for this state is the molecular triplet state T_1, because the 1 μs relaxation time coincides with the T_1 lifetime of most fluorophores under ambient conditions. A further reason is that the T_1 is a feature of organic fluorophores and fluorescent proteins alike. Also G_{2p} slightly varies with the sample preparation. For example, in the data of Fig.2.5 the gain for GFP is lower as compared to that in Fig.2.4 which was recorded on a sample that was 10 days old. As the embedding medium mowiol solidifies with time, the concentration and mobility of oxygen decrease, increasing the T_1 lifetime. A shortened T_1 lifetime lowers the T_1 pile-up and abates the effect of D-Rex microscopy. In contrast, an increased dark state lifetime will enforce f$<<$1 Mhz (Fig.2.3 (a) and Fig.2.4 (a)). Hence, while the boost factor depends on the chemical environment, most, if not all fluorophores are expected to exhibit gain under D-Rex conditions. In fact, ad hoc screening of Rhodamine6G, Coumarin120, DAPI and the enhanced yellow fluorescent protein have also exhibited a 5-15-fold fluorescence increase.

As dark state photobleaching is reduced by D-Rex illumination, $S_1 \longrightarrow S_{n>1}$ induced photobleaching becomes more prominent. Besides, non-excited T_1 molecules also undergo bleaching. There should be mentioned that D-Rex illumination is less important for one-photon excitation at low intensities as can also be inferred from the G_{1P} data in Fig.2.3 (b). Low intensities hardly generate cascaded excitation processes, rather the molecule relaxes to the S_0 before absorbing another photon. By contrast, in a typical two-photon microscope operating at 80 MHz and scanning with a double-pixel dwell time of 5 μs, a molecule is hit by 400 pulses in a row at Δt = 12.5 ns with each pulse containing $\approx$ 1000 photons. Once it has passed to the T_1 it is confronted with these pulses, explaining why even fluorophores with a low (< 1 %) rate for $S_1 \longrightarrow T_1$ crossing, such as Atto532, exhibit a substantial gain by the D-Rex modality. Yet high intensities are also necessary in one-photon excitation to maximize signal and to cut down acqusition times. The data indicate that the D-Rex scheme allow the application of high intensities while still providing a high fluorescence yield.

In the following section the measured repetition rate dependence is simulated on basis of a detailed photophysical description of a fluorescent molecules regarding the argumentations previously discussed.

2.3 Simulation of the repetition rate dependence

The photophysical simulations will show that the fluorescence enhancement upon the decrease in the repetition rate arises from a significantly lowered triplet population, which leads to less ground-state depletion and less multi-step photobleaching. The simulation data will be compared to the measured (pulse peak) intensity dependence of the fluorescence signal observed within the first 2000 pulses of one- and two-photon excitation (Fig.2.7) of the Atto532 layer (i.e., the first observed fluorescence value of the decays of Fig.2.2 (b,d)). As illustrated in Fig.2.2, a significant increase in fluorescence signal of a factor of 3 in the case of one- and up to 6 for two-photon excitation is already observed for such short number of excitation pulses. A similar characteristic is observed for GFP.
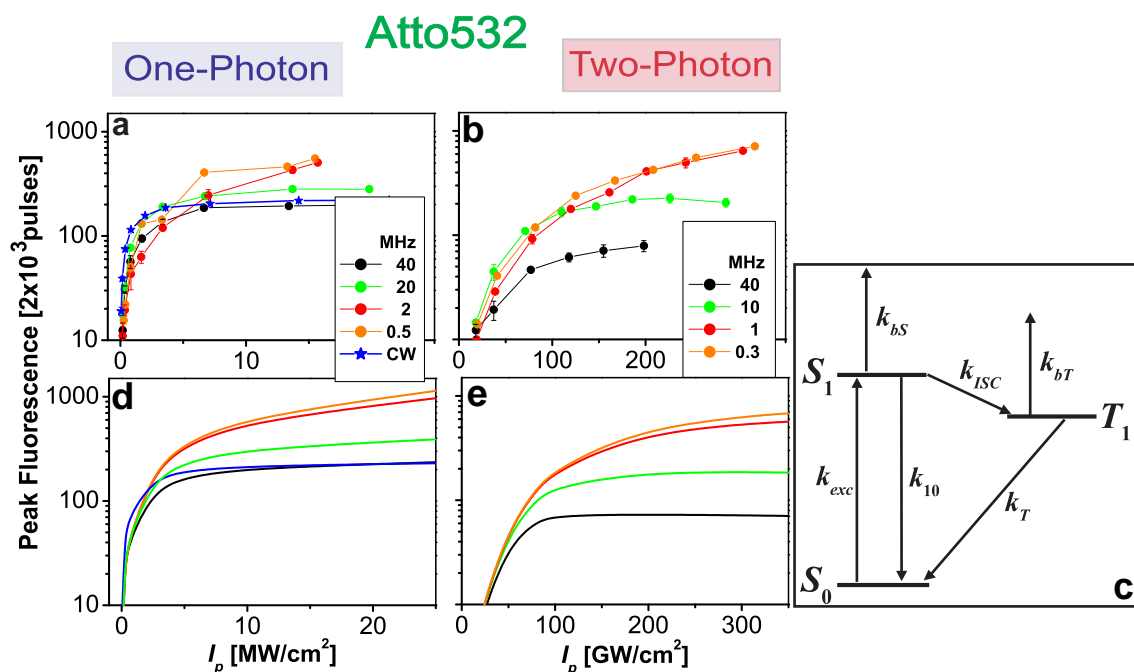
Figure 2.7: Photophysical description of the rise in fluorescence signal upon the reduction of the repetition rate for the Atto532 layer. (a and b) Fluorescence signal detected within the first 2000 pulses of one- and two-photon excitation, respectively, for increasing pulse peak intensity I_P and different laser repetition rates as labeled. The illumination time t_{exc} is thereby adapted to the varying repetition rate f and for CW excitation identified with t_{exc} = 0.05 ms of the 40 MHz experiment. (c) Photokinetic model with energy diagram of the dye molecule including three electronic levels and their transition and photobleaching rate constants. For details see text. (d and e) Simulation of the data of (a) and (b) applying the photokinetic model of (c).

Photophysical Model

The photophysical model is based on three electronic levels; singlet ground and first excited state S_0 and S_1, respectively, and lowest excited triplet states T_1 (Fig.2.7 (c)). The kinetic rate constants of the underlying transitions define the kinetic rate system of the time dependent relative populations of the different states as well as the photobleaching kinetics.

$$
\begin{pmatrix} \dot{S}_0(t) \\ \dot{S}_1(t) \\ \dot{T}_1(t) \end{pmatrix} = \begin{pmatrix} -k_{exc}(t) \\ k_{exc}(t) \\ 0 \end{pmatrix} S_0(t) + \begin{pmatrix} k_{10} \\ -k^*(t) \\ k_{ISC} \end{pmatrix} S_1(t) + \begin{pmatrix} k_T \\ 0 \\ -k_T - k_{bT}(t) \end{pmatrix} T_1(t), \quad (2.1)
$$

with $k^*(t) = k_{10} + k_{ISC} + k_{bS}(t)$. $k_{exc}(t)$ determines the rate constant for excitation from S_0 to S_1 and is given by the product $\sigma_{exc}\gamma I(t)$ for one- and $(\sigma_{exc}/2)\gamma^2 I(t)^2$ for two-photon absorption with the one- and two-photon absorption cross sections σ_{exc} and δ_{exc}, respectively, and the reciprocal photon energy γ ([44],[48]). The time dependence of k_{exc} results from the time course of the excitation intensity $I(t)$, which follows the pulse shape and the repetition rate in the case of pulsed excitation and is constant for CW excitation. The reciprocal fluorescence lifetime $k_0 = k_{10} + k_{ISC}$ is made up of the deexcitation rate constant k_{10} from S_1 to S_0 and the rate constant for intersystem crossing k_{ISC} denoting the S_1 to T_1 transition. k_T depicts the inverse lifetime of the triplet state following the return from T_1 to S_0. Photobleaching is introduced by the microscopic rate constants $k_{bS}(t)$ and $k_{bT}(t)$ starting from the excited states S_1 and T_1, respectively. Both rate constants comprise direct photoreactions from S_1 and T_1 with rate constants k_{bS1} and k_{bT1} and multi-step photobleaching from higher excited electronic singlet and triplet states (k_{bSn}, k_{bTn}) (Fig.2.2 (c)).

$$
k_{bX}(t) = k_{bX1} + k_{X1n}(t)/(k_{X1n}(t) + k_{Xn1})k_{bXn} \qquad (X = S \ or \ T) \qquad (2.2)
$$

Multi-step photobleaching follows an additional absorption step to higher excited electronic states with the rate constant for excitation $k_{X1n}(t) = \sigma_{X1n}\gamma I(t)$, the corresponding absorption cross section σ_{X1n}, and the rate constant k_{Xn1} for deexcitation to the lowest excited electronic state (X = S or T). In this model, vibrational substates are disregarded due to their comparatively short lifetime. Due to the same reason, the populations of the higher excited electronic states do not have to be explicitly calculated, rather are the essential reaction rates expressed in terms of the relative populations $k_{X1n}(t)/(k_{X1n}(t) + k_{Xn1})$. The time dependent populations of each electronic level can be calculated by solving equation (2.1) for a given time course of the excitation intensity $I(t)$ and with initial populations $S_0(0) = 1$ and $S_1(0) = T_1(0) = 0$. $S_1(t)$ on the other hand gives an estimate of the fluorescence signal $F(t_{exc}) \approx \int_0^{t_{exc}} S1(t)dt$ gathered for an illumination time t_{exc}. The proportionality thereby includes experimental and molecular constants such as the detection efficiency of the setup and the fluorescence quantum yield of the dye.

Simulation of experimental data

Fig.2.7 (d,e) shows the simulations of the experimental data (Fig.2.7 (a,b)), applying photokinetic parameters $\sigma_{exc} = 1\text{x}10^{-17}$ cm^2 for 470 nm and $3\text{x}10^{-17}$ cm^2 for 488 nm and $k_0 = 5\text{x}10^8$ s^{-1} determined from control experiments of absorption spectrum and time-correlated single-photon counting (TCSPC), $\delta_{exc} = 2\text{x}10^{-48}$ cm^4 s, $k_T = 5\text{x}10^5$ s^{-1}, k_{bS1} $= k_{bT1} = 500$ s^{-1}, $\sigma_{S1n} = 1\text{x}10^{-17}$ cm^2 and $\sigma_{T1n} = 5\text{x}10^{-17}$ cm^2 and $k_{Sn1} = k_{Tn1} = 5\text{x}10^{12}$ s^{-1} estimated from parameters known for the similar organic dye Rhodamine6G ([44]), and $k_{ISC} = 5\text{x}10^7$ s^{-1} and $k_{bSn} = k_{bTn} = 3\text{x}10^8$ s^{-1} for one- and $5\text{x}10^{10}$ s^{-1} for two-photon excitation adapted to fit the experimental data best. For both one- and two-photon excitation, the photophysical model describes the experimental intensity dependence of the fluorescence signal well, especially with respect to the saturation behaviour and the dependence on the repetition rate.

Calculation of the fluorescence signal following two-photon excitation at 40 MHz with (black line in Fig.2.8) and without triplet state population ($k_{ISC} = 0$, black dotted line in Fig.2.8) and without multi-step photobleaching from the triplet state ($k_{bTn} = 0$, gray dotted line in Fig.2.8) disclose the population of the triplet state as well as multi-step photobleaching from higher excited triplet states as the most severe limit in the fluorescence yield. It is actually the negligible population of the triplet state in the case of
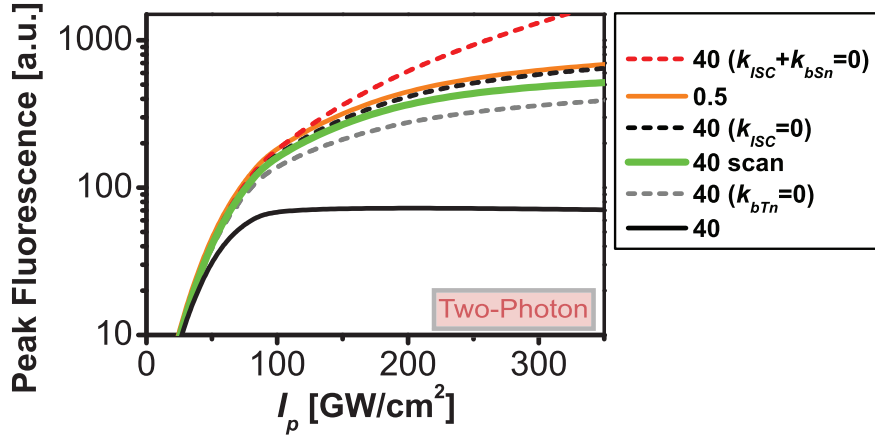
Figure 2.8: **Simulation of the fluorescence signal detected within the first 2000 pulses of the Atto532 layer for two-photon excitation with 40 MHz (label "40") and 0.5 MHz repetition rates (label "0.5") and for varying values of the photokinetic parameters. Comparison with the conditions of fast beam scanning frequencies (label "40 scan") with an effective dwell time of 100 ns (corresponding to 4 pulses at 40 Mhz) and full relaxation of the dark state before each following scan. For details see text.**

excitation with low repetition rates, which elicits the boost in fluorescence. This becomes obvious from the coinciding fluorescence signal expected for 40 MHz in the case of repressed triplet build-up compared to 0.5 MHz excitation (black dotted and orange lines in Fig.2.8). Actually, no difference in fluorescence signal is predicted with $k_{ISC} = 0$ or k_{bTn} = 0 in the case of 0.5 MHz (coinciding with the orange line in Fig.2.8). The fluorescence gained with a lowered repetition rate thus comprises reduced ground-state depletion, i.e., reduced fluorescence saturation and less multi-step photobleaching from higher-excited triplet states. It is the extended time lag between subsequent laser pulses, that allows the triplet state to relax to S_0, thereby preventing triplet pile-up or subsequent absorption to higher excited states. The calculations on the other hand reveal a marginal influence by direct photobleaching from S_1 and T_1 (k_{S1} and k_{T1}), as has been proposed before in the case of the high intensities used within confocal microscopy ([40]). In the case of repetition rates below 10 MHz, the fluorescence signal obtained by two-photon excitation almost reaches the signal level of one-photon excitation, eliminating limits of the signal-to-noise ratio in two-photon excitation fluorescence microscopy. Further improvements for both excitation modes can solely be achieved by minimizing residual multi-step photobleaching from higher excited singlet states ($k_{bSn} = 0$, red dotted line in Fig.2.8), e.g. by the addition of certain stabilizers ([49]).

CW excitation

The level of fluorescence signal gained by one-photon CW excitation (blue line in Fig.2.7 (d,e)) is as low as for one-photon pulsed excitation with repetition rates above 10 MHz. A similar consistence between CW and quasi-continuous excitation at 80 MHz has been reported for rhodamine dyes in aqueous solution ([40]). Both excitation modes, CW and quasi-continuous excitation at above 10 MHz repetition rates, do not allow essential depopulation of the triplet state in-between subsequent excitation events, thereby reinforcing analogue saturation and bleaching pathways via the enhanced triplet build-up.

Fast scanning

Implementing D-Rex by decreasing f is not optimal, because of the concurrent increase in recording time. The preferred implementation of the D-Rex modality is to scan the beam so fast, that succeeding pulses illuminate different molecules. This holds if the scanning speed is larger than the focal spot size divided by Δt. The ideal speed for a 40 MHz system is $\approx$ 200 nm/25 ns = 8 m/s. However, a relief is already predicted for slightly lower speeds, because they also reduce effective triplet built-up (thus minimizing the problem of image alignment during fast mirror scanning). Fast scanning rates utilize minimal dwell times, allowing no time for significant triplet build-up and thus no possibility of transitions to higher excited states. As simulated for 40 MHz two-photon excitation (green line in Fig.2.7), scanning dwell times as low as 100 ns reveal almost the same gain

in fluorescence signal and photostability as moving to repetition rates ≤ 1 MHz. For comparison and to achieve the same number of 2000 excitation pulses, the simulations assume 500-times repetition of the 100 ns scans, assuming complete relaxation of the triplet state between subsequent scans. The realization of such fast scanning experiments would therefore achieve the same improvements as the use of low repetition rates, however, in a much lower acquisition time, i.e., 50 μs compared to 4 ms for 0.5 MHz.

An elegant way of fast scanning is the application of spinning disks in which case the synchronization like for fast mirror scanning does not pose problems. Another option is to combine low-repetition-rate scanning with parallelized multispot or line-shaped illumination. The results also corroborate anecdotal reports that fast scanning microscopes bleach less and that high f lasers (1 GHz) do not provide the anticipated fluorescence flux. Finally should be noted that unlike the addition of antifade chemical agents, the D-Rex strategy is allphysical and hence compatible with live cells.

Conclusion

The simulation applies a basic photokinetic model, which is good enough to outline the underlying processes responsible for the experimental observations. However, from the data, I cannot really determine the exact details of the model as well as the real values of the corresponding photokinetic parameters. As an example, the value of $k_{bSn} = k_{bTn}$ of photobleaching from the higher excited triplet state should in principle be smaller for the case of two-photon excitation at 800 nm compared to one-photon excitation at 470 nm, inasmuch as the photon energy of 800 nm light is lower than that of 470 nm light. A lower energy results in a lower level of the higher excited electronic state and, thus, a lower efficiency of photobleaching. The contradiction of this findings, $k_{bSn} = k_{bTn} = k_{bXn}$ = 5×10^{10} s^{-1} for two- compared to $k_{bXn} = 3 \times 10^{8}$ s^{-1} for one-photon excitation, indicates further excitation steps to higher excited electronic states in the case of the extraordinary high photon densities applied for efficient two-photon excitation. Such photobleaching mechanism higher in order than three on the applied intensity has been examined several times before ([43],[50]) and is supported by the fact, that the lowest pulse intensities $I_P \approx 50$ GW/cm2 accessed in the two-photon experiments readily result in a saturated transition from the lowest to higher excited electronic states, $k_{X1n}(t)/(k_{X1n}(t) + k_{Xn1})$ ≈ 1. That is, the population of an excited state is immediately followed by subsequent absorption steps, resulting in extraordinary photobleaching efficiencies. Such a characteristic would for example not allow for the observation of a significant triplet population, and thus does not contradict the previous two-photon excitation fluorescence correlation spectroscopy (FCS) experiments in solution, which observed no triplet build-up at all in their correlation data ([49]).

2.4 Expectations of D-Rex application on STED-microscopy

With D-Rex having an impact on a variety of fluorescence techniques utilizing intense molecular excitation, this illumination scheme should facilitate new applications in STED-microscopy, too. Therefore studies were conducted to test D-Rex conditions for STED-microscopy, namely the effect of repetition rate reduction on the STED-efficiency (Fig.2.9) and the total bleaching behaviour (see chapter 3.1 and Fig.3.4), when the sample is illuminated under STED conditions.

When distinguishing the diverse interaction possibilities of the intense STED beam with the various molecular states of the fluorophore one has to keep in mind that the STED beam interferes with the dye in its excited state. Four different pump-probe conditions were investigated (Fig.2.9 (a)): (i),(ii) STED-mode: illumination with optimized inter-pulse distance of the excitation and STED beam for effective fluorescence depletion. The red beam is operated under common STED conditions, featuring long and short puls length, respectively. (iii, iv) "Reverse-mode": Illumination with reversed pulse order. The red shifted laser light (indicated in orange colour, Fig.2.9 (a)) arrives in time before the blue excitation light. This mode excludes a depleting effect of the red shifted beam, since the first excited state of the fluorescent molecule has already relaxed before the incidence of the STED pulse (the time gap between STED and excitation is ≥ 25 ns). Thus the STED beam only interacts with long living states (with $\tau >>$ ns), such as the triplet state. Again the red shifted beam is either featuring long (iii) and short (iv) pulse lengths of ≈ 300 ps and < 10 ps, respectively. Both pulse length conditions were provided by stretching the red laser beam via a pair of gratings or a 7 m single-mode fibre, respectively, thus varying the pulse peak intensity of the STED pulses of more than one order of magnitude, but keeping the total pulse energy (intensity values on the sample are ≈ 5 mW at 40MHz in both cases) constant. A higher pulse peak intensity makes nonlinear effects such as stimulated emission or excitation into higher electronic states more probable ([44]).

Fig.2.9 (b) depicts the repetition rate dependence of these four illumination conditions observed with 470 nm excitation light and 610 nm STED light on a dye layer of the organic dye Atto465, an acridine derivative. Note that the pulse peak intensity of the STED beam for a chosen pulse length was kept constant when stepping down the frequency in STED- and "reverse"-mode from 40 Mhz to 150 kHz, respectively. An acridine derivative was chosen as fluorescent label for this study, since it shows a very high triplet yield ([51]), pronouncing the D-Rex effect as discussed earlier in chapter (2.2). In particular two molecular transitions addressed by the intense red STED beam could be separately studied via repetition rate reduction and in combination with applying STED- (red
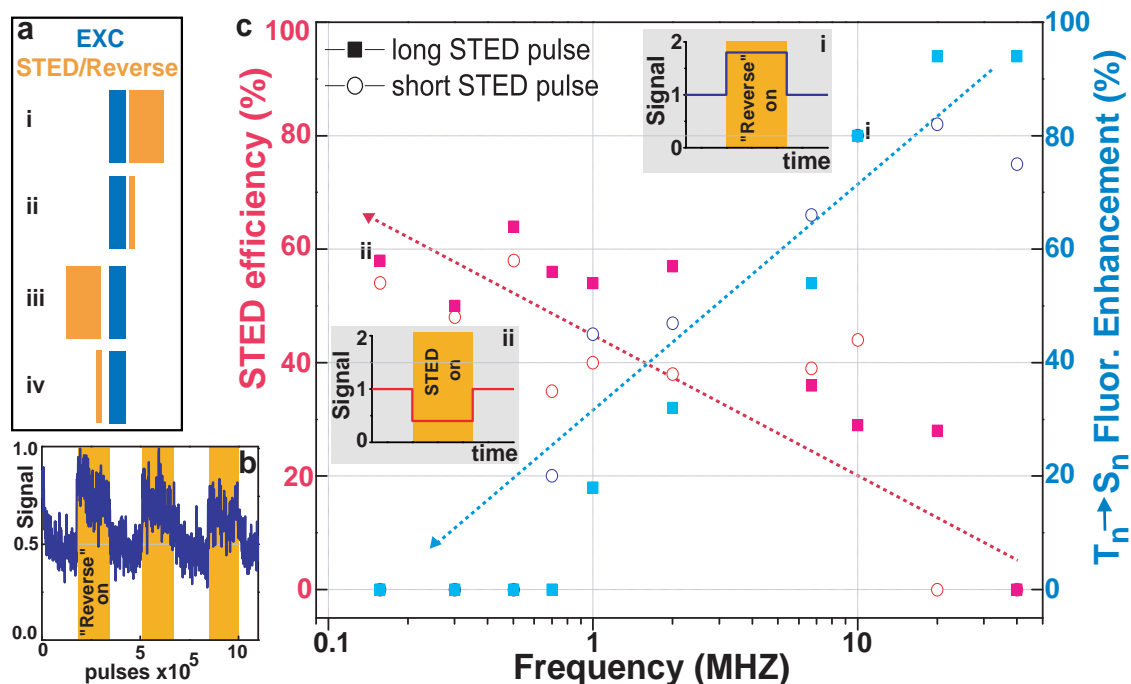
Figure 2.9: **Influence of the repetition rate on the STED-efficiency and fluorescence enhancement due to reverse intersystem crossing (ISC) ($T_n \longrightarrow S_n$).(a) Different illumination modes: (i) STED-mode, long pulse, (ii) STED-mode, short pulse, (iii)"Reverse"-mode, long pulse, (iv) "Reverse"-mode, short pulse. (b) Exemplified measurement at 40Mhz in mode (iv) illustrating the photoinduced fluorescence enhancement effect due to reverse ISC by the intense red beam. (c) Dependence of the STED-efficiency in case of STED mode (red colour) and of the fluorescence enhancement due to the reverse intersystem crossing in the case of the "reverse" mode (blue colour) on the repetition rate. (Inset i) Schematic signal enhancement due to reverse ISC by applying the "reverse" pulse mode in the high repetition rate regime (compare with the measurement in (b)). (Inset ii) Occurrence of fluorescence depletion due to STED by applying the STED mode in the low repetition rate regime.**

colour in Fig.2.9(b)) and "reverse"- illumination mode (blue colour in Fig.2.9(b)): STED depleting and reverse intersystem crossing (ISC) ($T_n \longrightarrow S_n$). The latter transition is an effective pathway for triplet depopulation, where the dye in its lowest excited triplet state T_1 is excited into higher excited triplet levels T_n. From T_n the dye can effectively cross back into the singlet system thus generating fluorescence emission as reported in ([52]). Photoinduced reverse ISC has therefore the potential to compromise the fluorescence depleting efficiency of the STED beam. Starting at high repetition rate (40Mhz) one can see a signal enhancement evoked by the red-shifted "reverse" pulse up to 90 % regarding the

fluorescence level reached by excitation only (Fig.2.9 (b)). With reducing the repetiton rate this enhancement in signal drops gradually to zero when reaching frequencies of $\approx$ 1 Mhz (Fig.2.9 (c)). Accordingly, the "reverse" pulse can no longer pump electrons from the triplet in the fluorescing singlet channel, as the long living dark (triplet) state is no longer populated at an interpulse distance of ≥ 1 μs. Obviously the red STED beam can only address the reverse ISC transition effectively at high repetition rates. Accordingly, in STED-mode no STED efficiency was observed at high repetition rates. However, fluorescence depletion is more pronounced when reaching low repetition rates (red colour in Fig.2.9) where the same photon density within the STED pulses reaches depleting levels of 60 %. Inherently, this observation is a consequence of the previous result. At high repetition rate the STED pulse can address both transitions, the depleting and the reverse ISC transition. Under this conditions the depleting effect is completely compromised by the fluorescence enhancement effect due to reverse ISC of the STED-beam. But with depopulating the dark state by stepping down the frequency, the depleting behaviour gains ground against the reverse ISC transition (inset (ii) in Fig.2.9). Therefore the STED depleting transition becomes the dominant process at low repetition rates.

The change of pulse duration of the STED pulse at least one order of magnitude has no significant influence on the STED efficiency or the reverse ISC (Fig.2.9 (c)), thus indicating that the addressed transitions are saturated and therefore eliminating any dependence on the pulse duration (like previously argued in section (2.2), Fig.2.5).
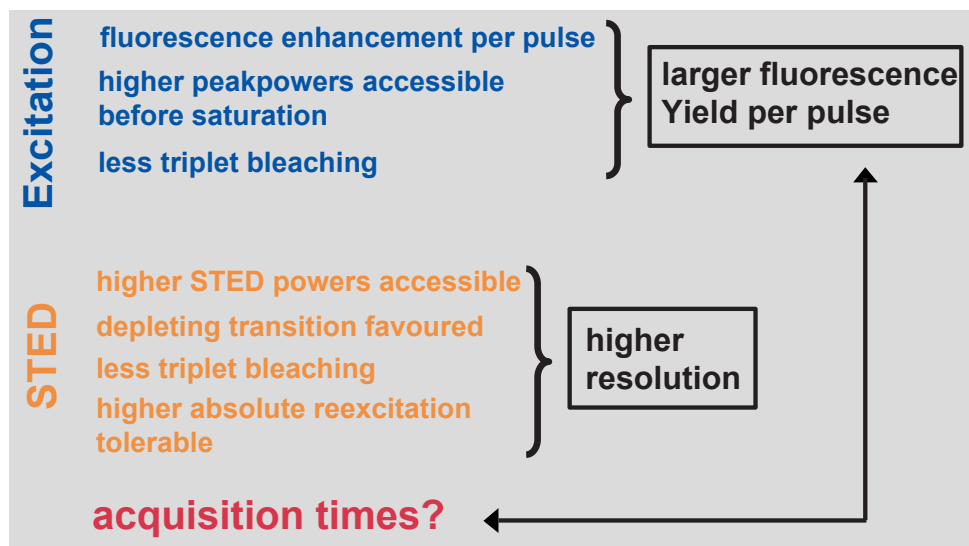
Figure 2.10: **Expectations for T-Rex STED-microscopy**

Conclusively, fluorescence dyes are generally expected to operate favourably under STED conditions in the low repetition rate regime. Exemplified on Atto465, a highly triplet pop-

ulating dye, the STED depleting transition is favoured under low repetition illumination against other compromising transitions, like the reverse ISC. In fact, Atto465 showed no STED applicability at 40 Mhz, whereas at repetition rates below 1 MHz the STED depleting ability was uncovered. On one hand, this observation illustrates that fluorescence depletion by STED is a general behaviour of a fluorescent dye, and on the other hand the application of low repetition rates widens the pool of fluorescent molecules accessible to STED-microscopy in terms of good depleting performance.

On the gained basis of understanding low repetition rate conditions for excitation and having tested them for STED applicability, the expectations for T-Rex STED-microscopy are summarized in Fig.2.10. Motivated by the uncovering of the T-Rex illumination scheme that substantially increases both the fluorescence yield per pulse and the photostability, the possibility of applying strong light levels prepares the grounds for expecting a resolution improvement of a STED-microscope with similar argumentation: applying larger STED peak intensities due to less dark state bleaching and more tolerable reexcitation due to the fluorescence increase following stronger excitation can directly enhance the resolution of a STED-microscope (see equation 3.1). Moreover, the fluorescence enhancement per pulse is the encouraging argument to fight the longer acquisition times being expected by drastically reducing the repetition rate, thus reducing the illumination time of the sample per second.
The next chapter will work out how these expectations were met in the experiment.

3 T-Rex STED-microscopy

3.1 Concept and experimental realization

Based on the following estimations, the operational principles of STED microscopy at a pulse repetition rate of 0.25 MHz that is 320 times lower than the standard rate of 80MHz were explored ([53]).

From the introduction we already know, that the rate for deexcitation by stimulated emission is given by $k_{STED} = \sigma I_{STED}$, with σ denoting the fluorophore cross-section and I_{STED} denoting the intensity of the deexcitation beam. Oversaturating the deexcitation requires k_{STED} be much larger than the fluorescence decay given by the inverse of the fluorescence lifetime, $\tau_{FL} \approx$ 1-5 ns, of the fluorescent state S_1. With typical molecular cross-sections $\sigma = 10^{-17}$ cm^2 for stimulated emission it follows that $I_{STED} >> 10^{26}$ photons/cm^2 which, at a wavelength of $\lambda = 600$ nm, amounts to $I_{STED} >> 33$ MW/cm^2. This intensity value is at least 10^3-fold lower than what is required for multiphoton excitation ([6]), but still 10^2-fold larger than what is used for single photon fluorescence excitation. Therefore, to operate with a moderate average power, the excitation and the STED beams are implemented in the pulsed mode ([19]). Besides, the duration of the STED pulse τ_{STED} is adjusted to a fraction of τ_{Fl}, typically ≈ 0.2 ns, in which case the depletion of the excited state is an exponential function of the stimulating intensity: $\exp(-\sigma\tau_{STED}I_{STED})$. Hence, a doughnut-shaped focal distribution featuring $I_{STED}^{max} = \max(I_{STED}(\vec{r}))$ at the doughnut crest and $I_{STED}(\vec{r}) = 0$ at the center, suppresses the signal throughout the focal region except at $\vec{r} = 0$. The remaining spot in the focal plane follows

$$\Delta r \approx \frac{\lambda}{2nsin\alpha\sqrt{1 + \sigma\tau_{STED}I_{STED}^{max}}}, \tag{3.1}$$

with nsinα denoting the numerical aperture at which the doughnut is generated ([54]). Thus, the resolution can be arbitrarily increased with increasing I_{STED}^{max} , in principle, down to the molecular scale ([19]).

An obvious challenge toward maximizing I_{STED}^{max} is elevated photobleaching of the fluorescent marker that usually scales nonlinearly with the applied intensities ([55]). For example, at the typical 80 MHz repetition rate of modelocked lasers, the focused average

power applicable to the green dye Atto 532 is about 15 mW ([56]). The associated I_{STED}^{max} = 250 MW/cm^2 yields a resolution of Δr = 50-70 nm. Larger I_{STED}^{max} and hence much narrower focal spots were reached only with a red dye under controlled photochemical conditions ([54]).

In STED microscopy, two bleaching pathways are imaginable ([31]): i) the absorption of the fluorescent state, leading to a higher molecular singlet state, $S_1 \longrightarrow S_{x>1}$, as it has been proposed for multiphoton microscopy ([44]) and ii) the excitation of excited molecules that have crossed to a triplet state, $T_1 \longrightarrow T_{x>1}$, or to another dark state with lifetime $\tau_T > 1\mu s$. Both the $S_{x>1}$ and $T_{x>1}$ are well known starting points for bleaching reactions (Fig.3.1(a)).
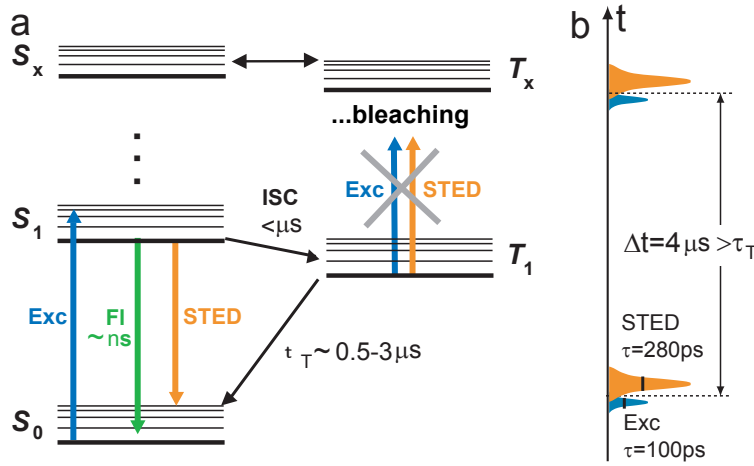

Figure 3.1: **(a) Fluorophore energy levels and potential bleaching pathways: fluorescence from S_1 is suppressed by stimulated emission. The latter may also excite the dye to a higher singlet state S_x, from which the molecule can cross to the triplet system T_x. In regions of weak STED pulse intensity, the molecule can directly cross to the T_1 featuring a lifetime of (0.5 - 3) μs. Excitation of T_1 molecules by subsequent pulses leads to reverse intersystem crossing or augmented photobleaching. (b) These adverse effects are counteracted by $\Delta t > \tau_T$.**

When considering the two routes, it becomes evident that the first one, $S_1 \longrightarrow S_{x>1}$, is counteracted by stimulated emission $S_1 \longrightarrow S_0$. With a wavelength optimized for the latter, $S_1 \longrightarrow S_{x>1}$ excitation by the STED pulse is less probable. Nevertheless, since the cross-sections for $S_1 \longrightarrow S_{x>1}$ are finite (both at the STED and at the excitation wavelength), higher singlet excitation is possible. The superexcited $S_{x>1}$ molecule may bleach, cross to the triplet system $S_{x>1} \longrightarrow T_{x>1} \longrightarrow T_1$, or return to S_1([45]). Referred to as internal conversion, the last process is very effective because it occurs within a few picoseconds. Due to the STED pulse duration of τ_T =0.2 ns, the putatively superexcited

molecule is instantly quenched by the same pulse. Therefore, as long as the molecule remains in the singlet system, the STED pulse is able to protect the molecule from photobleaching.

Just the opposite is the case once the molecule has slipped into the triplet state T_1. Due to its prolonged typical lifetime, $\tau_T \approx 1$ μs at ambient conditions, the T_1 molecule is exposed to a train of intense excitation and STED pulses. Given the comparatively large cross-sections (10^{-18} - 10^{-17} cm^2) for triplet absorption over a broad wavelength range, the STED pulse can efficiently pump up the molecule to higher triplet states $T_{x>1}$. The ≈ 80 MHz repetition rate of modelocked lasers used so far for STED implies that an inherently fragile triplet molecule faces on average 80 intense STED pulses before relaxing to the S_0 (just as previously discussed in chapter 2.2 for an excitation pulse only).
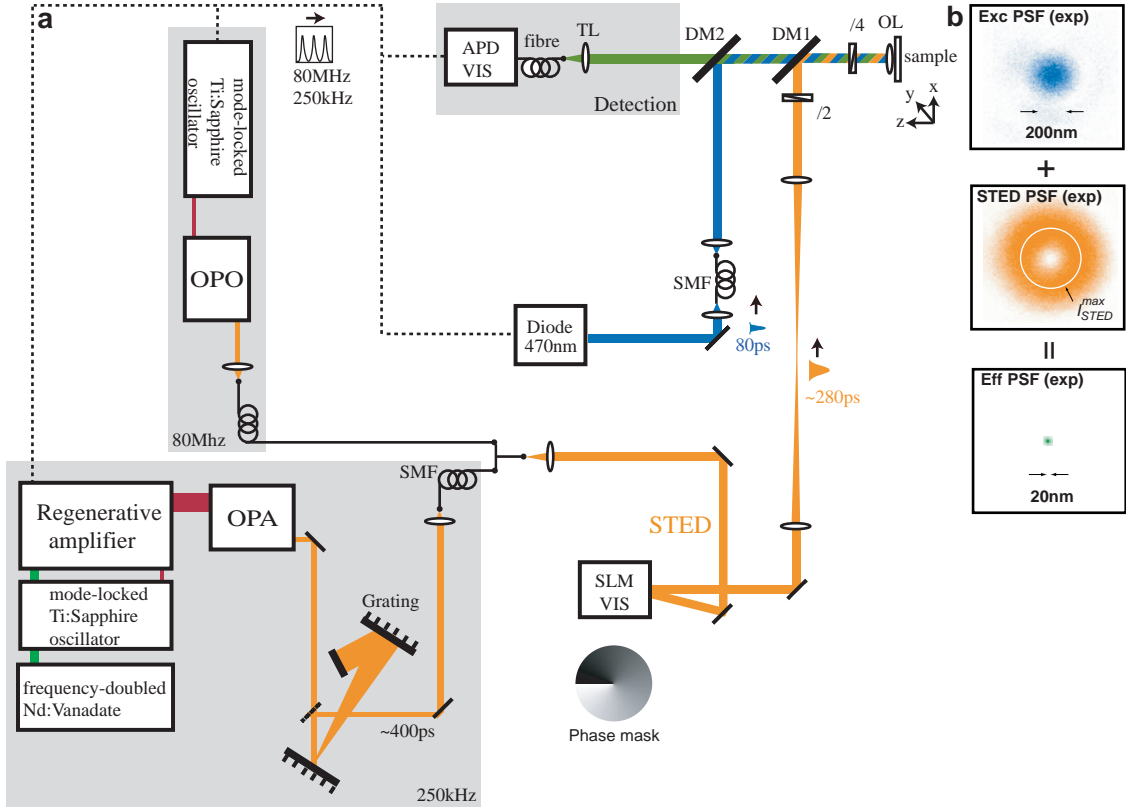
Figure 3.2: (a) T-Rex STED-microscope (250kHz) and 80Mhz STED setup. For explanation see text. (b) Stimulated emission depletion (STED) microscopy operation with interpulse time interval Δt $= 4$ μs. Measured focal spots (point-spread-functions) for excitation (wavelength: 470 nm, blue) and STED (603 nm, orange). Applying a crest intensity $\mathbf{I}_{STED}^{max}$ yields the effective spot shown in green (right). Note the fundamental reduction in focal spot area.

Moreover, most fluorophores spontaneously undergo $S_1 \longrightarrow T_1$ crossings with a probability of 1-10% per excitation cycle ([45]). At the doughnut hole, where the STED pulse is weak and the molecules relax spontaneously, stimulated emission does not override the intersystem crossing. Therefore, a remedy against this bleaching pathway is to illuminate molecules as little as possible within the timespan $\tau_T \approx 1$ μs after the excitation. The t $= 4$ μs time gap between subsequent pulse pairs ensures that a triplet state molecule of typical lifetime $\tau_T \approx 1$ μs relaxes to the ground state before encountering a second or third pulse pair (Fig.3.1(c)). This illumination scheme is termed Triplet-Relaxation (T-Rex) STED.

To explore the potential of T-Rex STED microscopy, an optical parametric amplifier fed by a regeneratively amplified modelocked Ti:Sapphire oscillator ([53]) (Coherent, Santa Clara, CA) was employed providing visible pulses of ≈ 200 fs duration and 100-250 nJ pulse energy (Fig.3.2 (a)). To stretch them to ≈ 280 ps, the pulses were diffracted from a grating pair before being coupled into a 4-m single mode glass fiber. The STED beam was circularly polarized and converted into a doughnut by a spatial phase modulator (Hamamatsu, Hamamatsu City, Japan). The latter was programmed to imprint a helical phase ramp on the STED beam wavefront which is reminiscent of a Gauss-Laguerre beam providing circular symmetry in the focal plane ([57]). For excitation, a laser diode emitting ≈ 80 ps pulses at 470 nm (Picoquant, Berlin, Germany) was synchronized. Both beams were focused by a 1.4 numerical aperture oil immersion lens (Leica Microsystems, Mannheim, Germany) on the sample. Fig.3.2 (b) shows the spot of the blue excitation light along with its STED counterpart; both spots are measured data.

For comparison measurements (Fig.3.4) an 80Mhz setup features a Ti:Sapphire laser pumping an optic parametric oscillator (OPO) for providing the STED pulse train.

3.2 Focal plane resolution of 20 nm in fluorescence microscopy

The resolution attainable under T-Rex conditions was first demonstrated on yellow-green beads emitting in the 500-530 nm range (Fig.3.3). Specified by the manufacturer using electron microscopy, the beads varied by 4 nm around a mean diameter of 24 nm (Molecular Probes Eugene, OR). The imaging parameters were: 10 x 10 nm pixels, 603 nm STED wavelength and $I_{STED}^{max} = 4.7$ GW/cm^2. Whereas the confocal recording (Fig.3.3 (a,e)) yielded undefined blobs, the STED images (b,f) discerned virtually every bead in the focal plane.

Fig.3.3 (g) and (h) depict line profiles through beads located 39 nm and 42 nm apart, respectively; both are clearly separated. The STED images also indicate that a frac-
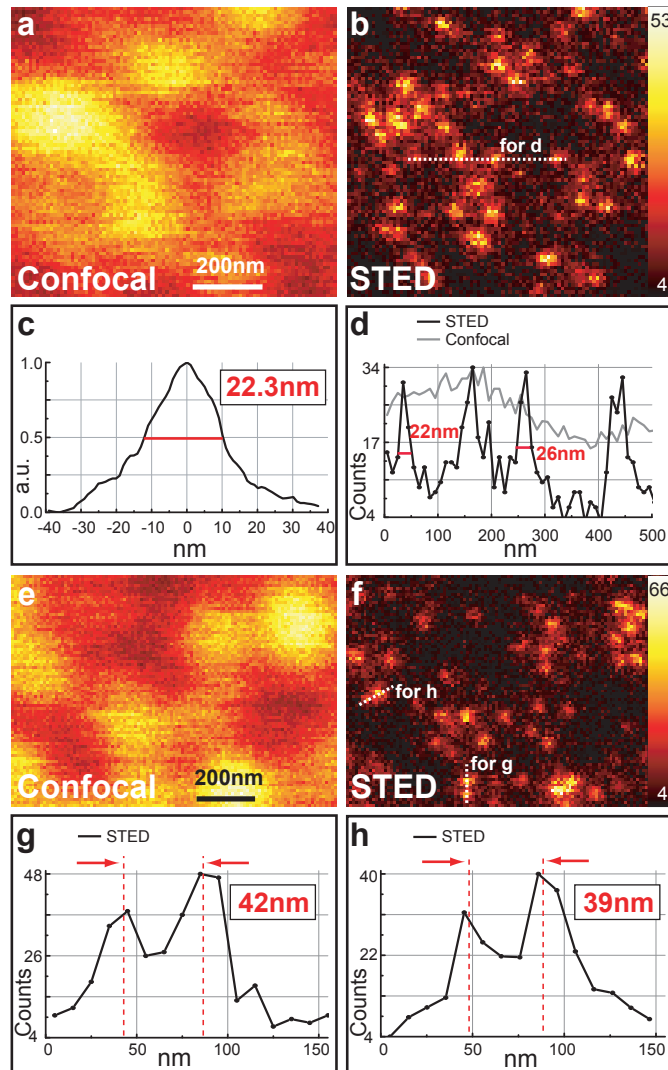
Figure 3.3: (a) Resolution < 20 nm in the focal plane of a STED microscope. Whereas the confocal imaging mode (a, e) fails to resolve the bead agglomeration, the corresponding STED recording (b and f) discerns every 24 nm bead. (c) Averaged profile of bead images. The **22.3 nm** FWHM indicates a lateral resolution of ≈ 16 nm in the focal plane (after extraction of the bead size). (d) Data as indicated by the dashed line in panel (b), both for the confocal and the STED recording. Note the sharp peaks resulting from STED superresolution. (g,h) Intensity profiles through the data in (f) proving the separation capability of the STED microscope.

tion of the fluorophore molecules leaked into the mounting medium (Mowiol by Merck, Darmstadt, Germany) which is commonly observed for nanosized fluorescent beads. The structure of the fluorophore and its molecular bleaching kinetics remained unknown to

me, but at 80 MHz resolving the beads was precluded by photobleaching.

Furthermore the function describing the bead image by averaging over 75 beads that were comparatively isolated and of lesser brightness was determined. The result is displayed in Fig.3.3 (c), exhibiting a full-width-half-maximum (FWHM) of 22.3±2 nm, as well as in the lower panel of Fig.3.2. As it is given by the convolution of the bead object function with the PSF of the microscope, the bead image function in Fig.3.3 (c) is just an upper bound for the actual PSF. Therefore, the actual resolution of the STED microscope is below 20 nm. If the PSF and the bead function are coarsely approximated by a Gaussian, one can assess the actual focal plane resolution as $=$ 15.8±4 nm. Comparison of this value with the resolution limit given by Abbe's criterion in an epifluorescence microscope, $\lambda_{FL}/2nsin\alpha = 190$ nm, demonstrates a ≈ 12 fold gain in focal plane resolution.

Reducing the repetition rate by a factor of 320 as compared to the standard 80 MHz implementation initially appears unappealing, because of the concomitantly reduced illumination duty cycle. However, experiments comparing the two illumination schemes showed that for the Rhodamine-like dye Atto532 (AttoTec, Siegen, Germany), as well as for many other dyes, this factor is largely compensated by the total yield of fluorescence. For example, in the 80 MHz case, the maximum applicable average power on an Atto532-labeled sample was 2 μW for excitation and 15 mW for STED, with corresponding focal intensities of 0.43 MW/cm^2 and $I_{STED}^{max} = 250$ MW/cm^2, respectively. In the 0.25 MHz case, I employed 0.1 μW for illumination and 0.5 mW for STED, but the lower repetition rate gave rise to a much larger peak power: 7 MW/cm^2 for excitation and $I_{STED}^{max} = 2.2$ GW/cm^2. In terms of pulse energy, the individual STED pulse reached a maximum value of 15mW/80MHz=0.1875 nJ in the 80-MHZ case and 0.5mW/0.25 MHz=2 nJ under T-Rex conditions.

Thus, the T-Rex conditions not only allowed to utilize STED pulses which were 9 times more intense, but also to excite the molecules 16 times more efficiently per pulse. In fact, calculations show that 17 % of all molecules in the inner focal spot were excited to S$_1$ by each pulse. Strong excitation not only favoured a strong fluorescence signal but also effectively prepared the grounds for STED by better emptying the S$_0$ and enhancing the S$_1$ population. Comparison of the total fluorescence yield showed that in the T-Rex (0.25 MHz) case, the integral signal before molecular bleaching was ≈ 30 times larger than in the 80 MHz counterpart optimized for maximal resolution. Therefore the extension in recording time was only 5- to 10-fold compared with the 80 Mhz-case. Because of the stronger signal, the typical dwell time in the images was 3-8 ms per pixels. Fig.3.4 shows the direct performance comparison on the same yellow-green bead sample between the 80Mhz-setup, optimized in terms of peak power, as well as the 250 kHz-setup, optimized respectively. Obviously, bleaching concearning mainly the STED-bleaching through dark state (triplet) absorption, is in the second STED image at 250 kHz (Fig.3.4 (g)) nearly
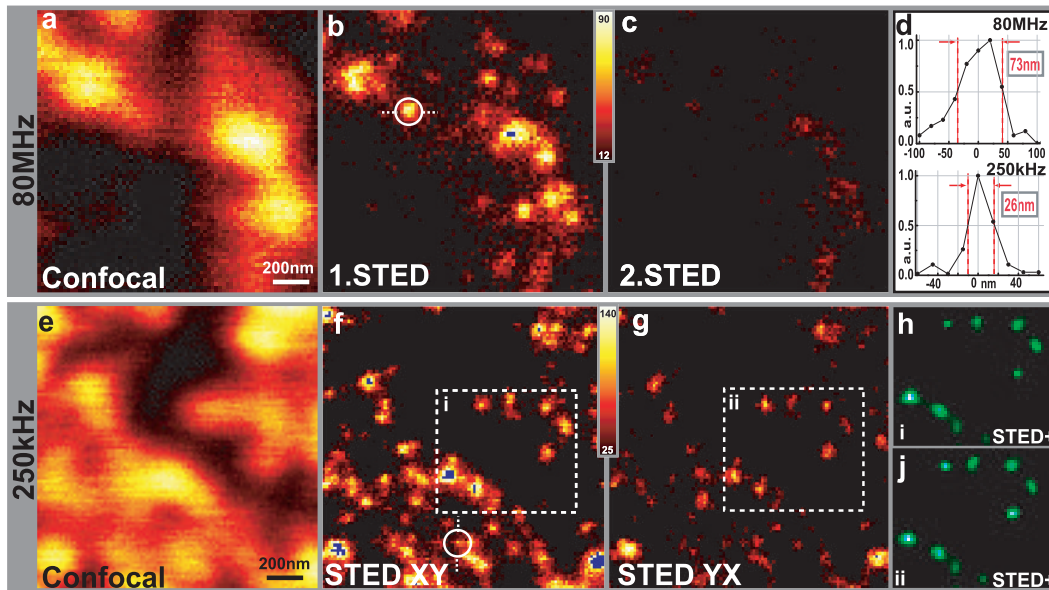
Figure 3.4: **Comparison of an 80 Mhz- and 250 kHz- STED setup. (Upper row) Recordings at 80 Mhz, with (b) and (c) showing two consecutively taken STED images; (Lower row) respectively taken images at 250 kHz with additionally changing the fast axis from (f) to (g). Note the bleaching reduction from the comparison of (c) with (g). (d) Profiles of 2 beads taken under both imaging conditions, respectively; note the 3-fold increase in resolution at low-repetition rate condition (250 kHz). (h,j) Magnified subregion after RL-deconvolution. Both images recall every single bead at its position thus demonstrating the reliability of the STED method.**

supressed when comparing it to the according second STED recording at 80 MHz (Fig.3.4 (c)), although the STED peakpower at 250kHz is nearly an order of magnitude larger. Moreover, the resolution increase at low repetition rate conditions is vividly demonstrated in (d), showing the same beads resolved in approximately 3-fold increased resolution. Finally note, that both consecutively taken, but independent STED images of the same bead distribution (outtakes in (f,g)) recover every single bead at its very position thus demonstrating the reliability of the STED method itself.

3.3 Biological applications of T-Rex STED-microsopy

After proving the new resolving power of the T-REX STED-microscope, the next step is to launch it for biological relevant problems. To this end the structures of interest were labeled by immunostaining methods ([58]) using Atto532 as organic fluorescent marker,

having shown its applicability under T-REX conditions in chapter 2 and STED compatibility in previous applications ([56],[59]). A highly visible advantage of STED microscopy is that in general any staining protocol can be performed as usual for confocal microscopy. As a control, all images in the following were recorded in the STED and confocal mode line by line by turning on and off the STED laser beam.

3.3.1 Biological structures accessible with STED

Initially one must deal with the justified question in which parts, organelles and structures of cells STED-microscopy can be successfully applied, since the generation of the STED beam requires e.g. sophisticated PSF engineering, which could be influenced by variations in the refractive index in different types of tissue. This question will simultaneously break the ground for the general applicability for the STED method in cell biology. During the various biological projects I came across many different parts of a cell, including the nucleus, mitochondria, the cytoskelett or proteins embedded in the plasma membrane. Fig.3.5 gives an overview of the cell structures that could be images with STED microscopy providing a resolution ability in the focal plane of ≈ 20 nm. Shown are the confocal and according STED images (linear deconvolved where indicated) throughout different parts of a cell, demonstrating how STED-microscopy can open up new insights into cell biology by providing macromolecular scale resolution ability.

(a) Assembly of SNAP25, a SNARE protein which is involved in synaptic vesicle fusion on the plasma membrane of mammalian cells ([60]). The substructure of the highly clustering protein pattern of SNAP25 can only be revealed by high resolution STED-microscopy ([61]). Another example shows the true size dimensions of vesicles from the same mammalian cells, which can be seen in the T-Rex STED image in (b) performed on the vesicle protein Synaptobrevin 2. Here the vesicles were previously been extracted from the cell during the purification process (for details see [62]). The arrow is indicating a FWHM of 36 nm, which is consistent with size evaluation from EM imaging ([63]). In (c) the tubulin structure from the cytoscelett of a cell is shown in both imaging modes. The STED image clearly resolves the bundles of tubulin fibres.

The ADP/ATP carrier, also referred to as ANT (adenosin nucleotide transporter), is the most abundantly occurring transporter of the inner mitochondrial membrane and is responsible for the membrane potential-driven exchange of ATP versus ADP between the inner-membrane space and the cytosol ([64]). The function and the electrogenicy of the protein have been investigated in detail, but its localization in the inner membrane remains unclear. The confocal recording of ANT in mammalian cells in (d) does not indicate a nonuniform distribution of the protein, whereas only the STED recording can uncover the clustering behaviour of ANT in the inner membrane of the mitochondria.
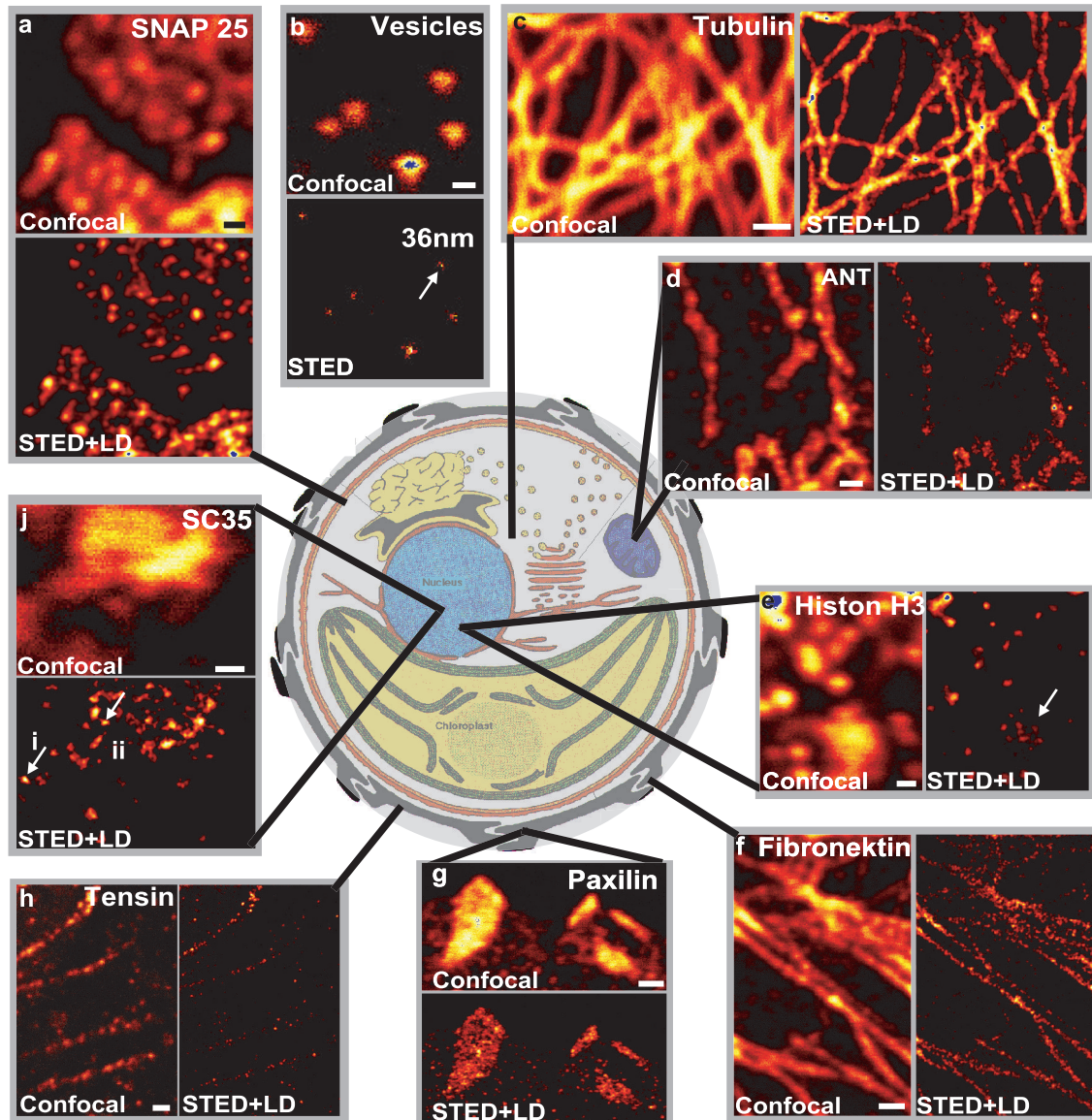
Figure 3.5: **STED-microscopy performed in conventional confocal and STED mode (deconvolution applied where indicated) in various compartments and organelles of a cell. Scale bar 200 nm (a,b,e,i) and 500 nm (c,d,f,g,h). For explanation see text.**

Turning into the nucleus Fig.3.5 (e) represents recordings of H3K9me3, a specific post-translational modification of the Histone H3 that has been associated with heterochromatin in the cell nucleus. Heterochromatin is the transcriptionally silent region of the genome, that is more densely packed than the active regions ([65]). Note that the STED image clearly resolves the arrow indicated area into defined and separated spots, whereas the confocal fails to do so.

Diverse cellular processes are carried out by specific integrin-mediated adhesions. Cell spreading and migration are driven e.g. by focal complexes, whereas robust adhesion to the extracellular environment are dominated by focal adhesions ([66]). The mechanism(s) governing those distributions in time and space as well as the interaction between different types of adhesions are unknown. Here it is shown that STED-microscopy is able to address the nanopatterned structure of different focal adhesion proteins of PAEC (porcine aortic endothelial cells) cells[1]. Fibronektin (f), Paxilin (g) and Tensin (h), the focal adhesion proteins which were studied, show clustering behaviour in the STED recordings, which cannot be recovered by conventional imaging. Especially in the case of Fibronektin, showing similar appearance in the confocal image like tubulin (comparing the confocal images of (f) with (c)), the STED image decodes once again a strict and regular clustering behaviour of the protein. Also Paxilin shows at the focal adhesion areas a clustered substructure of distinct adhesion "hotspots". This result of uncovering nanostructure within individual adhesion spots is also addressed by a different approach of studying the coherences behind the molecular arrangement of integrins in cell adhesion where experiments with living cells are carried out on nanostructured surfaces ([67]).

Finally (j) reveals the superresolving power of a highly compartmentalized structure of mammalian interphase nuclei. Particularly interested were the nuclear "speckles" enriched in premessenger RNA splicing factors and polyadenylated RNA ([68],[69],[70]). I imaged the distribution of the speckle marker protein, SC35. In contrast to the confocal imaging, the resolving power of the STED-microscope allowed to separate the speckles into distinct particles that have so far been accessible by electron microscopy only ([71]). Indicated areas feature FWHM profiles of 25 nm (i) and 22 nm (ii) in the raw STED data (not shown), respectively, thus proving the 20 nm resolution obtained in the nucleus of a fixed but otherwise intact mammalian cell. Notably the effective PSF of the STED-microscope, featuring no z-resolution enhancement in this realization, is also able to visualize details down to the nanoscale in real 3D structures. T-REX STED-microscopy appears to be suitable to bring further critical insight into how the nuclear organization ensures regulated gene expression.

Having shown that various biological fields regarding various parts of cells are feasible of exploiting the enhanced information of high resolution STED-microscopy, the next chapter illustrates concrete biological results of the latter method in further highlighted examples of the successful application of T-Rex STED-microscopy in cell biology.

---

[1]In kindly collaboration with Tova Volberg and Benjamin Geiger, Department of Molecular Cell Biology, Weizmann Institute of Science, Rehovot 76100, Isreal

3.3.2 Anatomie of a fusion protein Syntaxin 1 forming membrane microdomains

The fluid model for the structure of biological membranes ([72]) proposes single proteins to diffuse freely in a sea of lipids. However, in the plasma membrane of eucaryotic cells many proteins are concentrated in sub-micron sized clusters whose architecture and dynamics are still enigmatic. In fact, organization into clusters is well established for an increasing variety of membrane proteins ([73]). However, these domains are too small to be characterized by conventional light microscopy. To overcome this limit nanoresolution STED microscopy was combined in a more comprehensive study with quantitative biochemistry and FRAP-analysis ([74]) to explore the mechanism of the cluster formation in more detail. For this study Syntaxin 1 was used as an example because it is a relatively simple membrane protein being involved in the SNARE interactions of vesicle fusion. Recently it was already shown, that the SNARE motif of Syntaxin 1 is involved in cluster formation ([75]). Fig 3.6 displays a representative image of syntaxin distribution in both imaging modes, confocal (a) and STED (b), both subject to a RL-deconvolution respectively, on a membrane sheet of a PC12 cell. Indeed, the STED image can display
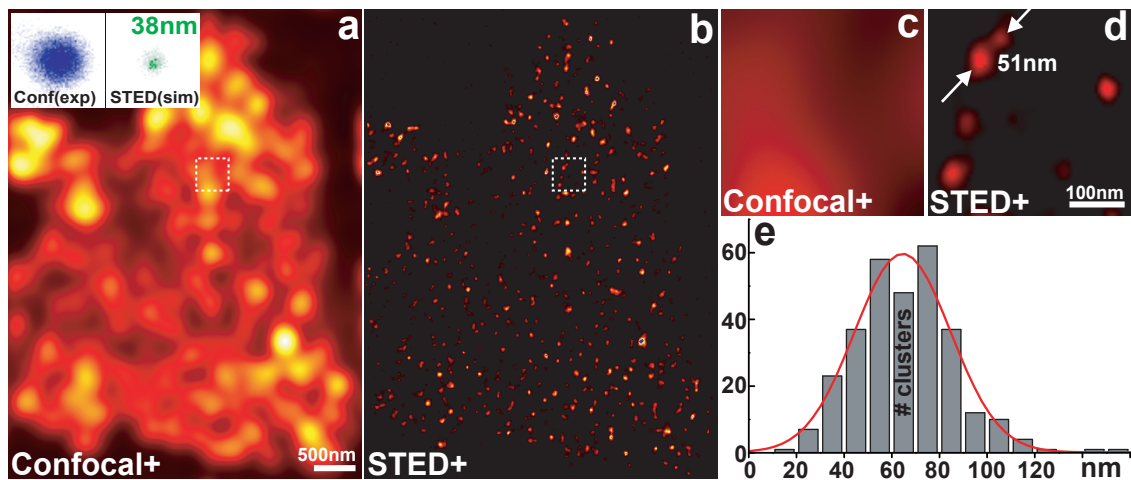
Figure 3.6: T-REX STED performed on Syntaxin I membrane sheets. (Inset in a) Effective PSF's for the confocal (190nm) and STED recording (38 nm); the latter is simulated with the measured depleting curve and both measured PSFs. RL-deconvolved confocal (a) and STED (b) recording of a typical membrane sheet. (c,d) Magnified outtake with clearly resolving two individual Syntaxin clusters distanced with 51 nm in the STED image. (e) Histogram of the clustersize from 304 individual clusters from 8 different patches in the raw STED data.

the single Syntaxin clusters separated and als give an upper limit of the clustersize by

identifying the FWHM of 304 individual clusters on eight different membrane sheets (e). With respect to the size of the effective STED-PSF (38 nm) at the given STED power level used for imaging (inset (a)), determined by the light distribution of both PSF's (excitation and STED-doughnut) and the according depleting curve, the upper limit in clustersize is ≈ 64 nm, suggesting dense packing of clustered syntaxin molecules. This size has especially to be taken serious, as the imaging PSF is crucially below the determined size thus being able to resolve smaller structures. The magnified outtakes shown in (c) and (d), respectively, demonstrate from the resolution point of view, that only the STED image contains object information on this spatial scale with clearly separating two individual Syntaxin clusters by 51 nm.

The clustersize is an important input parameter only being accessible by STED microscopy in the comprehensive modeling of the anatomy of supermolecular membrane protein structures like the Syntaxin 1 clusters thus affirming STED-microscopy to be an important tool in the microdomain research ([75]).

3.3.3 Signal transduction for biologically relevant odors involves the protein TRPM5

Some olfactory sensory neurons (OSNs) in the main olfactory epithelium (MOE), a specialized epithelium tissue inside the nasal cavity, respond to pheromones, but transduction for these stimuli in the MOE is poorly understood ([76]). A key step in transmission of olfactory information is the activation of the canonial cAMP (adenosine 3',5' cyclic monophosphate) signaling pathway by binding of airborne odor to olfactory receptors, resulting in influx of calcium through a CNG (cyclic nucleotide-gated) channel and subsequent depolarization ([77]). Biologically relevant chemosignals including pheromones signal social, sexual, genetic makeup and species identity are important for the survival of the individual and the species. Traditionally, it was thought that the vomeronasal organ, a tubular structure located in the roof of the mouth that is associated with the accessory olfactory system, mediates detection of pheromones - chemicals given off by an animal that elicit a response, physiological and/or behavioral, in a conspecific ([78]). However, a growing number of studies show that the main olfactory system also responds to pheromones ([79]). Although it is now clear that the main olfactory system is involved in detection of biologically relevant chemosignals, the transduction pathway(s) stimulated by these chemical stimuli in OSNs is (are) not well understood.
A comprehensive study of TRPM5, the protein M5 from the transient receptor potential channel in OSNs, strongly implicated the participation in chemosensory transduction, not only in the taste system as previously reported ([80]), but latterly also in the olfactory system ([81]). Within the process of this investigation STED microscopy was performed

on immunofluorescence staining of the olfactory epithelium with a TRPM5 antibody (Fig. 3.7).
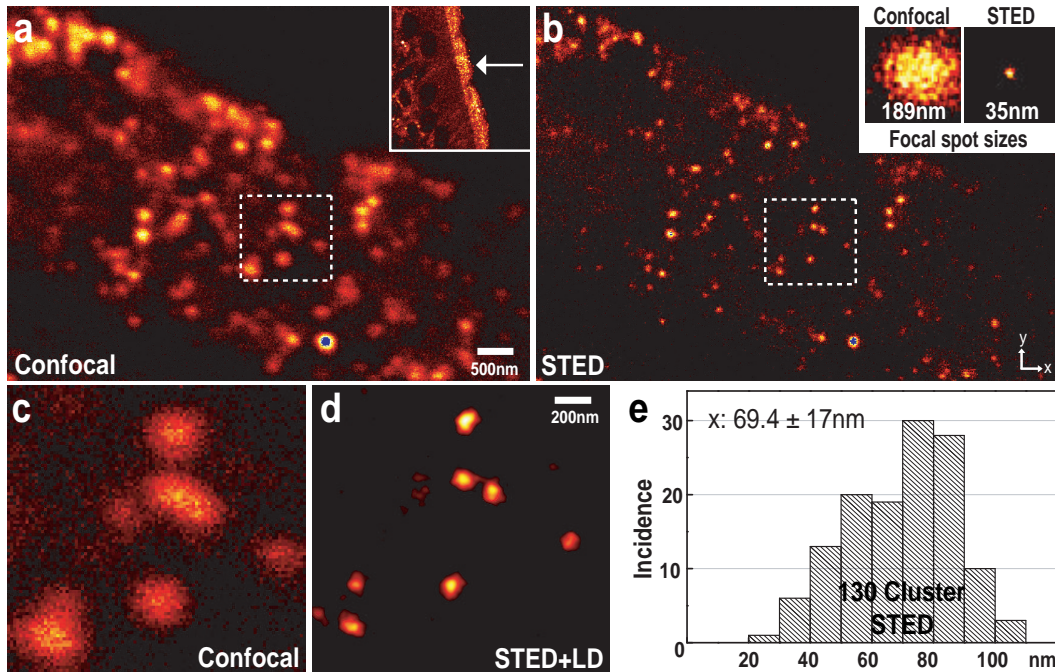
Figure 3.7: **Analysis of spot size for T-Rex STED images of TRPM5 immunoreactivity in the cilia layer. Confocal (a) and STED (b) images of TRPM5 immunofluorescence in the cilia layer of the olfactory epithelium. Inset in a: Confocal image at a lower magnification taken with a conventional confocal microscope. Inset in b: Smallest spot (antibody cluster) sizes in the confocal (189 nm) and STED (35 nm) imaging modes (each is an average of 3 individual spots). c and d: Higher magnification images of the areas enclosed by the dashed boxes in a and b respectively. The image in d represents the STED image further processed using a linear deconvolution (LD). (e) Histogram showing the distribution of full width half maxima (FWHM) for the clusters in three separate images (130 individual clusters from three separate images). In order to estimate the FWHM background was subtracted from the STED images and each cluster was fit with Lorentz-shaped profiles. If one assumes a 35 nm effective STED-PSF (indicated by the minimal spot sizes in the images) the real mean object size of the clusters is in the order of ≈ 60 nm.**

The images (a) and (b) show the TRPM5 distribution in the apical layer of the olfactory epithelium in confocal and STED mode, while the inlay in (a) illustrates the confocal cross-section of the olfactory epithelium indicating the site of recording. Higher magnification outtakes are shown in (c) and (d), with the STED image revealing discrete spots with an

average size of 69 nm derived from the raw data (e). I found similar punctuate distribution for CNGA2 (not shown), consistent with previous electron microscopy studies ([82]). A further intriguing finding of this study is the co-expression of TRPM5 and CNGA2 in the majority of TRPM5-expressing OSNs investigated by conventional fluorescence microscopy ([81]). Could these two channels, the CNGA2 channel and the TRPM5 channel, interact directly? TRPM5 has been shown to be a Ca^{2+}-activated channel ([83]), while under physiological conditions the current flowing through the CNGA2 channel is also made up mostly of Ca^{2+}. In fact, the finding that immunoreactivity for TRPM5 is found in small spots with average diameter of 69 nm suggests that the TRPM5-channel may be clustered in small microdomains. If CNGA2 and TRPM5 were co-localized within these microdomains there would be efficient activation of the TRPM5 channel by Ca^{2+} flowing through the CNGA2 channel. This information is likely to be accessible in the future of high resolution microscopy experiments, leading to further insights in the mechanism of signal transduction in the olfactory system.

3.3.4 Flow-induced functional adaptation and differentiation of endothelial cell junction

Endothelial cells line the inner surface of all blood vessels and the heart, and constitute a diffusion barrier between the blood and tissue, which is required for a controlled exchange of water, solutes and migrating cells between the blood and the surrounding tissue. A transport through the endothelium can occur either transcellular by vesicular machanisms or transport molecules in the cell membrane, or paracellular through the intercellular space. The paracellular transport is controlled by different cell junctions, particularly the adherens junctions and the tight junctions. While the tight junctions are well expressed in the endothelial cells of the blood brain barrier, they are poorly developed or even absent in most other endothelial cells. In these cells the paracellular barrier is mainly controlled by adherens junctions. The cell to cell adhesion in these junctions is mediated by the vascular endothelial cadherin (VE-cadherin) ([84]), which is an endothelial cell-specific adhesion protein. The extracellular domain of this transmembrane protein directly connects adjacent cells to each other while the intracellular domain is linked to actin filaments, composed of the protein actin, which is a prominent compound of the cytoscelett ([85]).

Due to their localization, endothelial cells are constantly subjected to shear stress generated by the flowing blood. This mechanical stimulus plays a pivotal role in vascular endothelial structure and function. Endothelial cells of the veins are polygonal in shape, while endothelial cells of the arteries are spindle shaped and aligned in the direction of flow ([86]). Transposition of vein segments into the arterial circulatory system or application
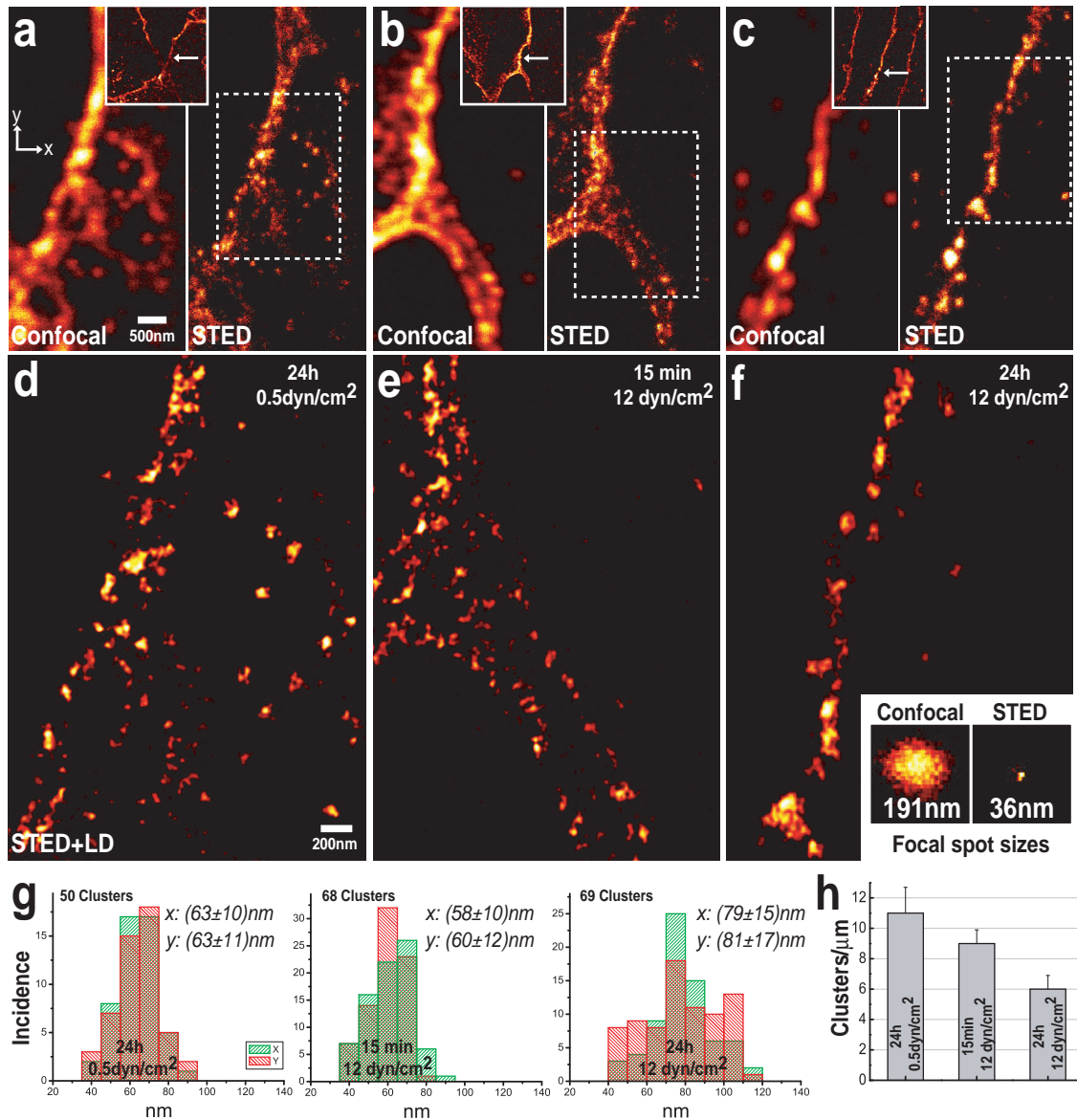
Figure 3.8: **Imaging reorganization of VE-cadherin of endothelial cell junctions under stress with nanoscale resolution STED-microscopy. (a,b,c, inset) Low-magnification confocal image indicating site of recording. Contrary to the confocal images (a,b,c, left), the STED recordings (a,b,c, right) display clustering behaviour of VE-cadherin with details < 40 nm. Panel (a) shows cells after exposure to low flow (0.5 dyn/cm^2), (b) after 15 minutes and (c) after 24 hours high shear stress exposure (12 dyn/cm^2). For direct comparison equally sized subregions of the STED images are further highlighted with linear deconvolution (LD) (see Appendix A.2) (d,e,f). Note the linearization of the cell contact protein distribution from d to f. Size distribution of the VE-cadherin clusters in orthogonal directions (g) and its line density (density of clusters along the cell junctions) under different stress situations as indicated (h). (Inset f) Upper limit for the effective focal spots of confocal and STED microscopy (average of 3 individual clusters within the images) determine the resolution of the respective imaging modes under the applied power conditions for STED.**

of flow to endothelial cell cultures causes cell elongation and alignment as observed in arteries in vivo ([87]). Those data identified fluid flow as a critical and physiological stimulus in arterialisation and differentiation of the endothelium. Since flow-induced morphological transition follows a characteristic time course of cell orientation, cell elongation and alignment in association with cell migration ([88]) a spatially and temporally remodeling of inter-endothelial junctions is required but the functional and structural consequences remains to be investigated. In the present study the functional and structural adaptation of endothelial junctions and barrier function in response to acute and chronic flow is shown ([89]).

Results and discussion

Laminar flow causes endothelial cell elongation and alignment that requires a coordinated regulation of endothelial cell junctions and was investigated on human umbilical vein endothelial cell cultures. Laminar flow was applied to endothelial cells using an extended cone-and-plate rheological system ([90]). Since VE-cadherin/catenin complexes and actin filaments are critical in junction regulation, immunofluorescence staining was performed (staining protocols see A.5). Under static and low flow conditions (0.5 dyn/cm^2) VE-cadherin was mainly localised in large overlapping endothelial junctions and exhibited an irregular pattern of staining. At arterial levels of flow (12 dyn/cm^2) immunofluorescence staining of VE-cadherin revealed a linearization of VE-cadherin, which describes the reorganization of VE-cadherin closer to the cell to cell contacts. Simultaneously one can verify reduced overlapping cell junctions and recruitment of junction-associated linear actin filaments ([89]). However, confocal images of the VE-cadherin distribution could not address the question of whether the VE-cadherin is altering its density at the cell contacts when applying flow profiles. Fig.3.8 presents the STED-microscopy study on VE-cadherin staining for different stress situations on endothelial cells. In contrast to the confocal images, the STED images of VE-cadherin of cells subjected to low flow (0.5 dyn/cm^2, 24 h) allowed the identification of clustering of proteins at the cell border (a). The profiles from 50 individual clusters were measured in the raw STED-images, providing round shaped clusters of 63±11 nm in diameter (first histogram in g). Furthermore, the clusters appear to be randomly distributed at cell junctions. Consistent with the observed transendothelial electrical resistance (TER)-increase (for details see [89]) and the reorganisation of junctional proteins and f-actin, STED microscopy revealed a largely linear distribution of VE-cadherin after 15 minutes of shear stress exposure due to extended lateral clustering (b). The cluster size remains basically unchanged with a diameter around 60±11 nm at this time point (middle histogram in g).
In addition to the short flow exposure experiments, the STED images after 24 hours of high flow uncover a further linearization of the cell junctions (c), featuring single chains of VE-cadherin clusters at the cell-to-cell junction. Consistent with this observation the

cluster sizes are significantly increased to 80±15 nm in diameter, indicating an aggregation of protein clusters at the elongated cell junction after 24 hours of high flow exposure. In fact, further evidence of this long-term reorganization effect is given by the number of clusters per chain length, which are considerably reduced form 12 clusters per μm under low shear stress conditions to 6 clusters per μm for cells exposed to high shear stress for 24 hours (Fig.3.8 (h)). Thus shear stress induced reorganization of VE-cadherin consists of a short-term linear reorganization of the VE-cadherin clusters, while the long-term exposure additionally induces cluster aggregation at the cell contacts. Together with the observed recruitment of filamentous actin to the junctions this pattern appears to be consistent with the distribution of these proteins in vivo ([91]).

The presented study investigated the structural adaptation of endothelial cell junctions in response to acute and chronic flow. Although VE-cadherin usually shows a diffuse staining along the cell border, the clustered organization of this protein can not be resolved using conventional fluorescence microscopy. Using the potential of high resolution STED microscopy, it became possible to show, that VE-cadherin forms cluster in the range of 60-80 nm. Application of shear stress increased the size of VE-cadherin clusters, which is consistent with flow-induced linearization of VE-cadherin along the junctions in association with recruited actin that remained at the junctions even during long lasting cell alignment. Both appears to be responsible for the early and long-term physiological adaptation of endothelial barrier function. The data further support the concept that shear stress is largely responsible for arterial differentiation of endothelial cells.

3.3.5 Imaging nanopatterns of endosomal proteins

Containing a variety of synaptic proteins, the endosomes of PC12 cells have been used extensively in *in vitro* assays for studying neuroendocrine activity. In gerneral those endosomes form structures of around 200-400 nm, occasionally even larger. Particularly they have been found to generate synaptic vesicles ([92]), thus being a key player in the mech-
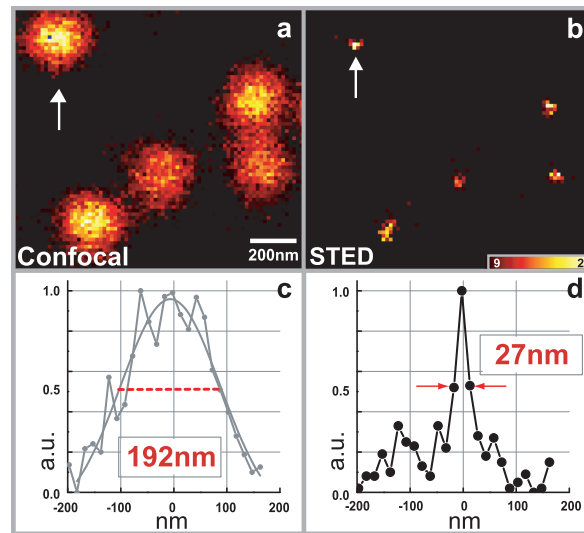
Figure 3.9: **Synaptotagmin I molecules form distinct spots on endomsomes. Whereas confocal microscopy exhibits a 190-200 nm diffraction limited spot per endosome (a), STED microscopy recognizes sharp dots of 25-40 nm size (b), both indicating its resolution as well as the punctuated spatial arrangement of synaptotagmin I on the endosome. (c, d) Corresponding intensity profiles.**

anism of neuronal signal transduction. So far, the resolution limit prevented to disclose any substructure on endosomes using fluorescence microscopy. Fig.3.9 compares recordings of synaptotagmin I, a transmembrane synaptic vesicle protein, on purified endosomes of the PC12 cell line ([92]). Whereas the confocal image (a) displays diffraction limited blobs of 192 nm FWHM (c), the corresponding STED image ($I_{STED}^{max} = 1.6$ GW/cm^2) identifies protein patches in the range of 25-40 nm. Fig.3.9 (d) shows an intensity profile through the protein labeled endosome, featuring a FWHM of 27 nm. Since the extent of the molecular distribution of synaptotagmin I on the endosome plus the antibody label is at least 15 nm, one can conclude that the actual lateral resolution of the system is 20 nm. In the process of vesicle formation one hypothesis being discusses is that endosomes putatively form protein subdomains specifically containing just synaptic vesicle proteins, such as synaptophysin. These subdomains subsequently break off. So far, this hypothesis was difficult to put to the test, since endosomes are too small for conventional light mi-
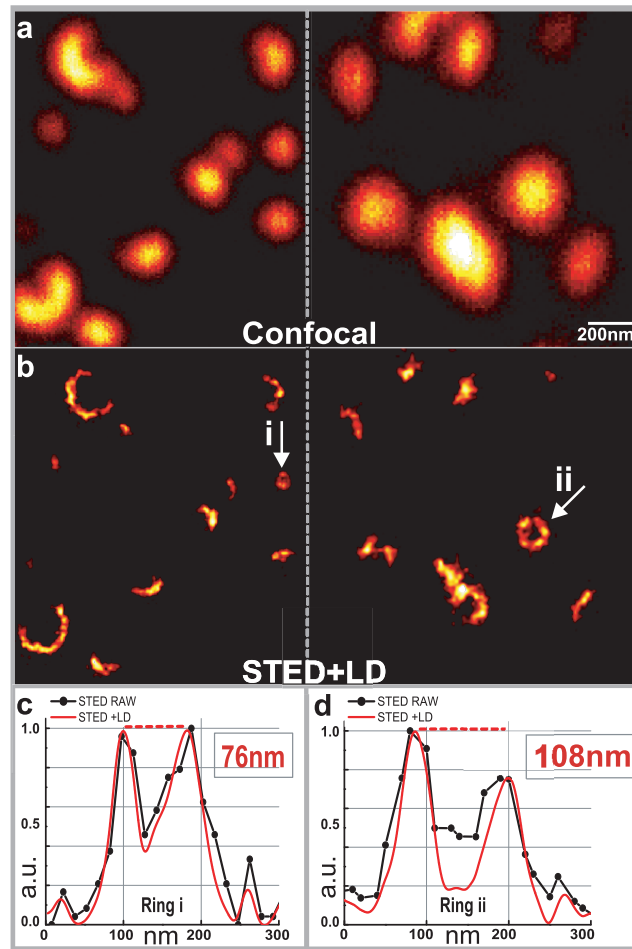
Figure 3.10: Synaptophysin forms elaborate nanopatterns on endosomes. (a) confocal reference, (b) STED microscopy plus a linear deconvolution (LD) revealing ring-like and C-shaped nanoarrangements. (c,d) Line profiles through rings, both of the LD (red line) and the raw STED data (black, with pixels).

croscopy, and the substructures cannot be easily recognized by electron microscopy due to the lower efficiency of labeling with metal particles.

Fig.3.10 shows that STED microscopy displays synaptophysin patterns on endosomes, such as nanosized C-shapes and rings ([53]). Note that the confocal recordings of synaptotagmin I (Fig.3.9) and synaptophysin are similar, although the latter protein seems to exists in typically larger numbers on individual endosomes and presents itself partly in noncircular shapes (confocal recording in Fig.3.10 a). But there is no indication that both proteins provide such different nanopatterns looking on the nanoscale. In the fourth chapter of this work (4.3.2) these endosomal proteins are again subject of investigation with a Dual-colour T-Rex STED-microscope.

3.3.6 Imaging neurofilaments of the human brain

Fig.3.11 displays the protein heavy subunit of neurofilaments (NF-H) in the human neuroblastoma cell line SH-SY5Y (retinoic acid-BDNF-differentiated) which establishes
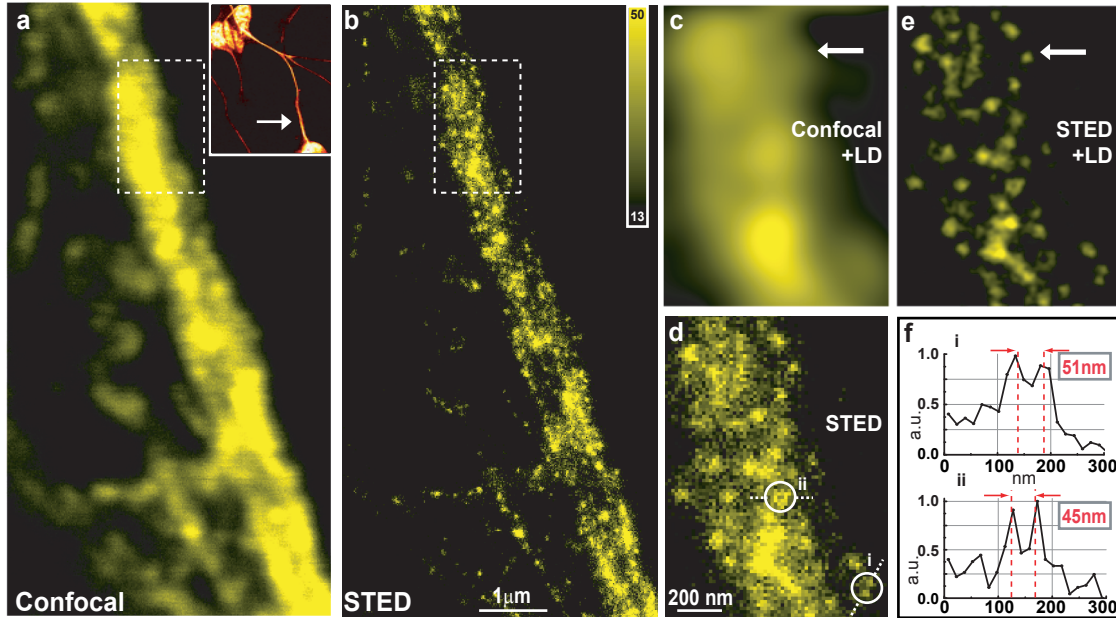
Figure 3.11: **Imaging neurofilaments in human neuroblastoma. Contrary to the confocal (a), the (b) STED recording displays details < 30 nm, as also highlighted by the comparison of image subregions bordered by dashed lines (c) and (d). (c, e) Subregion after linear deconvolution. Note that the deconvolved confocal image does not yield a substantial gain in information. (f) Profiles of raw data demonstrate the ability of (undeconvolved) STED data to reveal object structures that are far below the wavelength of light.**

crosslinks to organize and stabilize neurofilaments in axons ([93]). Neurofilaments play an essential role in many neurodegenerative diseases such as Parkinsons's. In contrast to the confocal (a) image, the STED (b) image identifies neurofilamental substructures of 20-30 nm size. This is particularly apparent in (d) showing a partial area of (b) at a larger magnification, as well as in (e) where the details are further enhanced by a linear deconvolution. The line plots of raw data in panel (f) prove that substructures that are only 45 nm apart are separated by a dip of 50 %. Interestingly the protein is not continuously distributed but mainly organized in chains of clusters. This becomes especially apparent when rather isolated axon areas of the neuron cells are imaged, as shown in Fig.3.12. The axon strand in the middle of the recording actually consists of two parallel chains of neurofilamental protein revealed only by STED microscopy (b). Each chain is
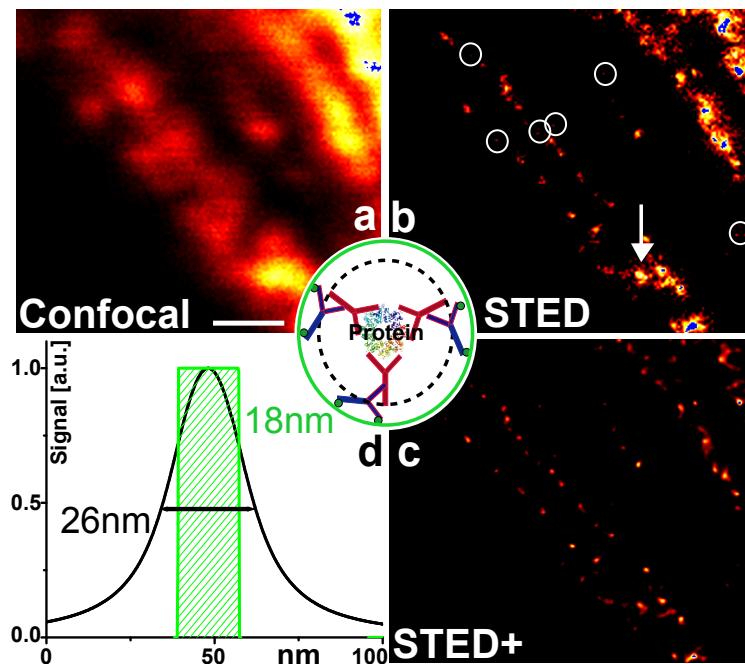
Figure 3.12: **Macromolecular scale fluorescence imaging close to the immunostaining limit. (Inset middle) Immunostaining schematic with primary and secondary antibody; the size of such a construct is estimated with ≈ 18 nm. (a) Confocal and (b) STED recording of rather isolated neurofilaments of an axon strand; the indicated areas (circles) mark protein clusters in the range of ≤ 24 nm FWHM. (c) RL-deconvolved STED data. (d) Convolution of an 18 nm object with a Lorentz-shaped profile of 20 nm FWHM leads to a theoretical object size ≈ 26 nm. Note that the measured STED profiles in (b) are below this value, indicating a true FWHM of the effective imaging PSF to be < 20 nm. Scale bar = 200 nm.**

represented by very small individual clusters of proteins and crosslinked by the same protein clusters as indicated by the arrow in (b). The STED image shows a bunch of these clusters each being in the order of ≤ 24 nm FWHM (indicated by circles). Note that the RL-deconvolved data (c) provides an extreme sharp contrast in resolution compared to the confocal recording in (a). Representing the convolution of the microscope's PSF with the spatial extent of the labeling, the FWHM of the profiles are just an upper limit for the actual imaging resolution. In fact, with a complex size of 6-8 nm for the protein, the secondary antibodies form an estimated 12-16 nm diameter volume around the similarly sized primary antibody ([94]). The whole construct therefore easily reaches diameter values of ≈ 18 nm (Fig.3.12 middle inset). Thus, the resolution has attained values that are close to the limits set by the labeling itself. A straight forward convolution of an 18 nm object with an estimated effective Lorentzian of 20 nm FWHM for the STED-PSF leads

to an image of 26 nm FWHM (d). This value is larger than the smallest object sizes defined by T-REX STED-microscopy in (b), which again indicates the focal plane resolution to be below 20 nm. Note that the sampling rate was 15 nm, thus leaving a theoretical chance of having underestimated the indicated cluster sizes. However, in Fig.3.12 (b) are approximately 39 clusters present with a FWHM > 30 nm and simultaneously are at least 6 clusters ≤ 24 nm indicated. Assuming a true cluster size of 24 nm the expected ratio of cluster images ≤ 24 nm and clusters > 30 nm due to a 15 nm sampling rate (30:6) is met in good agreement.

Conclusion

Intensity profiles of a FWHM of 22-30 nm (Fig.3.9, Fig.3.11, Fig.3.12) demonstrate the fundamental progress in resolution brought about by T-Rex STED-microscopy. The 10- to 12- fold multilateral increase in resolution below the diffraction barrier has been enabled by the elimination of the molecular triplet state excitation as a major source of photobleaching in STED-microscopy. The attained far-field optical resolution is similar to that of current high-end x-ray microscopy ([95]). In contrast to the latter, STED has the potential to provide 3D images without tomography and, what is perhaps more important, can harness fluorescence labeling. Moreover, the presented STED-microscopy results from various fields of cell biology show that lens-based fluorescence microscopy has reached macromolecular-scale resolution. This arguably unexpected power of light microscopy is anticipated to unravel many fundamental problems in life science.
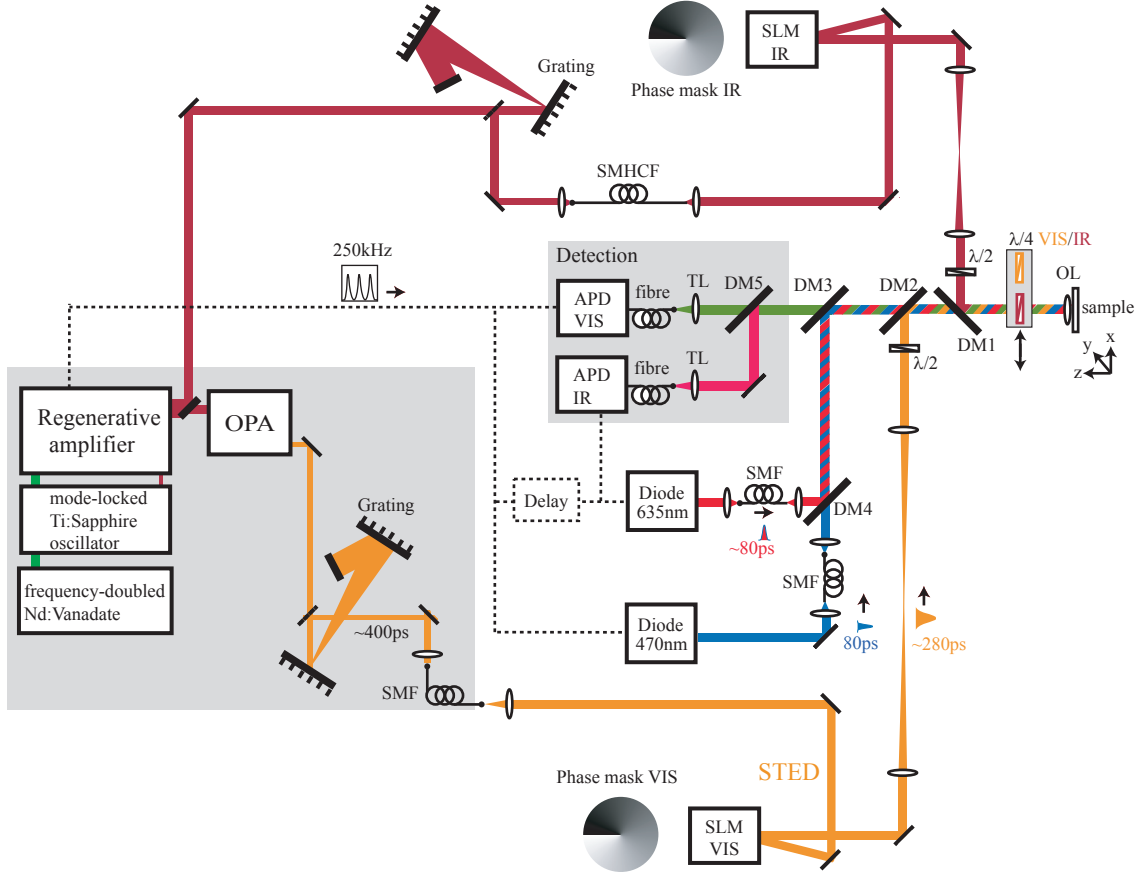
4 Dual-colour T-Rex STED-microscopy

The last chapter of this thesis presents the implementation of two independent imaging channels in a STED microscope and its first biological applications in terms of protein colocalization. In every biological project addressed by STED microscopy the discussions were at some point ruled by the question: What about the possibility of mapping out two individual proteins with subdiffraction resolution with the purpose of protein localization on the nanoscale? In fact, colocalization of proteins is a common method in fluorescence microscopy. Although the colocalization accuracy is not limited due to diffraction, however, in most cases the drawback of information quality is again due to the fact that two diffraction limited images are aligned to each other, thus not revealing any spatial information being smaller than ≈ 200 nm.

An obvious challenge toward discovering protein interactions on the molecular level is to colocalize different proteins on the nanoscale, which not only calls for two superresolution images of two different fluorophores but simultaneously for the ability of colocalization with accuracy one order of magnitude beyond what is needed for conventional optical imaging so far. In the following is pointed out how the experimental realization of the imaging components and the alignment procedure of both images has been worked out. In consequence, the investigation of the spatial relationship of two individual proteins at the nanoscale exemplified on endosomes and mammalian mitochandria can be presented.

4.1 Experimental realization of a Dual-Colour STED-microscope

Starting with a STED microscope optimized in its two wavelengths for effectively exciting and depleting a green fluorophore in the visible (emission maxima at 550 nm) I headed for the straight forward approach to introduce two additional independent laser beams in the microscope, which operate a second (red) fluorophore (emission maxima at 680 nm) under STED conditions. This approach requires the necessity for generating two independent doughnut shaped depleting pulses. To this end, half of the infrared pulse energy provided by the regeneratively amplified mode-locked Ti:sapphire oscillator was

used to pump an OPA thus generating the visible STED beam at 603 nm and the second half directly supplied the setup with infrared pulses of 780 nm, ≈ 200 fs pulse duration and energies up to 1.5 μJ, as shown in Fig.4.1 (see supplememt in ([96])).


Figure 4.1: Experimental setup of a Dual-Colour STED-microscope featuring T-Rex conditions for a green and a red fluorophore. See text for explanation.

To stretch the infrared STED light (similarly to the visible beam) to ≈ 300 ps ([31])) by up-chirping, it was diffracted from a pair of gratings before being coupled to a 2-m hollow-core fibre (Air6-800, Photonic Crystal Fibers, Denmark). Both fluorescent dyes (Atto 532 and Atto647N, respectively) were excited via two laser diodes emitting at 470nm and 635nm (Picoquant, Berlin, Germany), each of them electronically synchronized with the according STED pulse train. The conversion of both STED beams into doughnut-shaped light distributions were individually carried out by means of two spatial light modulators (Hamamatsu, Hamamatsu City, Japan) each delivering a (0-2π) helical phase ramp. In combination with circular polarized light, this imprinted phase distribution generates in the focal plane of an objective lens the typical doughnut shaped light distribution

featuring a singularity in the middle. Since the polarizations at both STED wavelengths have to be organized perfectly circular, this could not simply be achieved by a single phase-quarterplate ($\lambda/4$) likely because of chromatic imperfections of this optical element regarding wavelengths being ≈ 180 nm separated. For this reason two ($\lambda/4$)-phaseplates were introduced, one optimized for the visible and the other one for the infrared, on a repositionable mount. Accordingly the ($\lambda/4$)-phaseplates had to be switched between subsequent recordings of both colours (Fig.4.1). The central phase singularity of the modified beams coincided with the optical axis. All four beams were coupled via carefully dichroic filtering into the aperture of the 1.4 oil immersion lens.

On a first look the handling of four laser beams might be recognized as inconvenient complexity, however, this strategy provides the user with the valuable benefit of preventing spectral overlap of the fluorescence windows, thus having cross-talk free spatial information of both imaging channels. The dichroic handling of four wavelength and two fluorescence windows (545/50 and 680/50, AHF Analysentechnik, Germany) is illustrated in Fig.4.2.
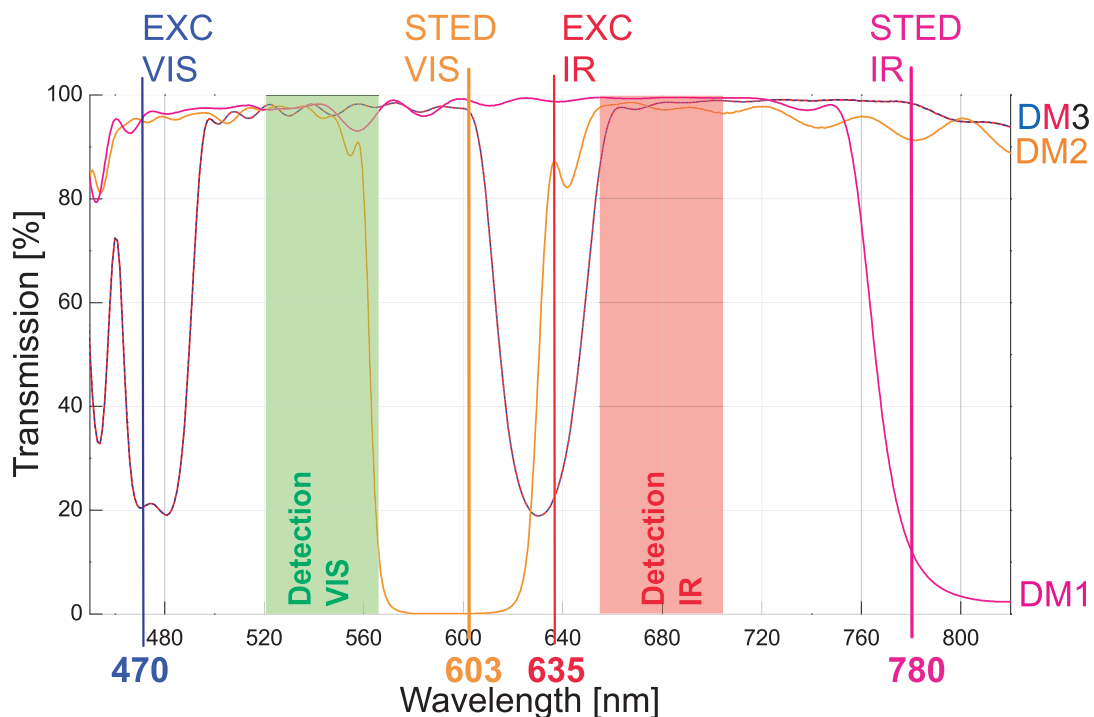
Figure 4.2: Dichroic filter setup and detection windows for a green and a red fluorescent dye in a Dual-colour STED-microscope. Position of the dichrioc filters DM1, DM2 and DM3 in the setup see Fig.4.1.

The most critical dichroic mirror is DM2 (see also Fig.4.1) due to the various demands

regarding its position in the setup: the 600 nm visible STED light has to be coupled into the microscope, while already 635 nm for the red excitation must pass effectively through it; additionally both detection windows need to be fully transmitted. Note that within the two detection windows all diochroic mirrors (except DM2 at its red edge) deliver more than 90 % transmission. Matching both spectral detection windows, both fluorescence maxima of the used organic fluorophores (Atto532 and Atto647N) are separated by 130 nm which prevents fluorescence cross talk in both detection channels.

The spectral separation is especially necessary, since the visible STED beam meets the excitation spectra of the red dye, which is hardly to prevent by using two independent STED wavelengths. This fact has two major implications on the recording procedure of both colour images: firstly, considering the STED intensity to be more than three orders of magnitude higher than the excitation light intensity, the red fluorophore is immediately bleached out when scanning the visible STED beam through the sample. Therefore the complete image of the red fluorophore has to be taken line by line in confocal- and STED-mode consequently before similarly capturing the distribution of the green dye.

Secondly, as both superresolution images of both colours have to be taken one after the other a reliable alignment procedure with nanoscale accuracy becomes necessary. To this end, two independent alignment procedures were established, one of them utilizing two-colour labeled fluorescent beads (Molecular Probes, Leiden, Netherlands), which provide a colocalization accuracy down to ± 5 nm (see Appendix A.3).

Fig.4.3 (a,b) shows the measured spots of the visible pulse pair at 470 nm and 603 nm, while (d) and (e) render the infrared counterpart beams at 635 nm and 780 nm. All four wavelengths were measured on the same gold nanoparticle for probing the different light distributions via scattering. To demonstrate the resolving power of the individual imaging channels, I measured the upper limit of the effective point spread functions by averaging 35 individual yellow-green fluorescence beads and 30 individual examples of crimson fluorescence beads (Molecular Probes Eugene, OR), respectively. Both fluorophores are not specified, but the manufacturer provided the size distribution to vary by 4 nm around a mean diameter of 24 nm with electron microscopy for both cases. The results are depicted in (c,f) revealing a bead image of 25 nm and 65 mn for the green and the red channel respectively ([96]). Note that the red imaging channel was limited to 65 nm in this study, since the STED wavelength of the infrared beam could not be tuned below 780 nm, which is not the optimal depleting wavelength for the red fluorophore. With another iteration of improving the red imaging channel for utilizing wavelength tunability, the resolution in the red channel is expected to meet the conditions of the green counterpart.

In the following the applicability of two STED beams and two excitation light sources for taking double colour images with diffraction unlimited resolution will be the center of interest.
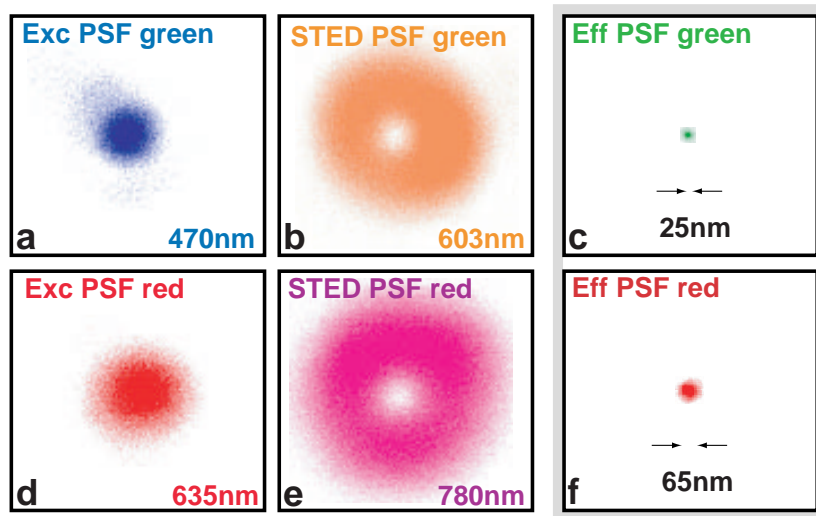
Figure 4.3: STED microscopy operating spectrally separated fluorophores at four different wavelengths. Measured focal spots (PSFs) for excitation and depletion beam in the green (a,b) and the red counterparts (d,e), respectively. The blue spot (a) features a FWHM of 190 nm, whereas the red spot (d) provides 250 nm FWHM. The effective spots operating under STED conditions are depicted for both channels in c and f featuring a FWHM of 25 nm and 65 nm, respectively.
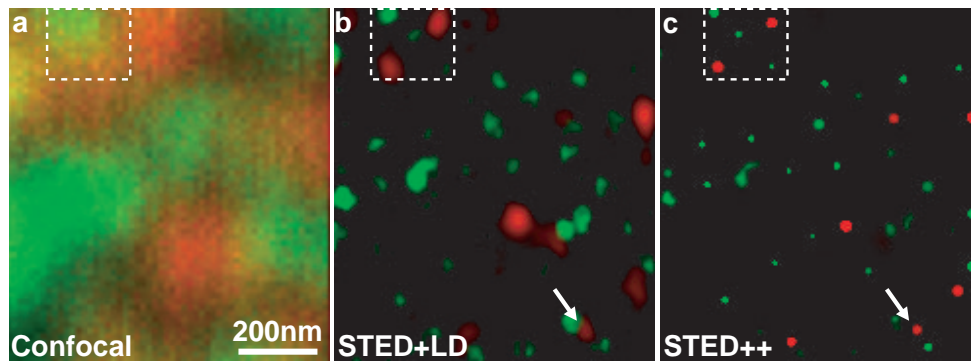
4.2 Performance of a Dual-Colour STED-microscope

The first demonstration of a successful expansion of STED microscopy to Dual-Colour operation is done by imaging of yellow-green and crimson fluorescence beads emitting in the 500-530 nm and 640-670 nm range, spread out on a silaniced cover slip, as shown in Fig.4.4. The imaging parameters were 3 ms (5 ms) pixel dwell time for the green (red) colour image, the applied excitation peak powers were I_{470nm}=4,2 MW/cm^2 and I_{635nm}=4,9 MW/cm^2 throughout the measurements and the STED peak powers were adjusted to $I_{STED(603nm)}^{max}$ =3,4 GW/cm^2 and $I_{STED(780nm)}^{max}$= 1,1 GW/cm^2.

Panel (a,c) depict both confocal recordings, while only the according RL-deconvolved STED recordings can provide object information on individual bead positions as depicted in (b,d). Insets in (a) and (b) show the confocal recordings of the same area before and for the visible case also after both STED recordings. Note, that the measured intensity distributions are not influenced by the STED beams, particularly the visible dye is not compromised by the red STED-beam previously being scanned through the specimen. In (e,f) the aligned confocal and RL-deconvolved STED recordings (see Appendix A.3, first alignment method applied) are presented. Fig.4.4 (f) identifies beads of opposite colour being 26 nm apart from each other. Panel (g) depicts fluorescence depleting curves
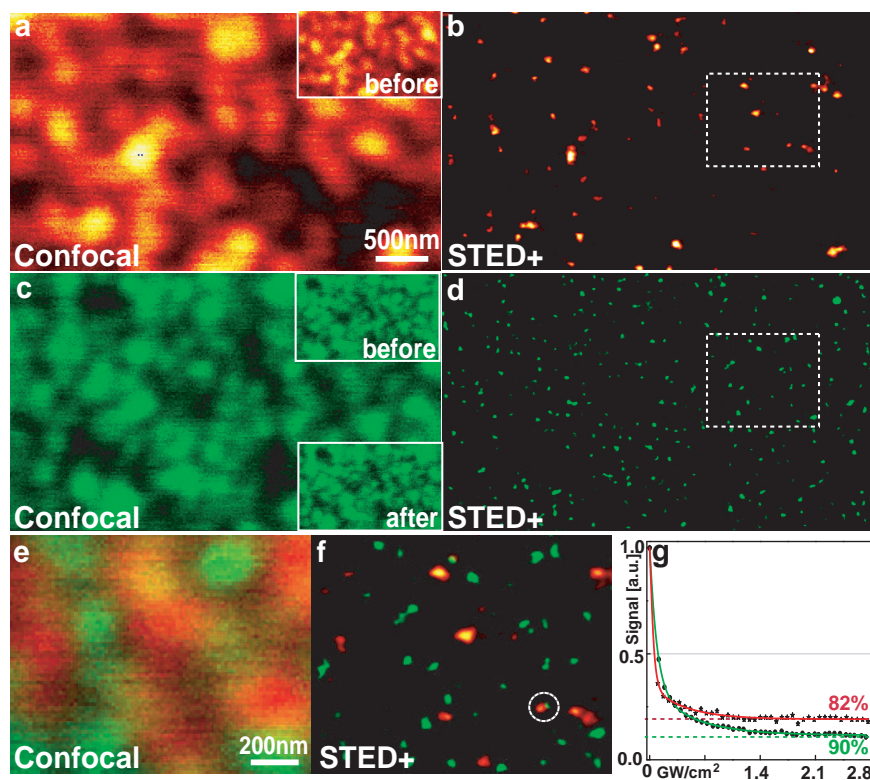
Figure 4.4: Imaging procedure of both STED channels exemplified on fluorescence beads of two species, yellow-green and crimson fluorescence beads. Confocal (a) and RL-deconvolved STED (b) recording, taken line-by-line in the red channel. Respectively the green channel imaged afterwards on the same sample area (c,d). (Inset in (c)) Low-magnification confocal recordings before and after the STED imaging procedure. Note, that the image "after" is not distorted by both STED-images taken previously and shows congruency with the confocal image taken at the beginning ("before"). (e,f) Magnified and aligned outtakes of (a-d); f represents a Dual-colour superresolved STED image with two opposite colour beads indicated to be < 30 nm apart. (g) Depleting efficiencies for the yellow-green and the crimson fluorescence beads against the according depleting intensity $\mathbf{I}_{STED}^{max}$ for the visible and the infrared STED beam, respectively.

for the yellow-green and the crimson fluorescence beads against the maximum applied depleting intensity $\mathbf{I}_{STED}^{max}$ at the doughnut crest, for the visible (603 nm) and the infrared (780 nm) STED beam, respectively. Note the higher depleting efficiency of the visible STED beam (90%) against the infrared counterpart (82%). This undepleted fluorescence is the reason for the pronounced confocal background in the red STED images, which should be effectively minimized by tuning down the STED wavelength for the infrared depleting beam. As the effective PSF width is in the order of the spatial distance of

characteristic object features, additional information can be extracted from the recorded images by utilizing photon localization methods ([97],[98]) (see Appendix A.4). The idea is to exploit a-priori object knowledge by identifying distinct localizations of separable bead positions and substituting the recorded area with the real objects of a 24 nm bead projection. The results are shown in Fig.4.5. As expected the new restoration technique

Figure 4.5: **Resolution of < 30nm (green) and ≈ 65nm (red) in the focal plane of a Dual-colour STED-microscope. The confocal image (a) fails to resolve the bead agglomeration, whereas the corresponding STED image (b) displays every separable 24 nm red and green bead. Applying a restoration algorithm (see Appendix A.4), the maximum clarity of the object is gained (c). Note that two individual beads of different colour indicated by arrows in (c) being 52 nm apart are perfectly separated with nm precision. Within the dashed area in (c) the object is fully restored by applying the algorithm on the STED data.**

increases the localization ability of the beads in the restored image. The positions of isolated bead images can be estimated with accuracy of a few nm or even less. Therefore also distances between neighbored bead images of different colour down to 52 nm indicated by arrows in (c) could be estimated with nm precision. Note that in case of identifying every single bead by STED-microscopy in the recorded area, the object would be fully restored by this advanced restoration procedure.

4.3 Nanoscale colocalization studies of two individual proteins

4.3.1 Colocalization of synaptic vesicle proteins on endosomes

Having demonstrated the operation principle of imaging two independent superresolution images with nanoscale colocalozation ability on bead samples I turned back to biologi-

cal imaging of individual proteins. Resuming the study of protein distribution on the endosomes of PC12 cells from section (3.3.2), this time double-labeled endosomes with two synaptic vesicle proteins, synaptotagmin I and synaptophysin, tagged with the red (Atto647N) and green (Atto532) fluorophor, respectively, were investigated. PC12 cells contain abundant small synaptic-like vesicles, which they can release upon stimulation. The vesicles are generated (and possibly recycled) through the endosomal compartment, which contains a variety of synaptic vesicle proteins. The earlier mentioned hypothesize that during vesicle biogenesis/recycling, domains rich in synaptic proteins would enrich on the endosomes, and then "break off" to form new vesicles could be further addressed ([92]): Are all synaptic vesicle proteins localized to the same places on the endosome?

To clarify this question a cellular fraction highly enriched in early endosomes was prepared, both proteins were immunostained, and finally STED imaging ($I_{STED(603nm)}^{max} = $
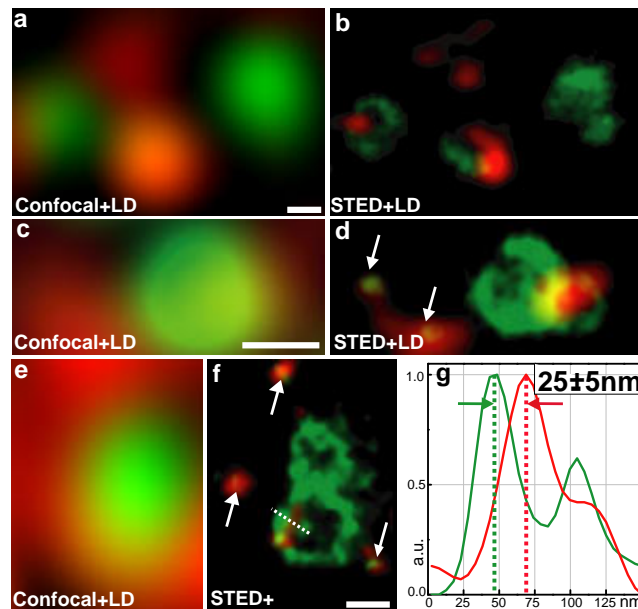
Figure 4.6: Resolving the nanostructure of two synaptic proteins, synaptotagmin I (red) and synaptophysin (green) on endosomes. (a) LD-deconvolved confocal reference, (b) STED microscopy plus LD (RL for f) (see Appendix A.2) revealing large, ring-shaped domains, while the by far less abandoned protein forms largely puncta-like structures. (c-f) Additionally there are double-labeled fluorescence beads incorporated in the sample, being distinguishable by providing a superresolved fluorescence bead image in both channels simultaneously (indicated by arrows in d and f). The alignment procedure for the indicated beads allows alignment precision of ±5 nm (see appendix A.3). Localization profiles of both proteins are reliable within this accuracy as shown in (g). Scale bar = 100 nm.

1,2 GW/cm^2 and I$_{STED(780nm)}^{max}$ = 0,7 GW/cm^2) was performed on individual endosomes ([96]). Fig.4.6 displays fully aligned images of the localization of both proteins. Confocal and STED recording were subject to a linear deconvolution (RL-deconvolution in (f)) for maximizing the information content. Synaptophysin is by far the more abundant protein. It resulted in large, ring-shaped domains as revealed in the green channel of Fig.4.6 (and Fig.3.10). In contrast, synaptotagmin I formed puncta-like domains, which largely colocalize with synaptophysin-containing structures (red channel in Fig.4.6, compare also with Fig.3.9). Thus, surprisingly, not all synaptic vesicle proteins occupy the same sites on the endosomes. One possible explanation for this phenotype is that synaptophysin-containing sites that lack syaptotagmin I could contain other isoforms such as synaptotagmin IX ([99]). Alternatively, it is possible that not all synaptophysin is directed toward synaptic vesicle formation - only the sites where proteins like synaptotagmin also exist are going to generate new vesicles, with other synaptophysin patches remaining on the endosome. Note that the corresponding confocal images in (a,c,e) cannot provide any information toward the localization of the two proteins on the endosomes; even rarely can be estimated, if both proteins exist on the same endosome or not.

It should be mentioned that in (c,d) four fluorophores are imaged during the acquisition procedure with two of them fluorescing in the green (Atto532 and yellow-green dye from the double-colour beads) and two in the red channel (Atto647 and crimson fluorophore from the double-colour beads), respectively. All four dyes can be effectively quenched by the corresponding STED depleting beams, which illustrates again that the depleting phenomena is a common photophysical behaviour of fluorescing molecules in general. Superresolved images of fluorescence beads within the recorded area, which are displayed in both channels are indicated by arrows (d). Fluorescence, which only occurs in one of the channels is referred to as fluorescence signal of the tagged proteins.

The images of the two-colour reference beads are utilized for overlaying both STED images with an accuracy corresponding to ± 5 nm. Within this presicion the double-colour intensity profile in (f) displays a profile of protein distribution of synaptotagmin I (red) and synaptophysin (green), being 25 nm apart from each other. Nanoscale localization of different proteins on endosomes opens up new possibilities in the study of vesicle formation.

4.3.2 Two-colour imaging of ATP synthase and translocase (TOM20) in mammalian mitochondria

Finally I applied the superresolving power of two-colour STED microscopy on two proteins from different compartments of mitochondria in mammalian PtK2 cells. Having shown,
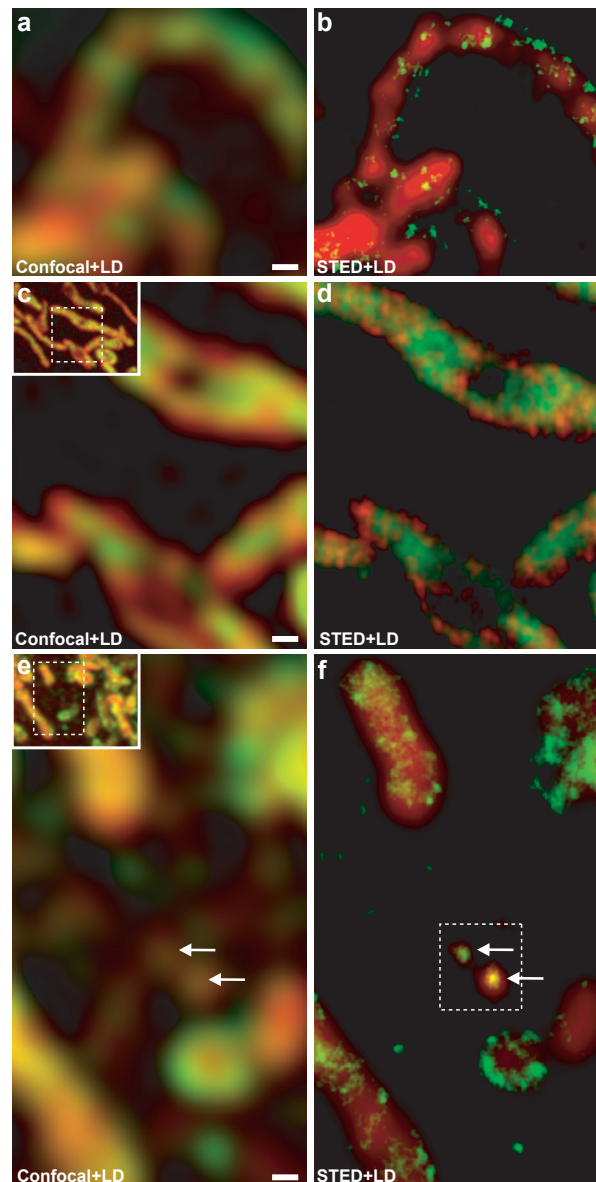
Figure 4.7: Inset in (c,e) indicating site of recording. Contrary to the confocal plus LD recording (a), only the STED plus LD image (b) displays major differences in the protein distribution patterns; the translocase of the mitochondrial outer membrane (TOM20) is located in distinct clusters (at the mitochondrial surface, green pattern in b,f), whereas the visualization of the distribution of the F_1F_0ATP synthase shows a homogeneous staining pattern (red in b,f). The observed staining patterns are independent from the used secondary antibodies shown by interexchange of the labeling colours (c,d). Additional incorporation of double labeled beads (indicated by arrows; note that the red colourmap is adjusted within the dashed box) for nanoscale precise alignment (± 5 nm) of both channels (e,f). Scale bar = 200 nm.

that the mitochondria protein ANT provides strong clustering behaviour (Fig.3.5 (d)) further proteins in the complex structure of the mitochondrial organelle were to be investigated in terms of spatial arrangement. Fig.4.7 displays fully aligned images from the mitochondrial ATP synthase and simultaneously the translocase (TOM20) of the mitochondrial outermembrane of immunolabeled mammalian cells ([96]). ATP is part of the mitochondrial F_1F_0ATP synthase complex, residing in the mitochondrial inner membrane. Electron microscopy demonstrated a dense packing of the F_1F_0ATP synthase complex along the inner membrane ([100]). The TOM complex mediates the transport of nuclear encoded mitochondrial preproteins across the mitochondrial outer membrane. The distribution of this complex within the outer membrane is less clear. The TOM complex has been suggested to be specifically enriched in so-called contact sites, regions at which the inner and the outer membranes are in close spatial proximity, although compelling experimental evidence is missing ([101]). To investigate the relative distributions of both complexes two-color STED microscopy was employed. One finds that the F_1F_0ATP synthase is practically homogeneously distributed along mitochondrial tubules (red colour in Fig.4.7 (b), (f)). Tom20, marking the localization of the TOM complex, however, is localized into distinct foci along mitochondrial tubules (green colour in Fig.4.7 (b), (f)). This protein specific localization of ATP and TOM20 is not changed when exchanging the labeling colour of both proteins displayed in (c,d). Accordingly, now the red protein distribution is recalling the clustering behaviour of TOM20. For nm-precision alignment there were also double-labeled fluorescent beads incorporated during the sample preparation process (see Appendix A.3), as shown in Fig.4.7 (e,f). Signal, which is present in both channels simultaneously is recognized as bead signal (indicated by arrows) and is used for direct alignment of the confocal and also the STED images respectively.

The spotted distribution of the TOM complex is only resolvable with the superior resolution of STED-microscopy, but not by conventional confocal microscopy. Therefore it has previously not been possible to resolve the sub-mitochondrial localization of the TOM complex. It will be enlightening to understand the molecular basis for the localization of this complex into clusters and to correlate the distribution of Tom20 with distinct mitochondrial morphological structures, possibly with contact sites.

Conclusion

The feasibility of reaching subdiffraction resolution in two separated colour channels allows the localization of individual protein nanopatterns down to the molecular level. The resolution of ≈ 65 nm in the red channel was limited compared to the green channel because of the lack of wavelength tunability for the red STED beam. By wavelength optimization the performance of the red channel is expected to meet the conditions of the green STED image (resolution < 30 nm). While electron microscopy (EM) provides

the possibility for imaging immunolabeled protein structures with high spatial resolution hence not being comparably competitive in the here shown examples of superresolution light microscopy, it seems to be nearly impossible to do protein colocalization studies. The accuracy of aligning both high resolution fluorescence images was shown to reach nm-precision. The progress in biological microscopy presented herein should facilitate the imaging of protein colocalization in cells with unreached clarity thus opening up a new method of fundamentally addressing problems in life science.

5 Conclusion and Outlook

The implementation of the dark-state relaxation (D-Rex) illumination scheme in STED-microscopy enabled to increase the resolution performance down to molecular scales of ≈ 20 nm. This increase in resolution is based on an improved photostability and on a major fluorescence signal increase per pulse under the D-Rex conditions, also allowing to apply much larger STED powers. Large STED powers have to be applied to reach highest resolution in STED-microscopy, so far debased by the photostability of the fluorescence labels. The comprehensive study of the impact of repetition rate reduction on one- and two-photon excitation in microscopy in general revealed that photobleaching at large excitation powers mainly occurred via the dark state, identified as the triplet state. Photobleaching can be effectively prevented by ensuring full dark state relaxation between subsequent excitation events. An optimum excitation scheme was realized, identified as pulsed illumination with a pulse repetition rate below 1MHz for both excitation modes, as exemplified on a rhodamine-related organic dye and on the green fluorescent protein (GFP), the archetype of fluorescent proteins. In fact, the fluorescence signal before bleaching was boosted by a factor of 18 for GFP and 7 for Atto532 for one-photon excitation and by a factor of 12 and 10 in the case of two-photon excitation on comparing the high and low repetition rate regimes, respectively. Altogether, the D-Rex illumination scheme, being all-physical, is expected to improve many biotechnological applications that rely on fluorescence.

Motivated by those results, a STED setup established with pulsed repetition rate of 250 kHz has proven a lateral performance of below 20 nm resolution tantamount to a 10- to 12- fold multilateral increase in resolution below the diffraction barrier which has yet been unattainable for biological fluorescence microscopy. This macromolecular-scale resolving ability was achieved inside immunolabeled cells demonstrated on a wide spread of biological applications, including imaging of membrane microdomains, vesicle proteins on endosomes and vesicles, mitochondrial proteins in mammalian cells, proteins of cell junction and focal adhesion, proteins from the olfactory system for odor signal transduction, and a neurofilamental protein in human neuroblastoma. The broad range of applications and biological questions addressed demonstrated imposingly the compatibility of super-resolution STED-microscopy to cell biology.

Beyond this, the T-Rex STED-microscope was extended to feature two independent su-

perresolving detection channels thus setting up the first method to colocalize different proteins on the nanoscale. To this end, four independent laser beams were coupled into the objective lens to independently image two fluorescent species, the green-emitting Atto532 and the red-emitting Atto647N, under STED conditions. Moreover, two independent alignment procedures were introduced to colocalize both images with a precision of up to ±5 nm. The method was able to resolve the so far unrevealed nanopatterns of two individual proteins on endosomes, as well as two proteins of mammalian mitochondria. For obvious reasons, superresolution colocalization ability sustainably widens the application field of STED-microscopy to studying molecular protein localization on the nanoscale.

Further progress in imaging capability should be possible in combination with axial resolution increasing strategies, such as 4Pi-microscopy. The STED-4Pi technique has already proven a resolution of < 40 nm in axial direction ([102],[103]). A combined strategy should have the potential of reaching real 3D nanoscale resolution without tomography. For the same purpose, one could think of additionally using phase masks for engineering a STED PSF addressing a z-resolution increase ([104]), as already shown for FCS applications in subdiffraction focal volumes ([9]) and also for biological imaging ([105]).

Further efforts are necessary to render a STED microscope applicable for live-cell imaging. Here the D-Rex modality is helpful in its implementation in fast beam scanning utilizing high repetition rate lasers. With the resultant fluorescence increase and gain in speed, the resulting imaging times are predicted to be even below the common imaging times in current scanning confocal microscopy, as already discussed in section (2.3). Supporting these efforts are the very promising developments in the use of fluorescent proteins for STED imaging. Having demonstrated the use of GFP for sub-diffraction STED imaging ([106]), further optimization by consequently exploiting the meanwhile established variety of photochemically differing fluorescent proteins is to be expected. This would pool together all the ingredients for live-cell STED imaging.

Other implementation strategies of the RESOLFT concept, such as ground state depletion (GSD) ([107]) are also making progress in taking the last step of experimental realization, while protein photoswitching has recently been vindicated ([21]). All these implementations can be combined with photon statistical localization methods ([97]), in the same manner like exemplarily shown in this thesis for the STED imaging of fluorescent beads, to further improve the resolution in fluorescence microscopy.

The different highlighted options in further improving optical microscopy to reach the ultimate goal of multicolour 3D live-cell imaging on the nanoscale are under careful investigation, while improvements are to be realized in the near future.

Bibliography

[1] E. Abbe. Beiträge zur theorie des mikroskops und der mikroskopischen wahrnehmung. *Arch. f. Mikr. Anat.*, 9:413–420, 1873.

[2] T. Wilson and C. J. R. Sheppard. *Theory and practice of scanning optical microscopy.* Academic Press, New York, 1984.

[3] T. Wilson (ed.). *Confocal microscopy.* Academic Press Ltd., London, 1990.

[4] L. Reimer. *Scanning electron microscopy.* Springer Series in Optical Sciences. Springer-Verlag, Berlin, Heidelberg, New York, Tokyo, 1985.

[5] M. Minsky. Microscopy apparatus, 1961.

[6] W. Denk, J. H. Strickler, and W. W. Webb. Two-photon laser scanning fluorescence microscopy. *Science*, 248:73–76, 1990.

[7] M. Göppert-Mayer. Über elementarakte mit zwei quantensprüngen. *Ann. Phys. (Leipzig)*, 9:273–295, 1931.

[8] W. Denk. Two-photon excitation in functional biological imaging. *J. Biomed. Opt.*, 1:296–304, 1996.

[9] Lars Kastrup, Hans Blom, Christian Eggeling, and Stefan W. Hell. Fluorescence fluctuation spectroscopy in subdiffraction focal volumes. *Phys. Rev. Lett.*, 94:178104, 2005.

[10] S. W. Hell and E. H. K. Stelzer. Fundamental improvement of resolution with a 4pi-confocal fluorescence microscope using two-photon excitation. *Opt. Commun.*, 93:277–282, 1992.

[11] S. W. Hell, M. Dyba, and S. Jakobs. Concepts for nanoscale resolution in fluorescence microscopy. *Curr. Opin. Neurobio.*, 14(5):599–609, 2004.

[12] H. Gugel, J. Bewersdorf, S. Jakobs, J. Engelhardt, R. Storz, and S.W. Hell. Cooperative 4pi excitation and detection yields 7-fold sharper optical sections in live cell microscopy. *Biophys. J.*, 87:4146–4152, 2004.

[13] D. Axelrrod, E.H. Hellen, and E.M. Fulbright. Total internal reflection fluorescence. In J.R. Lakowicz, editor, *Topics in Fluorescence Spectroscopy: Biochemical Applications*, volume 3. Plenum Press, New York, 1992.

[14] A. Lewis, M. Isaacson, A. Harootunian, and A. Murray. Development of a 500 a resolution light microscope. *Ultramicroscopy*, 13:227–231, 1984.

[15] D. W. Pohl, W. Denk, and M. Lanz. Optical stethoscopy: Image recording with resolution l/20. *Appl. Phys. Lett.*, 44:651–653, 1984.

[16] E.A. Jares-Erijman and T. M. Jovin. Fret imaging. *Nature Biotechnol.*, 21(11):1387–1395, 2003.

[17] M.A. Hink, T. Bisseling, and A.J.W.G. Visser. Imaging protein-protein interactions in living cells. *Plant Mol. Biol.*, 50(6):871–883, 2002.

[18] P. Schwille, U. Haupts, S. Maiti, and W.W. Webb. Molecular dynamics in living cells observed by fluorescence correlation spectroscopy with one- and two-photon excitation. *Biophys. J.*, 77:2251–2265, 1999.

[19] S. W. Hell and J. Wichmann. Breaking the diffraction resolution limit by stimulated emission: stimulated emission depletion microscopy. *Opt. Lett.*, 19(11):780–782, 1994.

[20] S.W. Hell. Toward fluorescence nanoscopy. *Nature Biotechnol.*, 21(11):1347–1355, 2003.

[21] M. Hofmann, C. Eggeling, S. Jakobs, and S.W. Hell. Breaking the diffraction barrier in fluorescence microscopy at low light intensities by using reversibly photoswitchable proteins. *Proc. Natl. Acad. Sci. USA*, 102(49):17565–17569, 2005.

[22] E. Betzig, G.H. Patterson, R. Sougrat, O.W. Lindwasser, S. Olenych, J.S. Bonifacino, M.W. Davidson, J. Lippincott-Schwartz, and H.F. Hess. Imaging intracellular fluorescent proteins at nanometer resolution. *Science*, 313(5793):1642–1645, 2006.

[23] S.T. Hess, Thanu P. K. Girirajan, and M. D. Mason. Ultra-high resolution imaging by fluorescent photoactivation localization microscopy (fpalm). *Biophysical Journal*, 91:4258–72, 2006.

[24] Michael J. Rust, Mark Bates, and Xiaowei Zhuang. Sub-diffraction-limit imaging by stochastic optical reconstruction microscopy (storm). *Nature Methods*, 3:793–796, 2006.

[25] R. Heintzmann and C. Cremer. Laterally modulated excitation microscopy: improvement of resolution by using a diffraction grating. *SPIE Proc.*, 3568:185–195, 1998.

[26] M. G. L. Gustafsson. Nonlinear structured-illumination microscopy: Wide-field fluorescence imaging with theoretically unlimited resolution. *Proceedings of the National Academy of Sciences of the United States of America*, 102(37):13081–13086, 2005.

[27] M. Schwentker, H. Bock, M. Hofmann, S. Jakobs, J. Bewersdorf, and S. W. Hell. Wide-field subdiffraction resolft microscopy using fluorescent protein photoswitching. *Microscopy Research and Technique*, page in press, 2007.

[28] A. Einstein. Zur quantentheorie der strahlung. *Physik. Zeitschr.*, 18:121–128, 1917.

[29] M. Dyba, J. Keller, and S. W. Hell. Phase filter enhanced sted-4pi fluorescence microscopy: theory and experiment. *New Journal of Physics*, 7, 2005.

[30] J. Keller. Optimal de-excitation patterns for resolft-microscopy. *Dissertation, Department of NanoBiophotonics*, 2006.

[31] M. Dyba and S.W. Hell. Photostability of a fluorescent marker under pulsed excited-state depletion through stimulated emission. *Appl. Optics*, 42(25):5123–5129, 2003.

[32] James B. Pawley (ed.). *Handbook of biological confocal microscopy.* Springer, New York, 2nd edition, 2006.

[33] R. Y. Tsien, L. Ernst, and A. Waggoner. Fluorophores for confocal microscopy: Photophysics and photochemistry. In J. B. Pawley, editor, *Handbook of biological confocal microscopy*, pages 338–352. Springer, New York, 3 edition, 2006.

[34] W. W. Webb, K. S. Wells, D. R. Sandison, and J. Strickler. Criteria for quantitative dynamical confocal fluorescence imaging. In B. Herman and K. Jacobson, editors, *Optical Microscopy for Biology*, pages 73–108. Wiley, New York, 1990.

[35] Jose-Angel Conchello and Jeff W Lichtman. Optical sectioning microscopy. *Nat. Methods*, 2(12):920–931, 2005. TY - JOUR 10.1038/nmeth815.

[36] G. Donnert, C. Eggeling, and S. W. Hell. Major signal increase in fluorescence microscopy through dark state relaxation. *Nature Methods*, 4:81–86, 2007.

[37] G. J. Brakenhoff, J. Squier, T. Norris, A. C. Bliton, M. H. Wade, and B. Athey. Real-time two-photon confocal microscopy using a femtosecond, amplified ti:sapphire system. *J. Microsc.*, 181(3):253–259, 1996.

[38] E. Beaurepaire, M. Oheim, and J. Mertz. Ultra-deep two-photon fluorescence excitation in turbid media. *Opt. Commun.*, 188:25–29, 2001.

[39] E.J. Sanchez, L. Novotny, G.R. Holtom, and X.S. Xie. Room-temperature fluorescence imaging and spectroscopy of single molecules by two-photon excitation. *J. Phys. Chem. A*, 101:7019–7023, 1997.

[40] C. Eggeling, J. Widengren, R. Rigler, and C. A. M. Seidel. Photobleaching of fluorescent dyes under conditions used for single-molecule detection: Evidence of two-step photolysis. *Anal. Chem.*, 70:2651–2659, 1998.

[41] J. Widengren, Ü. Mets, and R. Rigler. Fluorescence correlation spectroscopy of triplet states in solution: A theoretical and experimental study. *J. Phys. Chem.*, 99:13368–13379, 1995.

[42] C. Eggeling, J. Widengren, R. Rigler, and C. A. M. Seidel. Photostabilities of fluorescent dyes for single-molecule spectroscopy: Mechanisms and experimental methods for estimating photobleaching in aqueous solution. In W. Rettig, B. Strehmel, M. Schrader, and H. Seifert, editors, *Applied fluorescence in chemistry, biology and medicine*, pages 193–240. Springer, Berlin, 1999.

[43] G. H. Patterson and D. W. Piston. Photobleaching in two-photon excitation microscopy. *Biophys. J.*, 78:2159–2162, 2000.

[44] C. Eggeling, A. Volkmer, and C. A. M. Seidel. Molecular photobleaching kinetics of rhodamine 6g by one- and twp-photon induced confocal fluorescence microscopy. *ChemPhysChem*, 6:791–804, 2005.

[45] M. Kasha. Paths of molecular excitation. *Rad. Res. Suppl. 2*, (243-275), 1960.

[46] H. J. Koester, D. Baur, R. Uhl, and S. W. Hell. Ca2+ fluorescence imaging with pico- and femtosecond two-photon excitation: signal and photodamage. *Biophys. J.*, 77:2226–2236, 1999.

[47] T. Nagai, K. Ibata, E.S. Park, M. Kubota, K. Mikoshiba, and A. Miyawaki. A variant of yellow fluorescent protein with fast and efficient maturation for cell-biological applications. *Nat. Biotechnol.*, 20:87–90, 2002.

[48] C. Xu and W. W. Webb. Measurement of two-photon excitation cross-sections of molecular fluorophores with data from 690 to 1050 nm. *J. Opt. Soc. Am. B*, 13:481–491, 1996.

[49] P.S. Dittrich and P. Schwille. Photobleaching and stabilization of fluorophores used for single-molecule analysis with one- and two-photon excitation. *Appl. Phys. B*, 73:829–837, 2001.

[50] T.-S. Chen, S.-Q. Zeng, Q.-M. Luo, Z.-H. Zhang, and W. Zhou. High-order photobleaching of green fluorescent protein inside living cells in two-photon excitation microscopy. *Biophys. Biochem. Res. Commun.*, 291:1272–1275, 2002.

[51] M. Yamashita, A. Kuniyasu, and H. Kashiwagi. Intersystem crossing rates and saturation parameters in the triplet state for rhodamine, fluorescein, and acridine dyes. *The Journal of Chemical Physics*, 66(3), 1977.

[52] S. Reindl and A. Penzkofer. Higher excited-state triplet-singlet intersystem crossing of some organic dyes. *Chem. Phys.*, 211:431–439, 1996.

[53] G. Donnert, J. Keller, R. Medda, M. A. Andrei, S. O. Rizzoli, R. Lührmann, R. Jahn, C. Eggeling, and S. W. Hell. Macromolecular-scale resolution in biological fluorescence microscopy. *Proc. Natl. Acad. Sci. USA*, 103(31):11440–11445, 2006.

[54] V. Westphal and S.W. Hell. Nanoscale resolution in the focal plane of an optical microscope. *Phys. Rev. Lett.*, 94:143903, 2005.

[55] A. Hopt and E. Neher. Highly nonlinear photodamage in two-photon fluorescence microscopy. *Biophys. J.*, pages 2029–2036, 2001.

[56] K. I. Willig, S. O. Rizzoli, V. Westphal, R. Jahn, and S. W. Hell. Sted-microscopy reveals that synaptotagmin remains clustered after synaptic vesicle exocytosis. *Nature*, 440(7086):935 – 939, 2006.

[57] P. Torok and P. R. T. Munro. The use of gauss-laguerre vector beams in sted microscopy. *Optics Express*, 12(15):3605–3617, 2004.

[58] K. Weber, P. C. Rathke, and M. Osborn. Cytoplasmic microtubular images in glutaraldehyde-fixed tissue culture cells by electron microscopy and by immunofluorescence microscopy. *Proc. Natl. Acad. Sci. USA*, 75(4):1820, 1978.

[59] R. J. Kittel, C. Wichmann, T. M. Rasse, W. Fouquet, M. Schmidt, A. Schmid, D. A. Wagh, C. Pawlu, R. Kellner, K. I. Willig, S. W. Hell, E. Buchner, M. Heckmann, and

S. J. Sigrist. Bruchpilot promotes active zone assembly, ca2+-channel clustering, and vesicle release. *Science*, in press, 2006.

[60] R. Jahn, T. Lang, and T.C. Sudhof. Mambrane fusion. *Cell*, 112(4):519–533, 2003.

[61] S. W. Hell, K. I. Willig, M. Dyba, S. Jakobs, L. Kastrup, and V. Westphal. Nanoscale resolution with focused light: Sted and other resolft microscopy concepts. In J. Pawley, editor, *Handbook of Biological Confocal Microscopy*, pages 571–579. Springer, New York, 2006.

[62] S. Takamori. Molecular anatomy of a trafficking organelle. *Cell*, 127:831–846, 2006.

[63] H. de Wit, Y. Lichtenstein, H.J. Geuze, R.B. Kelly, P. van der Sluiys, , and J. Klumperman. Synaptic vesicles form by budding from tubular extension of sorting endosomes in pc12 cells. *Molecular Biology of the Cell*, 10:4163–76, 1999.

[64] T. Gropp, N. Brustovetsky, M. Klingenberg, V. Müller, K. Fendler, and E. Bamberg. Kinetics of electrogenic transport by the adp/atp carrier. *Biophysical Journal*, 77:714–26, 1999.

[65] W. Fischle, Y. Wang, and C.D. Allis. Histone and chromatin cross-talk. *Current Opinion in Cell Biology*, 15:172–183, 2003.

[66] R. Zaidel-Bar, R. Milo, Z. Kam, and B. Geiger. A paxillin tyrosine phosphorylation switch regulates the assembly and form of cell-matrix adhesions. *Journal of Cell Science*, 120:137–148, 2007.

[67] M. Arnold, E.A. Calvanti-Adam, R. Glass, J. Blümmel, W. Eck, M. Kantlehner, H. Kessel, , and J. Spatz. Activation of integrin function by nanopatterned adhesive interfaces. *ChemPhysChem*, 5:383–388, 2004.

[68] D.L. Spector. Macromolecular domains within the cell nucleus. *Annu. Rev. Cell Biol.*, 9:265–315, 1993.

[69] T. Misteli and D.L. Spector. The cellular organization of gene expression. *Curr. Opin. Cell Biol.*, 10:323–331, 1998.

[70] P. J. Mintz and D. L. Spector. Compartmentalization of rna processing factors within nuclear speckles. *Journal of Structural Biology*, 129(2-3):241–251, 2000. Times Cited: 33 Article English Cited References Count: 68 316ep.

[71] A. Monneron and W. Bernhard. Fine structural organization of interphase nucleus in some mammalian cells. *Journal of Ultrastructure Research*, 27(3-4):266–288, 1969. Times Cited: 558 Article English Cited References Count: 56 D2537.

[72] S. Singer and G. L. Nicolson. The fluid mosaic model of the structure of cell membranes. *Science (Washington, D. C., 1883-)*, 175:720–31, 1972.

[73] A. Kusumi, C. Nakada, K. Ritchie, K. Murase, J. Kondo, and T. Fujiwara. Paradigm shift of the plasma membrane concept from the two-dimensional continuum fluid to the partitioned fluid: high-speed single-molecule tracking of membrane molecules. *Annu Rev Biophys Biomol Struct*, 34:351–78, 2005.

[74] J. J. Sieber, K. I. Willig, C. Kutzner, C. Gerding-Reimers, B. Harke, G. Donnert, B. Rammer, C. Eggeling, S. W. Hell, H. Grubmüller, and T. Lang. Anatomy and dynamics of a supramolecular membrane protein cluster. *submitted to Science*, 2007.

[75] J. J. Sieber, K. I. Willig, R. Heintzmann, S. W. Hell, and T. Lang. The snare-motif is essential for the formation of syntaxin clusters in the plasma membrane. *Biophys. J.*, 90:2843–2851, 2006.

[76] M. Spehr, C. Wetzel, H. Hatt, and B. Ache. 3-phosphoinositides modulate cyclic nucleotide signaling in olfactory receptor neurons. *J. Neurosci.*, 26(1961), 2006.

[77] D. Schild and D. Restrepo. Transduction mechanisms in vertebrate olfactory receptor cells. *Physiol. Rev.*, 78(429), 1998.

[78] C. Dulac. Molecular architecture of pheromone sensing in mammals. *Novartis. Found. Symp.*, 268(100), 2005.

[79] M. Halpern and A. Martinez-Marcos. Structure and function of the vomeronasal system: an update. *Prog. Neurobiol.*, 70(245), 2003.

[80] Y. Zhang, M. A. Hoon, J. Chandrashekar, K. L. Mueller, L. Cook, D. Wu, C. S. Zuker, and N.J. Ryba. Coding of sweet, bitter, and umami tastes: different receptor cells sharing similar signaling pathways. *Cell*, 112(293), 2003.

[81] W. Lin, R. Margolskee, G. Donnert, S. W. Hell, and D. Restrepo. Olfactory neurons expressing transient receptor potential channel m5 (trpm5) are involved in sensing semiochemicals. *Proc. Natl. Acad. Sci. USA*, 104(7):2471–2476, 2007.

[82] O. Matsuzaki, R. E. Bakin, X. Cai, B. P. M. Menco, and Ronnett G. V. Localization of the olfactory cyclic nucleotide-gated channel subunit 1 in normal, embryonic and regenerating olfactory epithelium. *Neuroscience*, 94(131), 1999.

[83] D. Liu and E. R. Liman. Intracellular ca2+ and the phospholipid pip2 regulate the taste transduction ion channel trpm5. *Proc. Natl. Acad. Sci. USA*, 100(15166), 2003.

[84] G. Bazzoni and E. Dejana. Endothelial cell-to-cell junctions: molecular organization and role in vascular homeostasis. *Physiol Rev.*, 84:869–901, 2004.

[85] F. Drees, S. Pokutta, S. Yamada, W.J. Nelson, and W.I. Weis. Alpha-catenin is a molecular switch that binds e-cadherin-beta-catenin and regulates actin-filament assembly. *Cell*, 123:903–15, 2005.

[86] M.J. Levesque, D. Liepsch, S. Moravec, and R.M. Nerem. Correlation of endothelial cell shape and wall shear stress in a stenosed dog aorta. *Arteriosclerosis*, 6:220–9, 1986.

[87] V.S. Sottiurai, S.L. Sue, J.R. Breaux, , and L.M. Smith. Adaptability of endothelial orientation to blood flow dynamics-a morphologic analysis. *Eur J Vasc Surg.*, 3:145–51, 1989.

[88] P. Dieterich, M. Odenthal-Schnittler, C. Mrowietz, M. Kramer, L. Sasse, H. Oberleithner, and H.-J. Schnittler. Quantitative morphodynamics of endothelial cells within confluent cultures in response to fluid shear stress. *Biophysical Journal*, 79:1285–97, 2000.

[89] J. Seebach, G. Donnert, R. Kronstein, S. Werth, B. Wojciak-Stothard, D. Falzarano, C. Mrowietz, S. W. Hell, and H.-J. Schnittler. Flow-induced functional adaptation and differentiation of endothelial cell junction is mediated by rac1. *submitted*, 2007.

[90] J. Seebach, P. Dieterich, F. Luo, H. Schillers, D. Vestweber, H. Oberleithner, H.J. Galla, , and H.J. Schnittler. Endothelial barrier function under laminar fluid shear stress. *Lab Invest*, 80:1819–31, 2000.

[91] B.I. Strauss, B.L. Langille, , and A.I. Gotlieb. In situ localization of f-actin microfilaments in the vasculature of the porcine retina. *Exp Eye Res.*, 45:533–44, 1987.

[92] Y. Lichtenstein, C. Desnos, V. Faundez, R. B. Kelly, and L. Clift-O'Grady. Vesiculation and sorting from pc12-derived endosomes in vitro. *Proceedings of the National Academy of Sciences of the United States of America*, 95(19):11223–11228, 1998. Times Cited: 31 Article English Cited References Count: 30 120ld.

[93] Aidong Yuan, Ralph A. Nixon, and Mala V. Rao. Deleting the phosphorylated tail domain of the neurofilament heavy subunit does not alter neurofilament transport rate in vivo. *Neuroscience Letters*, 393(2-3):264–268, 2006. TY - JOUR.

[94] M. Osborne. Immunofluorescence microscopy of cultured cells. In J. E. Celis, editor, *Cell biology: A Laboratory Handbook*, volume 2, pages 462–468. Academic Press, San Diego, CA, 1998.

[95] W. L. Chao, B. D. Harteneck, J. A. Liddle, E. H. Anderson, and D. T. Attwood. Soft x-ray microscopy at a spatial resolution better than 15nm. *Nature*, 435(7046):1210–1213, 2005. Times Cited: 15 Article English Cited References Count: 31 940jj.

[96] G. Donnert, J. Keller, C. A. Wurm, S. O. Rizzoli, V. Westphal, A. Schönle, R. Jahn, S. Jakobs, C. Eggeling, and S. W. Hell. Two-color far-field fluorescence nanoscopy. *Biophysical Journal*, page online doi:10.1529/biophysj.107.104487, 2007.

[97] X. Michalet and S. Weiss. Using photon statistics to boost microscopy resolution. *Proc Natl Acad Sci U S A*, 103(13):4797–4798, 2006.

[98] S. Ram, E. S. Ward, and R. J. Ober. Beyond rayleigh's criterion: A resolution measure with application to single-molecule microscopy. *Proc Natl Acad Sci U S A*, 103(12):4457–4462, 2006.

[99] M. Fukuda, J.A. Kowalchyk, X. Zhang, T.F. Martin, and K. Mikoshiba. Synaptotagmin ix regulates ca2+-dependent secretion on pc12 cells. *J Biol Chem.*, 227(7):4601–4, 2002.

[100] R.D. Allen, C.C. Schroeder, and A.K. Fok. An investigation of mitochondria inner membranes by rapid-freeze deep-etch techniques. *J. Cell. Biol.*, 108:2233–2240, 1989.

[101] A.S. Reichert and W Neupert. Contact sites between the outer and inner membrane of mitochondria - role in protein transport. *Biochemica et Biophysica Acta - Molecular Cell Research*, 1592:41–49, 2002.

[102] M. Dyba and S.W. Hell. Focal spots of size l/23 open up far-field fluorescence microscopy at 33 nm axial resolution. *Phys. Rev. Lett.*, 88:163901, 2002.

[103] M. Dyba, S. Jakobs, and S.W. Hell. Immunofluorescence stimulated emission depletion microscopy. *Nature Biotechnol.*, 21(11):1303 – 1304, 2003.

[104] T.A. Klar, E. Engel, and S.W. Hell. Breaking abbe's diffraction resolution limit in fluorescence microscopy with stimulated emission depletion beams of various shapes. *Phys. Rev. E*, 64:066613, 1–9, 2001.

[105] T. A. Klar, S. Jakobs, M. Dyba, A. Egner, and S. W. Hell. Fluorescence microscopy with diffraction resolution limit broken by stimulated emission. *Proc. Natl. Acad. Sci. USA*, 97:8206–8210, 2000.

[106] K. I. Willig, R. R. Kellner, R. Medda, B. Hein, S. Jakobs, and S. W. Hell. Nanoscale resolution in gfp-based microscopy. *Nature Methods*, 3(9):721–723, 2006.

[107] S. W. Hell and M. Kroug. Ground-state depletion fluorescence microscopy, a concept for breaking the diffraction resolution limit. *Appl. Phys. B*, 60:495–497, 1995.

[108] A.N. Tikhonov and V.Y. Arsenin. *Solutions of Ill-posed problems*. Wiley, New York, 1977.

[109] T.J. Holmes and Y.-H. Liu. Richardson-lucy/maximum likelihood image restoration algorithm for fluorescence microscopy: further testing. *Appl. Optics*, 28:4930–4938, 1989.

[110] T. Lang, D. Bruns, D. Wenzel, D. Riedel, P. Holroyd, C. Thiele, and R. Jahn. Snares are concentrated in cholesterol-dependent clusters that define docking and fusion sites for exocytosis. *EMBO J.*, 20(9):2202–2213, 2001.

[111] C.J. Barnstable, R. Hofstein, and K. Akagawa. A marker of early amacrine cell development in rat retina. *Brain Research*, 352:286–90, 1985.

[112] F.J. Navone, G. Di Gioia, H. Stukenbrok, P. Greenhard, and P. De Camilli. Protein p38: An integral membrane protein for small vesicles of neurons and neuroendocrine cells. *J Cell Biol.*, 103:2511–27, 1986.

[113] S. O. Rizzoli, I. Bethani, D. Zwilling, D. Wenzel, T.J. Siddiqui, D. Brandhorst, and R. Jahn. Evidence for early endosome-like fusion of recently endocytosed synaptic vesicles. *Traffic*, 7(9):1163–76, 2006.

[114] W. Lin, J. Arellano, B. Slotnick, and D. Restrepo. Odors detected by mice deficient in cyclic nucleotide-gated channel subunit a2 stimulate the main olfactory system. *J. Neurosci*, 24:3703–10, 2004.

[115] C. Perez, R. Margolskee, S.C. Kinnamon, and T. Ogura. Making sense with trp channels: store-operated calcium entry and the ion channel trpm5 in taste receptor cells. *Cell Calcium*, 33:541–49, 2003.

[116] H.-J. Schnittler, R.P. Franke, U. Akbay, C. Mrowietz, and D. Drenckhahn. Improved in vitro rheological system for studying the effect of fluid shear stress on cultured cells. *Am J Physiol.*, 265:C289–98, 1993.

[117] H.-J. Schnittler, B. Puschel, , and D. Drenckhahn. Role of cadherins and plakoglobin in interendothelial adhesion under resting conditions and shear stress. *Am J Physiol.*, 273:H2396–405, 1997.

A Appendix

A.1 Setup D-Rex measurements

The experiments were performed with a stage-scanning fluorescence microscope featuring an oil immersion objective (100x magnification, 1.4 numerical aperture, i.e., $\alpha = 68°$; Leica, Mannheim, Germany) producing nearly diffraction-limited spots. For one-photon excitation we used a linearly polarized pulsed laser diode (470nm, $\tau_P = 100$ ps, LDH-P-C-470, PicoQuant GmbH, Berlin, Germany). Variation of the pulse rate was realized by means of a frequency generator. A linearly polarized argon laser (Omnichrome Series 43, Melles Griot, Carlsbad, CA) was applied for CW excitation at 488 nm. For two-photon excitation at 800 nm a femtosecond modelocked, linearly polarized Ti:Sa Laser of 80 MHz repetition rate (MaiTai, Spectra-Physics Lasers GmbH, Darmstadt, Germany) was utilized. A Single Pulse Selector (Pulse Select, APE GmbH, Berlin, Germany) equipped with a TeO$_2$ Bragg cell was used to adjust f from 40 down to 0.3 MHz. Where required, the initial pulse width $\tau_P = 200$ fs was stretched to ≈ 1 ps by a 20 cm SF6 glass rod. Longer durations were realized by passing the pulses through 2-20 m long glass fibers (PMF-RC-820-BL single-mode polarization maintaining, cutoff at 820 nm, StockerYale Inc., Halem, U.K.). τ_P was measured with an autocorrelator (Pulse Check, APE GmbH) or a microchannel plate photomultiplier tube (R3809U, Hamamatsu, Japan). The fluorescence emission was collected by the same objective lens and projected onto an avalanche photodetector (SPCM-AQR-13-FC, Perkin Elmer Optoelectronics, Fremont, CA) with an aperture size corresponding to 0.8 times the magnified Airy disk of the fluorescence spot. The detection events were further processed by a PC card (SPC 730, Becker&Hickl GmbH, Berlin, Germany), enabling the observation of the fluorescence count rate within varying observation time windows. The intensity point-spread function (PSF) of the excitation laser was probed by a gold bead of 80 nm diameter on a nonconfocal detector (MP 963 Photon Counting Module, Perkin Elmer). The full width at half maximum (FWHM) of the PSF in the focal plane and the power I$_P$ measured at the sample entered the calculation of the applied pulse peak intensities I$_P$ = P/$[\pi(0.5$ FWHM$)^2$ $(\tau_P$ f$)]$.

A.2 Deconvolution

A single-step linear deconvolution (LD) ([108]), i.e. Wiener filter, was carried out where indicated with a theoretical PSF FWHM as indicated (if no further specifications are made the images of Atto532 have been deconvolved with 20 nm and images of Atto647N with 60 nm, respectively). Alternatively a nonlinear deconvolution technique (RL) was applied were indicated, taking the positivity condition of the dye concentrations into account ([109]).

A.3 Alignment of the Dual-colour images

The two colour images showed a shift of their respective focusing points in the order of 50-100 nm. Therefore, two independent alignment procedures were applied.

In a first approach, an additional sample of dual-labeled fluorescence beads was prepared (green and red fluorophore, bead diameter 24 ± 4 nm, Molecular Probes, Leiden, Germany) by spreading them out on a silanized microscope cover glass, concentrating green and red fluorescence emission on the same spot. By calculating the crosscorrelation of the two (green and red) confocal images of these beads the lateral shift between the focal positions from the maximum of the crosscorrelation function can be rendered. This lateral shift was used to overlay the subsequently recorded two-colour confocal and STED images of the sample of interest. In a final alignment step the relative shift of the positions of the center of the confocal excitation PSF compared to the zero-intensity position of the STED light distribution was compensated. These zero-intensity positions define the centers of the effective PSFs in STED microscopy and can slightly vary between the different colours. I maintained this shift from the direct PSF measurements.

The alternative way was to incorporate double-labeled beads in the sample preparation process. They could be distinguished from the sample structure by featuring a small point like shape in both STED channels simultaneously. The shift between images of several beads in the two channels was then again computed by cross correlation techniques. The errors of these alignment procedures were estimated by modeling typical situations and testing the alignment procedures in these situations. Therefore, a model with an adapted number of objects, an adapted number of photons including a background and a typical shift of about 50 nm was chosen. The error obtained by repeated alignments of the noisy model images amounts to ± 17 nm in the first procedure and to about ± 5 nm in the second procedure.

A.4 Algorithm for deploying photon statistical localization methods

An algorithm was created[1] that identified separable bead positions in the image by evaluating the brightest position in a smoothed image first, fitting a 2D bead model including diameter, brightness and position convolved with an assumed PSF locally to the image, clearing the image of the obtained object and restarting the algorithm until a threshold was reached ([97],[98]). Only objects with a sufficiently high goodness of the fit were taken into account since they present separable and bright bead images. To account for the remaining parts of the image, a constrained deconvolution algorithm (RL) was applied that kept the results of the bead identification unchanged.

A schematic of the working principle of the algorithm is exemplified on a dense sample of yellow green beads (24nm FWHM) in Fig.A.1.
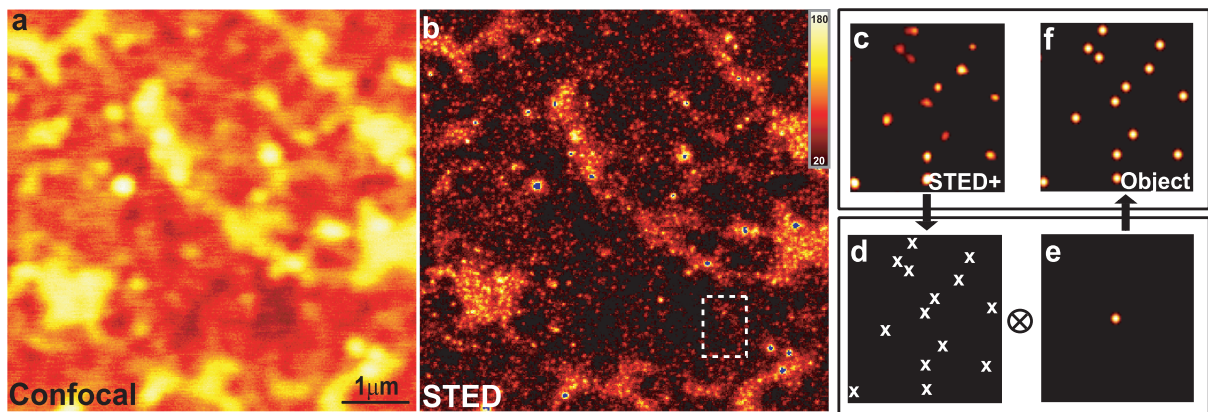
Figure A.1: Confocal (a) and STED (b) images of yellow-green beads. (c) Magnified outtake of the STED image after applying an RL-deconvolution. The deconvolved image reveals the individual bead positions (d) which are identified by the algorithm. After convolution with the object (e) of a 24 nm bead-projection the image is restored at every identified bead position. If all beads are identified the image is fully restored (f). Note that this process needs a-priori information of the subunits (in this case 24 nm bead objects) the object is actually consisting of to successfully apply the algorithm.

---

[1]Jan Keller, Department of Nanobiophotonics

A.5 Immunolabeling protocols

Labeling of SC35 protein in the nucleus

HeLa SS6 cells were grown on glass coverslips (FisherScientific) in Dulbecco's modified Eagle's medium (GibcoBRL) supplemented with 10% fetal calf serum (GibcoBRL) and 100 U ml-1 penicillin/streptomycin (Biochrom KG) at 37°C, 5% CO2. Cells were washed with PBS, fixed for 20 min with PBS pH 7.4/4% (wt/vol) paraformaldehyde, rinsed with PBS pH 7.4 and permeabilized in PBS pH 7.4/0.2% Triton X-100 (Sigma) for 20 min. Cells were then rinsed with PBS, blocked in PBS pH 7.4/10% Fetal Calf Serum (FCS) for 30 min and incubated for 60 min with the mouse anti-SC35 antibody (BD Pharmingen, San Diego, CA) diluted 1:500 in PBS pH 7.4/10% FCS. Subsequently, cells were washed and incubated overnight with the secondary Atto532 labeled antibody at 4°C. The coverslips were again washed and mounted in Mowiol (Merck, Darmstadt).

Syntaxin mambrane patches

PC12 cells (clone25) were maintained, propagated and transfected essentially as described ([110]). Membrane sheets were immunostained for systaxin 1 as previously described ([75]). As primary antibody we applied HPC-1 ([111]), as secondary antibodies goat anti-mouse-Atto532.

Endosomes preparation from PC12 cells

Enriched early endosomes were diluted to approximately 4 μg/ml protein, and centrifuged onto bovine serum albumin-coated coverslips for 40 minutes at 5900g. They were paraformaldehyde-fixed, and immunostained using anti-synaptotagmin I monoclonal antibodies (Clone 41.1, Synaptic Systems, Göttingen, Germany), and anti-synaptophysin polyclonal serum ([112]). The antibodies were applied at a dilution of 1:100, in PBS containing 1.5% BSA. After washing, sheep anti-mouse and anti-rabbit antibodies, conjugated to Atto 532 or Atto 647 (Atto Tec, Siegen, Germany), were applied for 2 hours, followed by washing with PBS (500 mM NaCl) and embedding in Mowiol or Moviol containing double-labeled alignment beads.
Preparation of early endosomes from PC12 cells. Early endosomes were enriched from post nuclear supernatants by use of discontinuous sucrose gradients, as previously described ([113]).

Neurofilaments in the human brain

The SH-SY5Y neuroblastoma cell line was grown as described previously ([93]). Cells were seeded on standard glass coverslips to a confluency of about 80%. 10μM all-trans-Retinoic Acid (RA) (EMD Biosciences Inc., San Diego, United States) was added the day after plating. After 5 days in the presence of RA cells were washed 3 times and incubated with 50 ng/ml human Brain Derived Neurotrophic Factor (hBDNF) (Alomone Laboratories, Jerusalem, Israel) in serum-free medium. Immunostaining of neurofilaments as a neuronal marker protein was performed with anti-200kD Neurofilament heavy subunit rabbit IgG (Abcam, Cambridge, UK) as primary antibody and with anti-rabbit conjugated Atto 532 IgG as secondary antibody respectively. The cells were mounted in Mowiol.

Mitochondrial proteins

For immunolabeling cultured PtK2 cells from the marsupial Potorous tridactylus were grown on coverslips, fixed with 4% formaldehyde for 15 minutes at room temperature and incubated with primary antibodies specific for the mitochondrial ATP synthase (mouse anti ATP synthase, alpha subunit, Molecular Probes, Leiden, Netherlands) or specific for the translocase of the mitochondrial outer membrane (rabbit anti Tom20, Santa Cruz, CA, USA). These primary antibodies were detected with secondary antibodies (goat anti rabbit, sheep anti mouse; Jackson ImmunoResearch Laboratories, PA, USA) coupled to Atto532 (Atto Tec, Siegen, Germany) or Atto647N (Atto Tec, Siegen, Germany). The stained cells were mounted in Mowiol and where indicated in Mowiol containing double-labeled alignment beads (Molecular Probes, Leiden, Netherlands) for imaging respectively.

Tissue preparation for TRPM5 immunolabeling

For euthanasia mice were anesthetized with ketamine/xylazine (100 μg - 20 μg/g body weight), perfused transcardially with 0.1M phosphate buffer (PB) followed by a PB buffered fixative containing 3% paraformaldehyde, 0.019 M L-lysine monohydrochloride, and 0.23% sodium m-periodate ([114]). The olfactory bulbs and nose were harvested and post-fixed for 2 h before being transferred for cryoprotection into PBS with 25% sucrose overnight. Olfactory bulbs were cut into 4 μm thick transverse sections mounted on Superfrost Plus slides (VWR) for the T-Rex STED experiments to minimize light scattering and background fluorescence. Sagittal cuts maximized the number of glomeruli visualized in medial and lateral sections.

For immunolabeling, sections were rinsed and incubated in blocking solution containing 2% normal donkey serum, 0.3% Triton X-100 and 1% bovine serum albumin in PBS for 1.5

hour. Sections were then incubated with primary antibodies for periods from overnight to 72 hours. Antibodies against rabbit anti TRPM5 (1:250 to or 1:500) ([115]) were used. Finally we utilized ATTO 532 anti rabbit as the secondary antibody (Atto-Tech GmbH, Germany). Removal of primary antibody resulted in no labeling in control sections.

Immunolabeling of VE-cadherin

Endothelial cells derived from human umbilical cord veins were harvested and cultured as described elsewhere ([116]). Endothelial cells from the first passage were used for the experiments. Cells were seeded on cross-linked gelatine coated glass cover slips, or glass slides especially manufactured for rheological experiments. Cells cultured on glass supports were fixed with 2% formaldehyde in phosphate buffered saline (PBS: 137 mmol/l NaCl, 2.7 mmol/l KCl, 1 mmol/l Na2HPO4, 1.5 mmol/l KH2PO4, pH 7.4) and permeabilized with 0.1% Triton X-100 for 10 minutes. Antibody labeling was performed as described elsewhere ([117]).

Acknowledgement

List of Publications

Parts of this thesis have been or will be published

1. Donnert, G., J. Keller, R. Medda, M. A. Andrei, S. O. Rizzoli, R. Lührmann, R. Jahn, C. Eggeling, S. W. Hell. 2006. *Macromolecular-scale resolution in biological fluorescence microscopy.* Proc. Natl. Acad. Sci. USA 103 (31): 11440-11445, 2006

2. Donnert, G., Eggeling, C., Hell, S. W. *Major signal increase in fluorescence microscopy through dark state relaxation.* Nature Methods, 4:81-86, 2006

3. Donnert, G., Keller, J., Westphal V., Wurm C., Jakobs, S., Rizzoli, S. O., Lührmann, R., Eggeling C., and S. W. Hell. *Two-Color Fluorescence Microscopy on the Nanoscale.* Biophysical Journal, online as doi:1529/biophysj.107.104497, 2007

4. Lin, W., Margolskee, R., Donnert, G., Hell., S.W., and Restrepo, D. *Olfactory neurons expressing transient receptor potential channel M5 (TRPM5) are involved in sensing semiochemicals.* Proc. Natl. Acad. Sci. USA 104 (7): 2471-2476, 2007

5. Sieber, J., Willig K. I., Kutzner, C., Gerding-Reimers, C., Harke, B., Donnert, G., Rammner B., Eggeling, C., Hell, S. W., Grubmüller, H., and T. Lang. *Anatomy and dynamics of a supramolecular membrane protein cluster.* submitted to science, 2007

6. Seebach, J., Donnert, G., Werth, S., Wojciak-Stothard, B., Falzarano, D., Feldmann, H., Mrowietz, C., Hell, S. W., and Schnittler, H.-J., *Flow-induced functional adaptation and differentiation of endothelial cell junctions is mediated by rac-1.* submitted

7. Hell, S. W., Donnert, G., Rankin, B., Willig, K.I., *Nanoscale resolution in far-field fluorescence microscopy with STED* Handbook of Lasers and Optics (Springer), in press

8. S.W. Hell, C. Eggeling and G. Donnert,*Verfahren und Vorrichtung zum optischen Messsen einer Probe*, 14.06.2005, European Patent